

On variational modelling of wave slamming by water waves

Tomasz Jakub Salwa



Submitted in accordance with the requirements for the degree of Doctor of Philosophy

The University of Leeds
Department of Applied Mathematics

September 2018

Declaration

The candidate confirms that the work submitted is his/her/their own, except where work which has formed part of jointly authored publications has been included. The contribution of the candidate and the other authors to this work has been explicitly indicated below. The candidate confirms that appropriate credit has been given within the thesis where reference has been made to the work of others.

Chapters 2, 3 and 4 include work published in

T. Salwa, O. Bokhove, and M. A. Kelmanson. Variational modelling of wave–structure interactions with an offshore wind-turbine mast. *Journal of Engineering Mathematics*, 107(1):61–85, Dec 2017. ISSN 1573-2703. doi: 10.1007/s10665-017-9936-4. URL <https://doi.org/10.1007/s10665-017-9936-4>

and its preceding conference papers Salwa et al. (2016a,b).

Attributable to T. Salwa: code implementation, most of the analytical computations, derivations and writing.

Attributable to O. Bokhove and M. Kelmanson: nonlinear model formulation, chi-coordinate transformation, proof-reading, guidance in derivations.

This copy has been supplied on the understanding that it is copyright material and that no quotation from the thesis may be published without proper acknowledgement. The right of Tomasz Jakub Salwa to be identified as Author of this work has been asserted by him in accordance with the Copyright, Designs and Patents Act 1988.

©2018 The University of Leeds and Tomasz Jakub Salwa

Abstract

This thesis is concerned with the development of both mathematical (variational formulation) models and simulation (finite-element Galerkin) tools for describing a physical system consisting of water waves interacting with an offshore wind-turbine mast.

In the first approach, the starting point is an action functional describing a dual system comprising a potential-flow fluid, a solid structure modelled with nonlinear elasticity, and the coupling between them. Novel numerical results for the linear case indicate that our variational approach yields a stable numerical discretization of a fully coupled model of water waves and an elastic beam.

The drawback of the incompressible potential flow model is that it inevitably does not allow for wave-breaking. Therefore another approach loosely based on a van-der-Waals gas is proposed. The starting point is again an action functional, but with an extra term representing internal energy. The flow can be assumed to have no rotation, so although it is again described with a potential, compressibility is now introduced. The free surface is embedded within the compressible fluid for an appropriate van-der-Waals-inspired equation of state, which enables a pseudo-phase transition between the water and air phases separated by a sharp or steep transition variation in density. Due to the compressibility, in addition to gravity waves the model enables acoustic ones, which is confirmed by a dispersion relation. Higher-frequency acoustic waves can be dampened by the appropriate choice of time integrators. Hydrostatic and linearized models have been examined as verification steps. The model also matches incompressible linear potential flow. However, at the nonlinear level, the acoustic noise remains significant.

Acknowledgements

This work was supported by the European Commission, Marie Curie Actions - Initial Training Networks (ITN), project number 607596. I would like to greatly thank my supervisor Prof. Onno Bokhove for research guidance, sharing his vast knowledge and devoted time. I am equally grateful to my co-supervisor Prof. Mark Kelmanson for his guidance, support and effort in making my thesis accessible to the reader. A particular gratitude is reserved for Dr Floriane Gidel for friendly company during the long PhD process and scientific help. Many thanks go to Leeds Water Waves group for fruitful discussions. These especially include Dr Anna Kalogirou and William Booker for their assistance. I would like to thank Firedrake developers, in particular Dr David Ham and Dr Lawrence Mitchell, for their technical support. I am also grateful to Ir. Geert Kapsenberg and Dr. Ir. Tim Bunnik from the Maritime Research Institute Netherlands (MARIN) for contributing their scientific expertise.

Contents

Abstract	ii
Acknowledgements	iii
Contents	iv
List of figures	vii
List of tables	xiii
Nomenclature	xiv
1 Introduction	1
1.1 Motivation	1
1.2 Objectives	3
1.3 Outline of the thesis	6
2 Elastic beam: mathematical formulation and FEM	7
2.1 Nonlinear hyperelastic mast	7
2.2 Linearized elastic dynamics	10
2.3 Numerical model	13
2.3.1 Time discretization schemes	15

CONTENTS

2.3.2	Discretization and implementation	19
2.4	Results	19
2.4.1	Conclusions	21
3	Nonlinear variational modelling of wave-structure interactions	23
3.1	Potential-flow water waves	23
3.2	Coupled model	25
3.2.1	Conclusions	28
4	Linear variational modelling of wave-structure interactions: finite-element method	29
4.1	Introduction	29
4.2	Linearization of the variational principle	30
4.3	Solution of the coupled linear system	36
4.3.1	FEM space discretization	37
4.3.2	Time discretization	43
4.4	Results	46
4.4.1	2D results	46
4.4.2	3D results	47
4.5	Discussion	54
5	Towards modelling and simulating breaking waves	55
5.1	Introduction	55
5.2	Compressible van-der-Waals-like fluid	56

CONTENTS

5.2.1	Model formulation	56
5.2.2	Equations of state	58
5.3	Linear waves	65
5.3.1	One-phase model	67
5.3.2	C^0 EOS and discontinuous speed of sound	68
5.3.3	C^0 EOS and speed of sound	70
5.3.4	Fluid in a box	73
5.4	Nonlinear results	75
5.4.1	C^0 EOS and discontinuous speed of sound	77
5.5	Conclusions	78
6	Code tutorial	81
6.1	Linear mixed fluid-structure interaction system	81
7	Conclusions	94
7.1	Summary	94
7.1.1	Achievements and concomitant extensions	94
7.1.2	Outreach	96
7.1.3	Experiment	97
	Appendices	98
A	Derivation of temporal discretization	98
	Bibliography	101

List of figures

1.1	A monopile offshore wind turbine from a wind farm at Horns Reef in the North Sea. Source: http://en.stonkcash.com/wind-energy-sustaility/ . . .	2
1.2	A sketch of the process of mathematical modelling, verification, validation and application.	4
2.1	A sketch of the beam geometry, depicting a cross-section in the $x-z$ plane, in which $\mathbf{a} = \mathbf{X}(\mathbf{a}, 0)$ is the Lagrangian coordinate in the reference state (boundary denoted by closed solid line); $\mathbf{X}(\mathbf{a}, t)$ is the position of a point in the deformed beam (boundary denoted by closed dashed line) and $\tilde{\mathbf{X}}(\mathbf{a}, t)$ its deflection; $\partial\Omega_0$ denotes the structure boundary and $\partial\Omega_0^b$ its fixed bottom.	8
2.2	Initial state of the (non)linear beam test case.	20
2.3	The energy partition of the evolving system as function of time for both the linear and nonlinear model. In the legend, E_p denotes potential energy, E_k kinetic energy and E_t the total energy.	20
2.4	The difference between the linear and nonlinear potential energy scaled by the total energy as a growing function of time.	21

LIST OF FIGURES

3.1 Geometry of the fluid domain: a box with rest-state dimensions $L_x \times L_y \times H_0$ and evolving free surface $z = H_0 + \eta(x, y, t) = h(x, y, t)$. Here $\eta(x, y, t)$ is the free-surface perturbation from the rest state that first appears in (4.2). 24

3.2 Geometry of the linearized or rest system: fluid (hatched) and elastic beam (cross-hatched). This 2D representation is in the $y = 0$ plane, with the y -axis directed into the page, in which direction the full 3D configuration has uniform depth L_y 26

3.3 Definition of the variables used in the VP transformation. Here $x_s(y, z, t)$ denotes the position of the fluid-structure interface and $\chi = L_s x / x_s(y, z, t)$ denotes the transformation of the domain to one whose dimension is fixed in the x -direction. A cross-section perpendicular to the y -direction is shown. 27

4.1 Flow chart schematically depicting the solution method. The subscript $(\cdot)_h$ denotes a spatially discretized function and superscript $(\cdot)^n$ the timestep counter. 36

4.2 Energy apportionment (in J) in the 2D system. From top to bottom (see key), curves represent energies of the total system (medium, horizontal), total water (thick, wavy), potential/kinetic water (thick dotted/dashed oscillatory), total beam (thin, wavy) and potential/kinetic beam (thin dotted/dashed oscillatory). 48

4.3 Convergence of the temporal energy as a function of timestep in 2D: relative error curves for timesteps Δt (upper curve) and $\Delta t/2$ (lower curve) have amplitudes in the ratio four to one, confirming second-order convergence. 48

LIST OF FIGURES

4.4 Rate of convergence, s in (4.46), of ϕ against time, computed using 3 regularly refined meshes and two norms: L_2 (solid line) and L_∞ (dashed line). As the mesh size tends to zero, the theoretical limit of Aitken acceleration yields $s = 2$ 49

4.5 Temporal snapshots of the 2D water-beam geometry during flow evolution. Although the computational domain is fixed, results have been post-processed into physical space to visualize the deformations. Initial condition of no flow (top) with motion initiated by free-surface displacement. Solutions after 3s (middle) and 5s (bottom). 50

4.6 Energy apportionment (in J) in the 3D system: water (top) and beam (bottom). Curves represent total (continuous), potential (dotted) and kinetic (dashed) energies. Note from the disparate vertical scales in the two plots that the total beam energy is much less than that of the water. . . 51

4.7 Convergence of the method as a function of the timestep in 3D: the full timestep (upper curve, grey) and half timestep (lower curve, black) relative-error curves have amplitudes in the ratio four to one, confirming second-order convergence. 52

4.8 Temporal snapshots of the 3D water-beam geometry during flow evolution. Although the computational domain is fixed, results have been post-processed into physical space to visualize the deformations. (Top left) initial condition; no flow; motion initiated by free-surface displacement. Physical flow geometries after 1.1 s (bottom left), 3.8 s (top right) and 5.9 s (bottom right). Colours, white to black, indicate flow-potential values. A beam deflection is clearly evident. 53

LIST OF FIGURES

5.1	Two-phase (top), three-phase (middle) and C^∞ (bottom) interface models. Density (left) and pressure (right) in the limit $\rho_a \rightarrow 0$, $c_a \rightarrow \infty$, $c_w \rightarrow \infty$, $c_a^2 \rho_a = p_a = 1000$ hPa, $\rho_w = 1000$ kg/m ³ with colors: blue, green, red to brown as the values approach the incompressible limit (black). The interface is located at $H_0 = 40$ m, while the total tank height $H = 80$ m.	60
5.2	The hyperbola, described by setting $a = b = 1$ in equation (5.20) centred at the origin, with lower branch (‘-’-blue), upper branch (‘+’-yellow), asymptotes $y = 0$ and $y = x$ (green), crossing y - axis at $b = \pm 1$	63
5.3	Equations of state: pressure as a function of density for the C^∞ model (blue) compared with the two-phase model (5.10) (yellow) and three-phase model (5.16) (green). Parameter values are: $c_a = 25$ m/s, $c_w = 30$ m/s, $c_m = 7$ m/s, $p_a = 1000$ hPa, $\rho_a = 160$ kg/m ³ , $\rho_w = 1000$ kg/m ³ , $b_a = 0.1p_a$, $b_w = 0.2p_a$	64
5.4	Driving term $Q(\rho) - Q(\rho_0(z))$ as a function of ρ and z . Parameter values are as given in the caption of Fig. 5.3 with the addition of $H_0 = 40$ m. . .	65
5.5	Dispersion curves computed from (5.41) for the pseudo two-phase model. Parameter values are: $c_w = 120$ m/s, $c_a = 100$ m/s, $c_m = 2$ m/s, $H_0 = 40$ m, $H = 80$ m, $\rho_w = 1000$ kg/m ³ , $p_a = 10^5$ Pa. The black curve represents the gravity-wave dispersion relation, and its presence reveals the absence of gravity-wave modes in the solution of the dispersion relation (5.41).	69
5.6	Dispersion curves for three-phase model, for which results up to $k = 2$ m ⁻¹ now agree with the gravity-wave dispersion relation shown by the black line. Parameter values are (top) $c_a = 100$ m/s, $c_w = 120$ m/s, $c_a = 2$ m/s and (bottom) $c_a = 316$ m/s, $c_w = 1500$ m/s, $c_a = 1$ m/s.	72

LIST OF FIGURES

5.7 The profile of $\hat{\phi}$ (red line) from the three-phase gas model compared, for $z \geq 0$, with ϕ from linear potential-flow water-wave theory (dashed blue line). Parameter values are $c_a = 100$ m/s, $c_w = 120$ m/s, $c_a = 2$ m/s. 73

5.8 Linear ρ at $x = 0$ and $\omega t = 0, \frac{\pi}{2}, \frac{3\pi}{2}$ corresponding to initial (hydrostatic, black), maximal (red) and minimal (min) displacement values. The reconstructed position of the free surface is obtained as the intersection of extrapolated solutions from different regions (dashed lines). The free-surface deviation η from the equilibrium given by linear potential-flow water waves with amplitude 0.2m is added for comparison (blue and red dots). Parameter values are as in the caption of Figure 5.7. 74

5.9 Free-surface level obtained by finding the intersection point between extrapolated solutions of the water and middle regions, compared with linear potential-flow water waves at their maximal deviation of amplitude of 0.01m. Parameter values are as in the caption of Figure 5.7. 75

5.10 Density-profile evolution in the 2D two-phase model (left) compared with the profile in the incompressible, linear potential-flow water-wave model mapped onto the same mesh (right) at times 0 (top) 2 (middle) and 5 seconds (bottom). The top figures also display the mesh, for which the uniform horizontal spacing is $\Delta x = 4$ m and the minimum vertical spacing is $\Delta z = 0.7$ m. The initial state for the gas model is constructed as the hydrostatic state with a shifted level of the free surface at each point, the shift corresponding to the level from the incompressible case. The growth of acoustic modes with time is clearly evident. Parameter values used (see main text for description) are: $a = 8$ m, $\lambda = 160$ m, $c_w = 120$ m/s, $c_a = 100$ m/s, $c_m = 2$ m/s, $H_0 = 40$ m, $H = 80$ m, $L = 80$ m, $\rho_w = 1000$ kg/m³, $p_a = 10^5$ Pa. 80

LIST OF FIGURES

6.1	Geometry and initial condition in the system. Fluid with deflected free surface (blue) and the structure (red).	84
7.1	The wave tank set-up with a wave-maker (left), beach (right) and a beam.	97

List of tables

4.1	Parameter values used in the 2D computations.	47
4.2	Parameter values used in the 3D computations.	49
5.1	Simulation time until divergence t_{div} for a given timestep size for the symplectic Euler scheme, on a reference mesh (left) and one that has been refined by splitting (right).	78

Nomenclature

x, y, z, t Cartesian coordinates and time

$\Omega, \partial\Omega$ current fluid domain and boundary

$\Omega_0, \partial\Omega_0$ reference structure domain and boundary

$\partial\Omega_f$ free surface

$\partial\Omega_s$ fluid-structure interface

$\partial\Omega_w$ rigid fluid walls

$\partial\Omega_0^b$ structure-base boundary

L_x fluid domain length

H_0 rest state water level

H mixed fluid domain height

L_y fluid and structure width

L_z beam height

L_s x -position of the fluid-structure interface

\mathbf{n} unit outward normal vector for fluid domain

\mathbf{n}_0 unit outward normal vector for structure domain

$\mathbf{a} = (a, b, c)^T = (a_1, a_2, a_3)^T$ Lagrangian coordinates

- i, j, a, b, c spatial indices $\in \{1, 2, 3\}$
- T_{ij} stress tensor
- E_{ij} Green-Lagrangian strain tensor
- e_{ij} linear strain tensor
- $\partial_i = \partial/\partial x_i$ partial derivative with respect to i^{th} component
- $\mathbf{X} = (X, Y, Z)^T = (X_1, X_2, X_3)^T$ structural position
- $\tilde{\mathbf{X}}$ structural displacement
- $\mathbf{U} = (U_1, U_2, U_3)^T$ structural velocity
- W elastic energy
- \mathbf{E} Lagrangian-Green strain tensor
- \mathbf{F} deformation gradient
- λ, μ first and second Lamé constants
- \mathcal{L}, \mathcal{H} continuous Lagrangian and Hamiltonian functionals
- ρ fluid density
- ρ_0 structural material density
- $\rho_0(z)$ hydrostatic fluid density
- ρ_a air reference density
- ρ_w water reference density
- c_a speed of sound in air
- c_w speed of sound in water
- c_m speed of sound in interface region
- ϕ flow potential

η free-surface displacement

g gravitational acceleration

p pressure

p_a constant air pressure

$U(\rho)$ fluid internal energy

Indices for nodes in finite-element discretization

i, j all nodes in fluid domain; also spatial indices $\in \{1, 2, 3\}$, depending on context

α, β free-surface nodes

i', j' nodes in fluid domain excluding surface nodes

k, l structure nodes

k', l' structure nodes excluding fixed-base ones

m, n interface nodes (fluid)

\tilde{m}, \tilde{n} interface nodes (structure)

\tilde{m}', \tilde{n}' interface nodes (structure) excluding fixed-base ones

$\tilde{\varphi}_i, \tilde{\varphi}_\alpha, \tilde{X}_k$ finite-element basis functions

V, T, M, D scales for: velocity, time, mass and length

$M_{\alpha\beta}, A_{ij}, W_{\tilde{m}n}, N_{kl}, B_{kl}^{ab}, E_{kl}^{ab}$ finite-element matrices of integrals of basis functions

L, H discrete Lagrangian and Hamiltonian functions

P_k^a conjugate variable to X_k^a

C, D, U, F auxiliary finite-element matrices used in the derivation

L, H abstract generalized Lagrangian and Hamiltonian functionals

Q, P abstract generalized coordinate and its conjugate

Chapter 1

Introduction

1.1 Motivation

One of the characteristic traits of contemporary civilization is rapid economic growth, the concomitant advantages of which, such as general higher standards of living and decreased poverty, have their consequences. Among the most important of these is increasing energy consumption, as a result of which — and contemporaneously with the promotion of energy-saving products, policies and lifestyles — mankind has been searching for alternative and effective sustainable energy sources that support balanced growth. One of the energy sources that has been actively explored in recent years is offshore wind energy. On the one hand, going offshore with wind energy is stimulated by ameliorating negative visual impacts to high-value scenic resources (Sullivan et al., 2012, 2013) and by reducing noise/discomfort for local inhabitants from onshore wind turbines. On the other hand, the overall greater wind supply in offshore areas translates to better energy-producing efficacy.

There are two main branches of active research in the field of wind energy, namely offshore floating platforms with wind turbines and fixed-bottom monopile wind farms in shallow water: a review is given in Benitz et al. (2015). The first branch is still in the prototype stage of development and will not be addressed in this work. The



Figure 1.1: A monopile offshore wind turbine from a wind farm at Horns Reef in the North Sea. Source: <http://en.stonkcash.com/wind-energy-sustainability/>

second branch, *i.e.* concerning shallow and intermediate-depth-water, fixed-bottom wind turbines, already exists *e.g.* in areas of the North Sea, see Fig. 1.1. It is accordingly considered in this thesis.

The aerodynamics of onshore and offshore wind turbines are essentially the same. The interesting difference occurs at the bottom of the latter case, namely the structure's interaction with water waves. It is extremely important to take this factor into account when designing a new wind turbine, as otherwise the wave loads can damage or destroy the whole structure. In mitigating this risk, mathematical modelling proves particularly useful.

A mathematical model describes the system of interest using mathematical concepts and language. For our purposes it will be the language of partial differential equations for continuum mechanics. For real applications, such a model involves certain assumptions and simplifications about the system it aspires to describe. On the one hand, it is never

known *a priori* whether those assumptions and simplifications were sufficiently justified and do not adversely affect final predictions of the model. On the other hand, too many variables and extensive complexity of the model tend to blur our understanding of the important underlying processes, let alone our ability to monitor and control them. Moreover, one may not be able to obtain solutions at all or within a reasonable time. The ultimate criterion of the correctness of the model is whether there is a reasonable-to-good agreement between its predictions and experimental data. If the model fails to do so, then it has to be reformulated or improved. Once a model has been verified and validated for a particular set of conditions, then it can be used with reasonable confidence to give correct predictions under different conditions within its scope of application. This fact is widely used in engineering applications and so it is utilised in our case. A mathematical model of interaction between water waves and an offshore wind-turbine mast can be used in a design process to determine what loads a real structure will be exposed to and to predict its response. Before the proposed model is deployable, its predictions have to be verified against experimental data drawn from a small-scale test model. There are scientific testing facilities, *e.g.*, at the Maritime Research Institute Netherlands (MARIN), that specialize in conducting such experiments by using dedicated water basins with appropriate wavemakers. If a bespoke model does not match relevant experimental data, then it has to be changed until its predictions are satisfactory. This iterative interaction of validation and improvement is germane to the spirit of respectable mathematical modelling; it is sketched in Fig. 1.2.

The aim of the project presented in this thesis was to develop such a mathematical model of wave impact on a single beam/mast of an offshore wind turbine.

1.2 Objectives

Fixed-bottom offshore wind-turbine models have already been widely studied and can be found in the literature. A 1-way coupling method was implemented by Bunnik

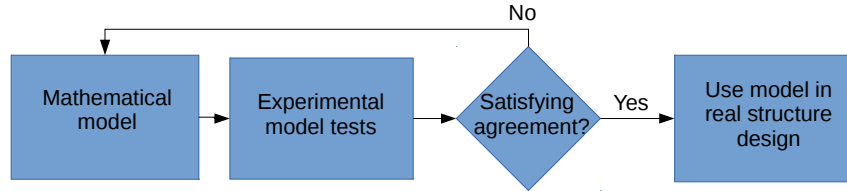


Figure 1.2: A sketch of the process of mathematical modelling, verification, validation and application.

et al. (2015) and tested at MARIN. Sagar et al. (2015) used a volume-of-fluid (VOF) method and solved the Reynolds-Averaged Navier-Stokes Equations (RANSE). Other fluid-structure interaction (FSI) problems with 3D finite element (FE) beam models have also been developed and applied to marine structures by many authors. Therefore, in this work we will not simply focus on developing another FSI solver, but rather the problem will be addressed from a novel mathematical perspective.

FSI problems, such as the coupled water-wave and wind-turbine system considered here, are known to suffer from numerical instabilities as a result of coupling two inherently distinct problems, where different methods would suit better to solve the two subsystems. Instabilities depend on the domain size and the density of the structure (Causin et al., 2005; Förster et al., 2007). In general, numerical FSI solvers can be broadly divided into two types based on the coupling between the fluid and the structural equations. The first method is the monolithic approach in which the entire coupled system is solved at once. An alternative is to use partitioned solvers, which allow to treat the fluid and the structure in separation, see *e.g.* Benitz et al. (2015); Hübner et al. (2004). As will be shown, our algorithm involves elements of both categories. In the problem addressed, the two distinct subsystems are the nonlinear water-wave dynamics and the nonlinear beam dynamics, the former of which is described generally in terms of an Eulerian framework comprising an observer and mathematical coordinate system fixed in space, and the latter of which in

terms of a Lagrangian framework moving with the material of the wind-turbine mast.

In the standard approach, the problem is posed as a system of equations for separate domains augmented with coupling conditions. The novelty of our method is based on the fact that the coupled problem is posed in the form of a single functional. As a starting point, a variational principle (VP) for surface gravity waves is considered, described in Luke (1967); Miles (1977), coupled to a nonlinear elastic beam (van Brummelen et al., 2016). van Daalen et al. (1993) proposed a similar model, but for a point ship, rather than a continuous structure. The advantage of this approach is that the whole system is described by a single VP. A solution procedure for the linearized problem will be performed. The linear VP is first discretized directly in space with a finite element expansion. Subsequent discretization in time involves a reduction of the whole system to an abstract Hamiltonian form, to which known, stable discrete schemes can and will be applied. Variation of this algebraic VP then directly yields a so-called Galerkin finite element model, with mixed dis/continuous element approximations, an approach considered before in greater detail in Gagarina et al. (2014, 2016) and Bokhove and Kalogirou (2016). It shall be shown that, after returning to the original variables, the procedure results in the addition of novel regularization terms due to the fluid-beam coupling. The final discrete FSI system preserves conservative properties akin to the ones in the parent continuum system. Our numerical results for the linearized system indicate that our approach by construction yields, as anticipated, a stable numerical scheme.

The approach with Luke's VP involves an irrotational, incompressible, non-dissipative potential-flow fluid approximation that precludes the modelling of wave-breaking. Although mathematically interesting, the model has little use in realistic applications. Therefore an attempt is also made to extend the model so that wave-breaking can be simulated. One remains within the variational framework, yet compressible flow is allowed for and an equation of state is added that enables the simulation of a mixture of water and air phases, and thus (at the two-phase interface) also wave-breaking, which is the ultimate objective of this work.

1.3 Outline of the thesis

The thesis is organized as follows. Chapter 2 describes the model of the nonlinear elastic beam, both using an appropriate VP and with equations of motion. The VP is subsequently linearized and the linear and nonlinear models are compared. Chapter 3 deals with the coupling of the structure with a potential-flow fluid model. First, the VP for the potential flow is introduced. Second, the model of a fully coupled fluid-beam system is presented. The addition of a wavemaker to the formulation is discussed. Chapter 4 describes the solution of the coupled linear model. First, a nonlinear VP is linearized. Second, the Finite Element Method (FEM) is used to discretize the system in space. Third, the system is reduced to Hamiltonian form and a temporal discretization is applied. Both two-dimensional (2D) and three-dimensional (3D) results are presented. Firedrake (Rathgeber et al., 2016) is used extensively in our computations. Firedrake is an automated system for the solution of partial differential equations using the finite element method (FEM). Firedrake uses sophisticated code generation to provide mathematicians, scientists, and engineers with a very productive way to create sophisticated high performance simulations.

In Chapter 5, a new, irrotational compressible-fluid model is introduced with the purpose of simulating breaking waves impacting on an offshore wind turbine; the ultimate aim of this work. Three different equations of state are proposed, examined and the results are shown. Chapter 6 contains excerpts of the various Firedrake code implementations, which have been contributed as tutorials to the Firedrake website https://firedrakeproject.org/demos/linear_fluid_structure_interaction.py.html. Chapter 7 summarizes and concludes the thesis.

Chapter 2

Elastic beam: mathematical formulation and FEM

A fluid-structure interaction problem naturally consists of two sub-models. In this chapter, the focus is put on a description of the beam model used to describe the wind-turbine mast. First, the fully nonlinear model is formulated. Subsequently, it is linearized. Finally, numerical simulations of both the nonlinear model and its linearization are compared.

2.1 Nonlinear hyperelastic mast

Let us consider a nonlinear hyperelastic model for an elastic material in which the geometric nonlinearity of the displacements is taken into account. The latter geometric nonlinearity leads to the overall nonlinearity of the hyperelastic model (Temam and Miranville, 2005; van Brummelen et al., 2016). The constitutive law is such that, after linearization, it satisfies a linear Hooke's law. The choice of this model is guided by the goal of coupling the potential-flow water-wave model to either a weakly nonlinear hyperelastic or a linear elastic model. *A priori* it is not known whether the coupling between a nonlinear water-wave model and linear elasticity can lead to a consistent linear and (partially) nonlinear and conservative coupled model. Consequently, the starting point

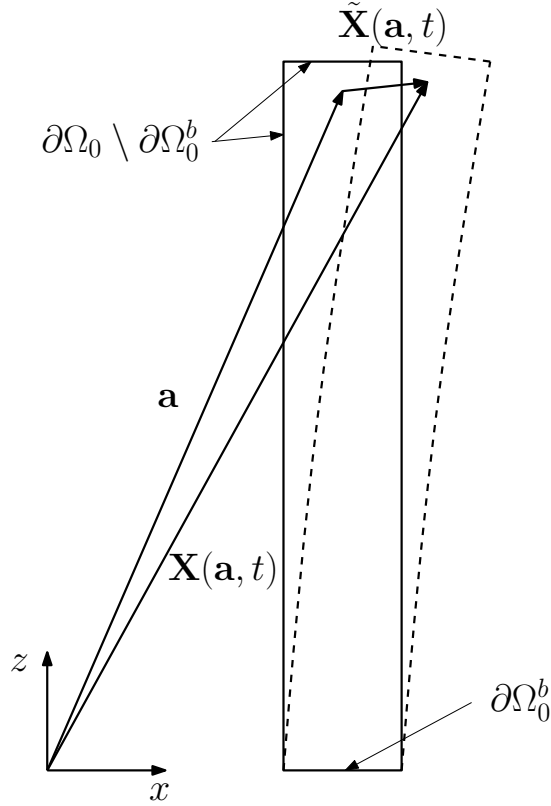


Figure 2.1: A sketch of the beam geometry, depicting a cross-section in the x - z plane, in which $\mathbf{a} = \mathbf{X}(\mathbf{a}, 0)$ is the Lagrangian coordinate in the reference state (boundary denoted by closed solid line); $\mathbf{X}(\mathbf{a}, t)$ is the position of a point in the deformed beam (boundary denoted by closed dashed line) and $\tilde{\mathbf{X}}(\mathbf{a}, t)$ its deflection; $\partial\Omega_0$ denotes the structure boundary and $\partial\Omega_0^b$ its fixed bottom.

is a fully nonlinear beam model. This question of modelling consistency will be discussed and addressed again at a later stage, after the analysis of our findings.

Let us first model the positions $\mathbf{X} = \mathbf{X}(a, b, c, t) = (X, Y, Z)^T = (X_1, X_2, X_3)^T$ of an infinitesimal 3D element of solid material as a function of Lagrangian coordinates $\mathbf{a} = (a, b, c)^T = (a_1, a_2, a_3)^T$ in the reference domain Ω_0 with boundary $\partial\Omega_0$ and time t . At time $t = 0$, $\mathbf{X}(\mathbf{a}, 0) = \mathbf{a}$ is taken, see Fig. 2.1. The displacements $\tilde{\mathbf{X}}$ follow from the positions as $\tilde{\mathbf{X}} = \mathbf{X} - \mathbf{a}$. The velocity of the displacements is $\partial_t \tilde{\mathbf{X}} = \partial_t \mathbf{X} = \mathbf{U} = (U_1, U_2, U_3)^T$, where the displacement velocity $\mathbf{U} = \mathbf{U}(\mathbf{a}, t)$ is again a function of Lagrangian coordinates \mathbf{a} and time t . The variational formulation of the elastic material follows closely the variational formulation of a linear elastic solid obeying

Hooke's law. However, the geometric movement makes the model nonlinear since the material is taken to be Lagrangian with finite rather than infinitesimal displacements. The variational formulation then comprises the kinetic and potential/internal energies, *i.e.*, $\rho_0|\mathbf{U}|^2/2$ and ρ_0gZ plus $W(\mathbf{E})$ with \mathbf{E} defined below, in the Lagrangian framework. Hence, the VP for the hyperelastic model in van Brummelen et al. (2016), adjusted to a format fitting our present purpose, becomes

$$0 = \delta \int_0^T \iiint_{\Omega_0} \rho_0 \partial_t \mathbf{X} \cdot \mathbf{U} - \frac{1}{2} \rho_0 |\mathbf{U}|^2 - \rho_0 g Z - W \, da \, db \, dc \, dt. \quad (2.1)$$

In (2.1), $\rho_0 = \rho_0(\mathbf{a})$ is a uniform material density and the internal, elastic energy W is defined as

$$W = \frac{1}{2} \lambda [\text{tr}(\mathbf{E})]^2 + \mu \text{tr}(\mathbf{E}^2), \quad (2.2)$$

in which λ and μ are material parameters called the first and second Lamé constants, respectively. The Lagrangian-Green strain tensor \mathbf{E} is defined by

$$\mathbf{E} = \frac{1}{2} (\mathbf{F}^T \cdot \mathbf{F} - \mathbf{I}), \quad (2.3)$$

where \mathbf{I} is the identity matrix and in which the deformation gradient \mathbf{F} , given by

$$\mathbf{F} = \frac{\partial \mathbf{X}}{\partial \mathbf{a}} = \frac{\partial(X, Y, Z)}{\partial(a, b, c)}, \quad \text{or equivalently} \quad F_{ij} = \frac{\partial X_i}{\partial a_j}, \quad \text{for } i, j = 1, 2, 3, \quad (2.4)$$

yields the determinant J between the Eulerian and Lagrangian frameworks that accounts for the geometric nonlinearity. The determinant J is given explicitly by

$$\begin{aligned} J = \det(\mathbf{F}) &\equiv \left| \frac{\partial(X, Y, Z)}{\partial(a, b, c)} \right| \\ &= X_a Y_b Z_c + Y_a Z_b X_c + Z_a X_b Y_c - X_c Y_b Z_a - Y_c Z_b X_a - Z_c X_b Y_a \end{aligned} \quad (2.5)$$

with subscripts denoting $X_a \equiv \partial_a X$, *etc.* A beam is modelled, which is fixed at the bottom $\partial\Omega_0^b$, defined here by $c = 0$ for $a \in [L_{a1}, L_{a2}]$ and $b \in [L_{b1}, L_{b2}]$, so that $\mathbf{X}(a, b, 0, t) = \mathbf{0}$,

which implies that $\delta \mathbf{X}|_{\partial\Omega_0^b} = \mathbf{0}$. Thus, evaluation of the variation in (2.1) yields

$$\begin{aligned}
 0 = & \int_0^T \iiint_{\Omega_0} \rho_0 (\partial_t \mathbf{X} - \mathbf{U}) \cdot \delta \mathbf{U} - \rho_0 \partial_t \mathbf{U} \cdot \delta \mathbf{X} - \rho_0 \delta_{l3} \delta X_l \\
 & + \partial_{a_i} (\lambda \operatorname{tr}(\mathbf{E}) F_{li} + 2\mu E_{ki} F_{lk}) \delta X_l \, da \, db \, dc \\
 & - \iint_{\partial\Omega_0 \setminus \partial\Omega_0^b} n_i (\lambda \operatorname{tr}(\mathbf{E}) F_{li} + 2\mu E_{ki} F_{lk}) \delta X_l \, dS \, dt, \quad (2.6)
 \end{aligned}$$

in which the temporal end-point conditions $\delta \mathbf{X}(0) = \delta \mathbf{X}(T) = \mathbf{0}$ have been used, as well as, from (2.3), the definitions

$$E_{ij} = \frac{1}{2} (F_{ki} F_{kj} - \delta_{ij}) = E_{ji} \quad \text{and} \quad \delta E_{ij} = \frac{1}{2} (F_{ki} \delta F_{kj} + F_{ki} \delta F_{kj}). \quad (2.7)$$

Given the arbitrariness of the respective variations, the resulting equations of motion, following directly from (2.6), become

$$\delta \mathbf{U} : \quad \partial_t \mathbf{X} = \mathbf{U} \quad \text{in } \Omega_0 \quad (2.8a)$$

$$\begin{aligned}
 \delta X_l : \quad \rho_0 \partial_t U_l &= -\rho_0 g \delta_{3l} + \partial_{a_i} (\lambda \operatorname{tr}(\mathbf{E}) F_{li} + 2\mu E_{ki} F_{lk}) \\
 &= -\rho_0 g \delta_{3l} + \partial_{a_i} T_{li} \quad \text{in } \Omega_0 \quad (2.8b)
 \end{aligned}$$

$$\delta X_l : \quad 0 = n_i (\lambda \operatorname{tr}(\mathbf{E}) F_{li} + 2\mu E_{ki} F_{lk}) = n_i T_{li} \quad \text{on } \partial\Omega_0 \setminus \partial\Omega_0^b \quad (2.8c)$$

with stress tensor $T_{li} = \lambda \operatorname{tr}(\mathbf{E}) F_{li} + 2\mu E_{ki} F_{lk}$.

2.2 Linearized elastic dynamics

Let us proceed with the linearization of (2.1), together with the transformation from a Lagrangian to an Eulerian description. Since the ultimate interest is in the dynamics of the fluid-structure interaction, the gravity term is neglected. Given (see Fig. 2.1) that

$\mathbf{X} = \mathbf{a} + \tilde{\mathbf{X}}$, expression (2.3) can be written as (Hunter, 1976)

$$\mathbf{E} = \frac{1}{2} \left(\left(\frac{\partial \tilde{\mathbf{X}}}{\partial \mathbf{a}} \right)^T + \left(\frac{\partial \tilde{\mathbf{X}}}{\partial \mathbf{a}} \right) \right) + \frac{1}{2} \left(\frac{\partial \tilde{\mathbf{X}}}{\partial \mathbf{a}} \right)^T \cdot \left(\frac{\partial \tilde{\mathbf{X}}}{\partial \mathbf{a}} \right). \quad (2.9)$$

The linearization entails the assumption that the displacement gradient is small compared to unity, *i.e.*, $\|\partial \tilde{\mathbf{X}}/\partial a\| \ll 1$, so that second- and higher-order terms can be neglected.

Therefore, the linearized version \mathbf{e} of \mathbf{E} is

$$\mathbf{e} = \frac{1}{2} \left(\left(\frac{\partial \tilde{\mathbf{X}}}{\partial \mathbf{a}} \right)^T + \left(\frac{\partial \tilde{\mathbf{X}}}{\partial \mathbf{a}} \right) \right) \quad \text{or} \quad e_{ij} = \frac{1}{2} \left(\frac{\partial \tilde{X}_j}{\partial a_i} + \frac{\partial \tilde{X}_i}{\partial a_j} \right). \quad (2.10)$$

Moreover, $\text{tr}(\mathbf{E})^2 = E_{ii}E_{jj} \approx e_{ii}e_{jj}$ and $\text{tr}(\mathbf{E} \cdot \mathbf{E}) = E_{ij}^2 \approx e_{ij}^2$, whence (2.1) becomes

$$0 = \delta \int_0^T \iiint_{\Omega_0} \rho_0 \partial_t \tilde{\mathbf{X}} \cdot \mathbf{U} - \frac{1}{2} \rho_0 |\mathbf{U}|^2 - \frac{1}{2} \lambda e_{ii} e_{jj} - \mu e_{ij}^2 \, da \, db \, dc \, dt, \quad (2.11)$$

in which the domain is, in a manner inconsistent with the linearization process, still the original moving domain Ω_0 . Since the fluid is described in the Eulerian framework, it is useful to work in the same coordinates with the structure, which, at the linear level, allows to use one unified Eulerian-or-Lagrangian coordinate system. Therefore (2.11) is transformed to Eulerian coordinates. For clarity, functions in Eulerian coordinates are momentarily annotated with a superscript $(\cdot)^E$ so that $f(\mathbf{a}) = f^E(\mathbf{x} = \mathbf{X}(\mathbf{a}))$. First, since $\mathbf{x} = \mathbf{X}(\mathbf{a}, t)$ and $\mathbf{X} = \mathbf{a} + \tilde{\mathbf{X}}$, let us note that

$$\frac{\partial \tilde{\mathbf{X}}}{\partial \mathbf{a}} = \frac{\partial \mathbf{X}}{\partial \mathbf{a}} \frac{\partial \tilde{\mathbf{X}}^E}{\partial \mathbf{x}} = \left(\mathbf{I} + \frac{\partial \tilde{\mathbf{X}}}{\partial \mathbf{a}} \right) \frac{\partial \tilde{\mathbf{X}}^E}{\partial \mathbf{x}} \quad (2.12)$$

and, hence, one finds that

$$\frac{\partial \tilde{\mathbf{X}}}{\partial \mathbf{a}} = \left(\mathbf{I} - \frac{\partial \tilde{\mathbf{X}}^E}{\partial \mathbf{x}} \right)^{-1} \frac{\partial \tilde{\mathbf{X}}^E}{\partial \mathbf{x}} \approx \frac{\partial \tilde{\mathbf{X}}^E}{\partial \mathbf{x}} \quad (2.13)$$

and

$$\mathbf{e} \approx \frac{1}{2} \left(\left(\frac{\partial \tilde{\mathbf{X}}^E}{\partial \mathbf{x}} \right)^T + \left(\frac{\partial \tilde{\mathbf{X}}^E}{\partial \mathbf{x}} \right) \right) = \mathbf{e}^E, \quad (2.14)$$

in which only linear terms are retained. Given that only quadratic terms have been retained in (2.11), its implied variation will yield linear equations of motion so that the Jacobian (2.5) of the transformation between Lagrangian and Eulerian frames can be approximated by $J \approx 1$. Consequently, the Eulerian form of the VP (2.11) is

$$0 = \delta \int_0^T \iiint_{\Omega_t} \rho_0 \partial_t \tilde{\mathbf{X}}^E \cdot \mathbf{U}^E - \frac{1}{2} \rho_0 |\mathbf{U}^E|^2 - \frac{1}{2} \lambda e_{ii}^E e_{jj}^E - \mu (e_{ij}^E)^2 dx dy dz dt, \quad (2.15)$$

in which the integration is still inconsistent, when taking into consideration the moving domain Ω_t . In the last step, we showed that, in the limit of small displacements, the integration must be performed over the fixed domain Ω_0^E as $\Omega_t = \Omega_0^E + \tilde{X}$, meaning that the deformed domain is the reference one subject to deformation. A small perturbation of a three-dimensional domain is considered on a length scale that is proportional to ϵ . One can write a general Taylor expansion of the integral in terms of ϵ

$$\begin{aligned} \int_{x_1+\epsilon\xi_1}^{x_2+\epsilon\xi_2} \int_{y_1+\epsilon\eta_1}^{y_2+\epsilon\eta_2} \int_{z_1+\epsilon\zeta_1}^{z_2+\epsilon\zeta_2} f(x, y, z) dz dy dx &= \int_{x_1}^{x_2} \int_{y_1}^{y_2} \int_{z_1}^{z_2} f(x, y, z) dz dy dx \\ &+ \epsilon \left(\int_{y_1}^{y_2} \int_{z_1}^{z_2} \xi_2 f(x_2, y, z) - \xi_1 f(x_1, y, z) dz dy \right. \\ &+ \int_{x_1}^{x_2} \int_{z_1}^{z_2} \eta_2 f(x, y_2, z) - \eta_1 f(x, y_1, z) dz dx \\ &\left. + \int_{x_1}^{x_2} \int_{y_1}^{y_2} \zeta_2 f(x, y, z_2) - \zeta_1 f(x, y, z_1) dy dx \right) + O(\epsilon^2). \end{aligned} \quad (2.16)$$

The displacement $\tilde{\mathbf{X}}$ can be treated as a small perturbation, with linear terms in ϵ in (2.16) translating to cubic terms in $\tilde{\mathbf{X}}$, $\tilde{\mathbf{U}}$ and $\partial_i \tilde{X}_j$ in (2.15). Therefore, retaining only quadratic terms and omitting for brevity the $(\cdot)^E$ superscript, *e.g.* in Ω_0^E , (2.15) becomes

$$0 = \delta \int_0^T \iiint_{\Omega_0} \rho_0 \partial_t \tilde{\mathbf{X}} \cdot \mathbf{U} - \frac{1}{2} \rho_0 |\mathbf{U}|^2 - \frac{1}{2} \lambda e_{ii} e_{jj} - \mu e_{ij}^2 dx dy dz dt. \quad (2.17)$$

In the limit of small displacement gradients, the following approximations hold

$$\text{tr}(\mathbf{E}) F_{li} = E_{jj} F_{li} \approx e_{jj} \delta_{li}, \quad E_{ki} F_{lk} \approx e_{ik} \delta_{lk} = e_{il}. \quad (2.18)$$

By either linearizing (2.8), neglecting the gravity term and using (2.18) or taking the variation of (2.11) (or (2.17)), the classical linearized equations of motion emerge as

$$\delta\mathbf{U} : \partial_t \tilde{\mathbf{X}} = \mathbf{U} \quad (2.19a)$$

$$\delta\tilde{X}_l : \rho_0 \partial_t U_l = \partial_{x_i} (\lambda e_{jj} \delta_{lj} + 2\mu e_{il}) \quad \text{in } \Omega_0 \quad (2.19b)$$

$$\delta\tilde{X}_l : 0 = n_i (\lambda e_{jj} \delta_{lj} + 2\mu e_{il}) \quad \text{on } \partial\Omega_0 \setminus \partial\Omega_0^b, \quad (2.19c)$$

in which Ω_0 denotes the fixed domain after linearization, with associated fixed boundary $\partial\Omega_0$ and fixed bottom $\partial\Omega_0^b$.

2.3 Numerical model

To solve partial differential equations numerically, one has to discretize them. For the spatial discretization and numerical implementation of the model, Firedrake is used (Rathgeber et al., 2016). The Firedrake environment requires partial differential equations to be defined in weak form, including the proper definition of the function spaces of the variables involved and the polynomial order and degrees of quadrature used. Let us abbreviate the spatial integral notion as $\iiint_{\Omega_0} \dots dx dy dz = \int \dots dV$. The weak form of equations (2.8), with \mathbf{v} as a test function, is

$$\int \partial_t \mathbf{X} \cdot \mathbf{v} dV = \int \mathbf{U} \cdot \mathbf{v} dV \quad (2.20a)$$

$$\int \partial_t \mathbf{U} \cdot \mathbf{v} dV = - \int \nabla_{\mathbf{v}} \Phi dV - \frac{1}{\rho_0} \int \nabla_{\mathbf{v}} W dV, \quad (2.20b)$$

in which have been used gravitational potential-energy density $\Phi = gZ$ and the directional derivative

$$\nabla_{\mathbf{v}}(\dots) = \mathbf{v} \cdot \frac{\partial(\dots)}{\partial \mathbf{X}}. \quad (2.21)$$

Equations (2.20) can be also derived directly from the VP (2.1). Using (2.1) and previously introduced notions one gets

$$0 = \delta \int_0^T \int \rho_0 \partial_t \mathbf{X} \cdot \mathbf{U} - \frac{1}{2} \rho_0 |\mathbf{U}|^2 - \rho_0 \Phi - W \, dV \, dt \quad (2.22a)$$

$$= \rho_0 \int_0^T \int \delta \mathbf{U} \cdot (\partial_t \mathbf{X} - \mathbf{U}) - \delta \mathbf{X} \cdot \left(\partial_t \mathbf{U} + g \frac{\partial \Phi}{\partial \mathbf{X}} + \frac{1}{\rho_0} \frac{\partial W}{\partial \mathbf{X}} \right) \, dV \, dt. \quad (2.22b)$$

(2.22b) contains equations (2.20) with appropriate variations instead of test functions. To ensure that variational structure is preserved in the discretization, we can first discretize the VP in space and then derive equations of motion. Using Einstein summation convention we can write

$$\mathbf{X}(\mathbf{x}, t) = \mathbf{X}_i(t) \varphi_i(\mathbf{x}) = (X^1, X^2, X^3)_i^T(t) \varphi_i(\mathbf{x}) \quad (2.23a)$$

$$\mathbf{U}(\mathbf{x}, t) = \mathbf{U}_i(t) \varphi_i(\mathbf{x}), \quad (2.23b)$$

in which functions are approximated with FE expansion in space, $\varphi_i(\mathbf{x})$ being basis functions. Inserting these expansions into (2.1) we get

$$0 = \delta \int_0^T \int \rho_0 \partial_t \mathbf{X}_i \cdot \mathbf{U}_j \varphi_i \varphi_j - \frac{1}{2} \rho_0 \mathbf{U}_i \cdot \mathbf{U}_j \varphi_i \varphi_j - \rho_0 g Z_i \varphi_i \quad (2.24a)$$

$$- X_i^a X_j^b W_{ij}^{ab} - X_i^a X_j^b X_k^c W_{ijk}^{abc} - X_i^a X_j^b X_k^c X_l^d W_{ijkl}^{abcd} \, dV \, dt. \quad (2.24b)$$

The exact form of tensor W will not be presented, as this is for conceptual illustration only. Taking variations

$$0 = \int_0^T \rho_0 \delta \mathbf{U}_i \cdot (\partial_t \mathbf{X}_j - \mathbf{U}_j) A_{ij} - \delta X_i^a \left(\rho_0 \partial_t \mathbf{U}_j^a A_{ij} + \rho_0 g B_i \delta^{a3} \right) \quad (2.25a)$$

$$+ X_j^b V_{ij}^{ab} + X_j^b X_k^c V_{ijk}^{abc} + X_j^b X_k^c X_l^d V_{ijkl}^{abcd} \, dt, \quad (2.25b)$$

in which $A_{ij} = \int \varphi_i \varphi_j \, dV$, $B_i = \int \varphi_i \, dV$ and tensor V arises from integrating W in space, but again, we will not specify their full form. Using the fact that the individual

variations are independent, we arrive at equations of motion discretized in space

$$\delta \mathbf{U}_i : A_{ij}(\partial_t \mathbf{X}_j - \mathbf{U}_j) = 0 \quad (2.26a)$$

$$\delta X_i^a : \rho_0 \partial_t \mathbf{U}_j^a A_{ij} = -\rho_0 g B_i \delta^{a3} - X_j^b V_{ij}^{ab} - X_j^b X_k^c V_{ijk}^{abc} - X_j^b X_k^c X_l^d V_{ijkl}^{abcd}. \quad (2.26b)$$

VP (2.25) contains their weak form

$$\delta \mathbf{U}_i \cdot (\partial_t \mathbf{X}_j - \mathbf{U}_j) A_{ij} = 0 \quad (2.27a)$$

$$\delta X_i^a \left(\rho_0 \partial_t \mathbf{U}_j^a A_{ij} + \rho_0 g B_i \delta^{a3} + X_j^b V_{ij}^{ab} + X_j^b X_k^c V_{ijk}^{abc} + X_j^b X_k^c X_l^d V_{ijkl}^{abcd} \right) = 0, \quad (2.27b)$$

which is also a space-discretized version of (2.20). Hence variational structure is ensured. Yet, as Firedrake performs space discretization for us, equations (2.20) in space-continuous form will be used thereafter. At this point (2.20) needs to be discretized in time. Therefore, some temporal schemes will be introduced and examined. They will be used both here and later in this work.

2.3.1 Time discretization schemes

As Hamiltonian systems are being solved, symplectic discretization schemes will be used that are designed for this purpose since they conserve energy (up to bounded oscillations) during time evolution.

Symplectic Euler scheme

Let us consider a system with a Hamiltonian $H(q, p)$. The equations of motion are

$$\begin{aligned} \partial_t q &= \nabla_p H(q, p) \\ \partial_t p &= -\nabla_q H(q, p). \end{aligned} \quad (2.28)$$

The general symplectic Euler scheme for this system is

$$\begin{aligned} q_{n+1} &= q_n + \Delta t \nabla_p H(q_{n+1}, p_n) \\ p_{n+1} &= p_n - \Delta t \nabla_q H(q_{n+1}, p_n) \end{aligned} \quad (2.29)$$

or

$$\begin{aligned} q_{n+1} &= q_n + \Delta t \nabla_p H(q_n, p_{n+1}) \\ p_{n+1} &= p_n - \Delta t \nabla_q H(q_n, p_{n+1}). \end{aligned} \quad (2.30)$$

Stability of the scheme for a harmonic oscillator $H(q, p) = \frac{1}{2}p^2 + \frac{1}{2}\omega^2q^2$ will be investigated now, for which (2.29) takes the form

$$\begin{aligned} q_{n+1} &= q_n + \Delta t p_n \\ p_{n+1} &= p_n - \omega^2 \Delta t q_{n+1}, \end{aligned} \quad (2.31)$$

which can be written in the implicit matrix form

$$\begin{pmatrix} 1 & 0 \\ \omega^2 \Delta t & 1 \end{pmatrix} \begin{pmatrix} q_{n+1} \\ p_{n+1} \end{pmatrix} = \begin{pmatrix} 1 & \Delta t \\ 0 & 1 \end{pmatrix} \begin{pmatrix} q_n \\ p_n \end{pmatrix} \quad (2.32)$$

with equivalent explicit matrix form

$$\begin{pmatrix} q_{n+1} \\ p_{n+1} \end{pmatrix} = \begin{pmatrix} 1 & \Delta t \\ -\omega^2 \Delta t & 1 - \omega^2 \Delta t^2 \end{pmatrix} \begin{pmatrix} q_n \\ p_n \end{pmatrix}. \quad (2.33)$$

The scheme (2.31) is unconditionally/conditionally stable provided the eigenvalues λ of the amplification matrix in (2.33) lie within/on the unit disc in the complex λ plane. In the present case all λ are real, so $-1 \leq \lambda \leq 1$. The required λ are the roots of the characteristic polynomial

$$\lambda^2 + \lambda(\omega^2 \Delta t^2 - 2) + 1 = 0, \quad (2.34)$$

which yields

$$\lambda = \frac{1}{2} \left(2 - \omega^2 \Delta t^2 \pm \omega \Delta t \sqrt{\omega^2 \Delta t^2 - 4} \right). \quad (2.35)$$

Equation (2.35), together with the condition $|\lambda| \leq 1$, give the stability criterion

$$|\omega \Delta t| \leq 2. \quad (2.36)$$

Although the system is nonlinear, based on this criterion one can still estimate a neutrally stable timestep so that the oscillations related to the finite mesh resolution are not amplified; unfortunately, neither are they reduced due to the neutral stability of the scheme. The maximal $\omega = ck$ is given by the largest wave propagation speed c (speed of sound in water in our case) and a wave vector $k = 2\pi/\lambda_w$ related to shortest wavelength $\lambda_w = 2\Delta x$, in which Δx is the smallest distance between the mesh nodes. Accordingly, one obtains

$$\Delta t \leq \frac{2\Delta x}{\pi c}. \quad (2.37)$$

Störmer-Verlet scheme

An alternative to symplectic Euler scheme is the Störmer-Verlet scheme, which includes a half-step calculation and, for (2.28), takes the form (Leimkuhler and Reich, 2004)

$$\begin{aligned} q_{n+1/2} &= q_n + \frac{\Delta t}{2} \nabla_p H(q_{n+1/2}, p_n) \\ p_{n+1} &= p_n - \Delta t \nabla_q H(q_{n+1/2}, p_{n+1}) \\ q_{n+1} &= q_{n+1/2} + \frac{\Delta t}{2} \nabla_p H(q_{n+1}, p_{n+1}) \end{aligned} \quad (2.38)$$

or

$$\begin{aligned} p_{n+1/2} &= p_n - \frac{\Delta t}{2} \nabla_q H(q_n, p_{n+1/2}) \\ q_{n+1} &= q_n + \Delta t \nabla_p H(q_n, p_{n+1/2}) \\ p_{n+1} &= p_n - \frac{\Delta t}{2} \nabla_q H(q_{n+1}, p_{n+1}). \end{aligned} \quad (2.39)$$

A linear stability analysis leads to the same criterion (2.37) as in the symplectic-Euler case.

Implicit midpoint scheme

The implicit midpoint scheme for system (2.28) is

$$\begin{aligned} q_{n+1} &= q_n + \Delta t \nabla_p H\left(\frac{q_n + q_{n+1}}{2}, \frac{p_n + p_{n+1}}{2}\right) \\ p_{n+1} &= p_n - \Delta t \nabla_q H\left(\frac{q_n + q_{n+1}}{2}, \frac{p_n + p_{n+1}}{2}\right), \end{aligned} \quad (2.40)$$

which, for the harmonic oscillator, takes the form

$$\begin{aligned} q_{n+1} &= q_n + \frac{1}{2} \Delta t (p_n + p_{n+1}) \\ p_{n+1} &= p_n - \frac{1}{2} \omega^2 \Delta t (q_n + q_{n+1}). \end{aligned} \quad (2.41)$$

In matrix notation (2.41) becomes, in implicit form,

$$\begin{pmatrix} 2 & -\Delta t \\ \omega^2 \Delta t & 2 \end{pmatrix} \begin{pmatrix} q_{n+1} \\ p_{n+1} \end{pmatrix} = \begin{pmatrix} 2 & \Delta t \\ -\omega^2 \Delta t & 2 \end{pmatrix} \begin{pmatrix} q_n \\ p_n \end{pmatrix} \quad (2.42)$$

and hence, in explicit form,

$$\begin{pmatrix} q_{n+1} \\ p_{n+1} \end{pmatrix} = \frac{1}{4 + \omega^2 \Delta t} \begin{pmatrix} 4 & \Delta t^2 \\ \omega^4 \Delta t^2 & 4 \end{pmatrix} \begin{pmatrix} q_n \\ p_n \end{pmatrix}. \quad (2.43)$$

The roots of the characteristic polynomial of the system matrix (2.43) are

$$\lambda_1 \equiv 1, \quad \lambda_2 = \frac{4 - \omega^2 \Delta t^2}{4 + \omega^2 \Delta t^2}, \quad (2.44)$$

both of which fulfil the condition $|\lambda| \leq 1$ for all Δt . Therefore the implicit midpoint scheme is unconditionally stable.

2.3.2 Discretization and implementation

The symplectic Euler scheme applied to equations (2.20) yields

$$\int \mathbf{X}^{n+1} \cdot \mathbf{v} \, dV = \int \mathbf{X}^n \cdot \mathbf{v} \, dx + \Delta t \int \mathbf{U}^n \cdot \mathbf{v} \, dV \quad (2.45a)$$

$$\int \mathbf{U}^{n+1} \cdot \mathbf{v} \, dV = \int \mathbf{U}^n \cdot \mathbf{v} \, dx - \Delta t \int \nabla_{\mathbf{v}} \Phi \, dV - \frac{\Delta t}{\rho} \int \nabla_{\mathbf{v}} W^{n+1} \, dV. \quad (2.45b)$$

A specific property of system (2.45) is that, although the model is nonlinear, the sole nonlinearity resides in the internal, elastic energy, *i.e.*, the term $W(\mathbf{E})$, which is evaluated at a known time level. That is, despite the mathematical nonlinearity, the numerical solvers are explicit. This is a consequence of the Hamiltonian in (2.1) being a sum of a position-dependent potential energy and a velocity-dependent kinetic energy. In Firedrake, the weak forms (2.45) are directly implemented as given. The function space used for \mathbf{X} and \mathbf{U} is the linear continuous Galerkin. The finite element method itself is described in more detail in Chapter 4, where it is necessary for derivation. Here it is sufficient to rely on Firedrake's implementation.

2.4 Results

To see the difference between the linear- and nonlinear-beam models, a straightforward case is examined. Consider a block of dimensions $2 \times 2 \times 20\text{m}$ made of material with density 7700kg/m^3 and Lamé parameters $\lambda = \mu = 10^7 \text{ N/m}^2$, discretized into $4 \times 4 \times 20$ finite element blocks, each consisting of 6 tetrahedra, *cf.* Fig. 2.2.

Essentially, the difference between the two models' implementation boils down to the expression for the Green-Lagrangian strain tensor, *cf.* (2.9) and (2.10). The nonlinear model contains an extra quadratic term which is omitted in the linear model. As a result, the potential energy has additional higher-order terms in the nonlinear model. Hence, the total energy is larger for the nonlinear model, which is visible in Fig. 2.3.

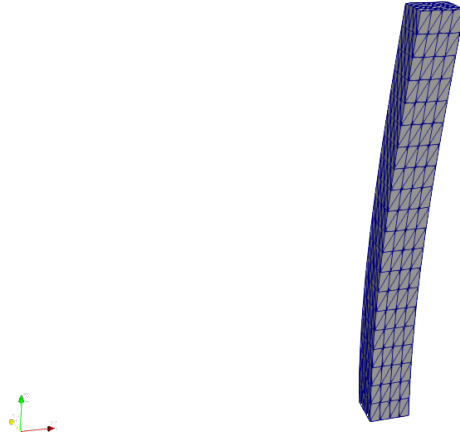


Figure 2.2: Initial state of the (non)linear beam test case.

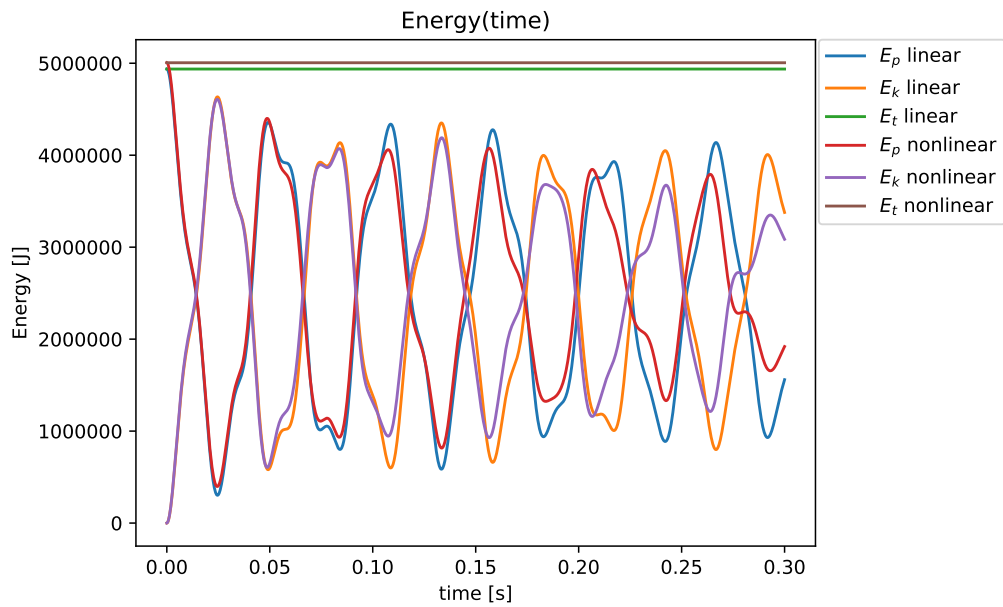


Figure 2.3: The energy partition of the evolving system as function of time for both the linear and nonlinear model. In the legend, E_p denotes potential energy, E_k kinetic energy and E_t the total energy.

The difference between the two models is visualized more clearly in Fig. 2.4, which shows that the difference in potential energy between the two models is an increasing function of time. This growth occurs because the frequencies of oscillations in the two models start

to deviate due to nonlinear interactions that develop in time.

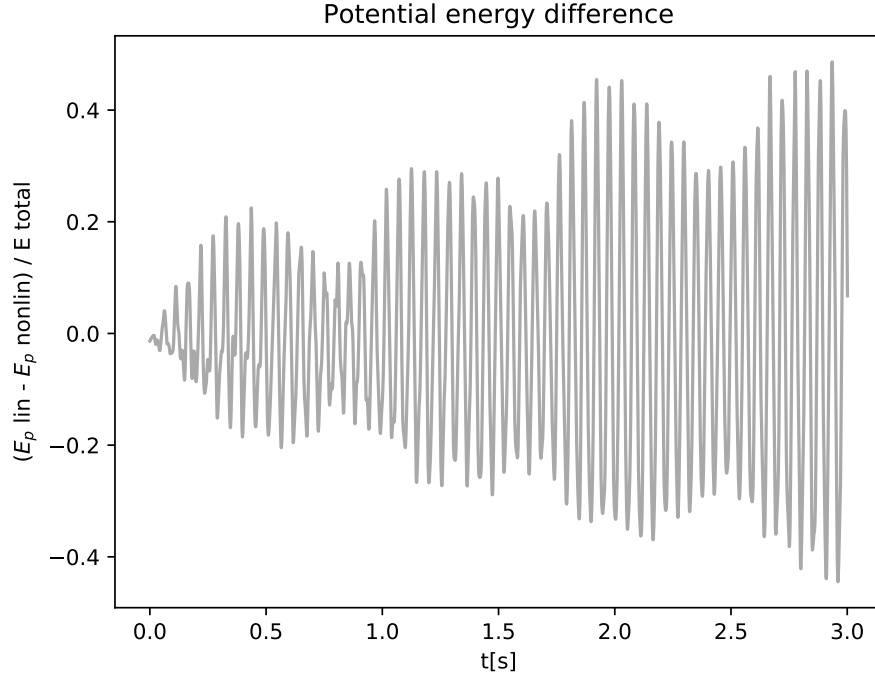


Figure 2.4: The difference between the linear and nonlinear potential energy scaled by the total energy as a growing function of time.

2.4.1 Conclusions

A nonlinear hyperelastic beam model and its linearization have been introduced. Subsequently, a continuous Galerkin finite-element method has been used to discretize both systems and a first-order symplectic time integrator. The linear finite-element model is the building block for the coupled (linear) water-wave and elastic-beam models investigated in the next two chapters. One less satisfactory aspect, which will also turn-up in the coupled model, is an inconsistency in the linearization because gravity in the calculation of the basic, rest state, was ignored. However, strictly speaking the beam needs to be subjected to a hydrostatic pressure distribution (or on one side in two dimensions). This inconsistency in the linearization is generally ignored in the continuum-mechanics literature, see *e.g.* Antman (1995); Temam and Miranville (2005). Linearization should

take place around the proper lithostatic rest state, for a nearly incompressible solid subject to a hydrostatic pressure. The problem likely requires a numerical calculation of the nonlinear lithostatic state, but that can readily be done with our numerical model, and a subsequent linearization around this rest state, which will include the numerical determination of certain material parameters emerging in the linear model. Such a procedure is standard practice in fluid mechanics (Temam and Miranville, 2005). For the coupled model, such an extension is important because the rest state for the water-wave domain will –indeed– be hydrostatic. In addition, one can make an asymptotic analysis for a nearly incompressible solid and compare this with a linearization around a case without gravity and without hydrostatic pressure forcing.

Chapter 3

Nonlinear variational modelling of wave-structure interactions

In this chapter a model is formulated, expressed in terms of a single functional, for Fluid-Structure Interaction (FSI) consisting of the hyperelastic beam considered in last chapter, a potential-flow fluid, and the coupling between these two sub-models. The linearization of this system and the solution of the linearized system is the topic of the next chapter.

3.1 Potential-flow water waves

Water is hereafter considered as an incompressible fluid with density ρ . The vector velocity field $\mathbf{u} = \mathbf{u}(x, y, z, t)$ has zero divergence, $\nabla \cdot \mathbf{u} = 0$, with spatial coordinates $\mathbf{x} = (x, y, z)^T$ and time coordinate t . Gravity acts in the negative z -direction and the associated acceleration of gravity is g . The velocity is expressed in terms of a scalar potential $\phi = \phi(x, y, z, t)$ such that $\mathbf{u} = \nabla\phi$. Flow is considered in the 3D Cartesian domain Ω (see Fig. 3.1) bounded by solid walls at $x = 0$, $x = L_x$, $y = 0$, $y = L_y$ and the flat bottom at $z = 0$. The upper surface of Ω is given by the single-valued evolving free surface $z = h(x, y, t)$, and hence $\Omega = [0, L_x] \times [0, L_y] \times [0, h(x, y, t)]$, within which

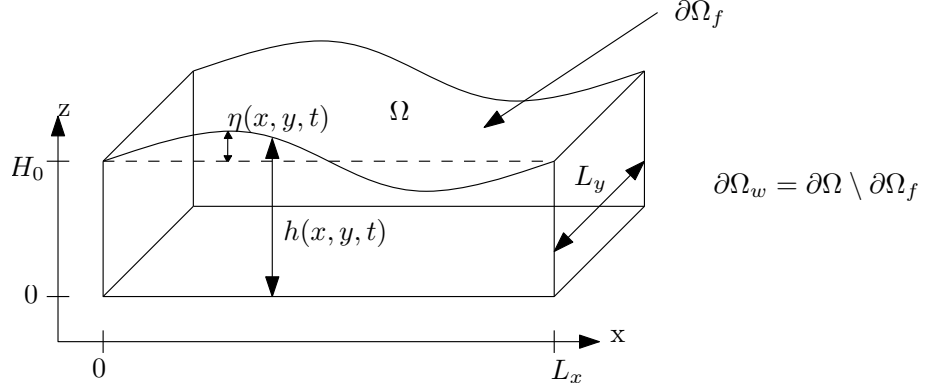


Figure 3.1: Geometry of the fluid domain: a box with rest-state dimensions $L_x \times L_y \times H_0$ and evolving free surface $z = H_0 + \eta(x, y, t) = h(x, y, t)$. Here $\eta(x, y, t)$ is the free-surface perturbation from the rest state that first appears in (4.2).

Luke's variational principle (VP) (Luke, 1967) for potential-flow water waves reads

$$\begin{aligned}
 0 &= \delta \int_0^T \iiint_{\Omega} -\rho \partial_t \phi \, d\Omega - \mathcal{H} \, dt \\
 &\equiv \delta \int_0^T \int_0^{L_x} \int_0^{L_y} \int_0^{h(x,y,t)} -\rho \left(\partial_t \phi + \frac{1}{2} |\nabla \phi|^2 + g(z - H_0) \right) dz \, dy \, dx \, dt, \quad (3.1)
 \end{aligned}$$

in which H_0 is the rest-state water level. The energy or Hamiltonian \mathcal{H} consists of the sum of kinetic and potential energies. Integration by parts in time is used together with Gauss' law with outward normal $\mathbf{n} = (-\nabla_{\perp} h, 1)^T / \sqrt{1 + |\nabla_{\perp} h|^2}$ at the free surface, in which $\nabla_{\perp} = (\partial_x, \partial_y)$. The passive and constant air pressure is denoted by p_a . Then, variation of (3.1) yields

$$\begin{aligned}
 0 &= \int_0^T \int_0^{L_x} \int_0^{L_y} \int_0^{h(x,y,t)} \rho \nabla^2 \phi \, \delta \phi \, dz \, dy \, dx - \int_{\partial\Omega_w} \rho \nabla \phi \cdot \mathbf{n} \, \delta \phi \, dS \\
 &\quad + \int_0^{L_x} \int_0^{L_y} \rho \left(-\partial_z \phi + \partial_x \phi \partial_x h + \partial_y \phi \partial_y h + \partial_t h \right) \Big|_{z=h} \delta \phi \Big|_{z=h} \\
 &\quad + (p - p_a)_{z=h} \delta h \, dy \, dx \, dt, \quad (3.2)
 \end{aligned}$$

in which the pressure difference $p - p_a$ here acts as a shorthand placeholder for the Bernoulli expression $-\rho(\partial_t \phi + \frac{1}{2} |\nabla \phi|^2 + g(z - H_0))$ and $\partial\Omega_w$ denotes the solid-wall and bottom boundaries.

The equations of motion emerge from relation (3.2), augmented by the following no-normal-flow boundary conditions $\mathbf{n} \cdot \nabla\phi = 0$ on $\partial\Omega_w$, with unit outward normal \mathbf{n} at solid walls and bottom $\partial\Omega_w$, as follows

$$\begin{aligned}
 & x \in [0, L_x], y \in [0, L_y], z \in [0, h]; \\
 & \delta\phi : 0 = -\rho\nabla^2\phi = \frac{\delta\mathcal{H}}{\delta\phi} \\
 & x \in [0, L_x], y \in [0, L_y], z = h(x, y, t); \\
 & (\delta\phi)_h : \partial_t h = -\partial_x\phi \partial_x h + \partial_z\phi = \frac{\delta\mathcal{H}}{(\delta\phi)_h} \tag{3.3} \\
 & x \in [0, L_x], y \in [0, L_y], z = h(x, y, t); \\
 & \delta h : \rho\partial_t\phi = -\frac{1}{2}\rho|\nabla\phi|^2 - \rho g(h - H_0) = -\frac{\delta\mathcal{H}}{\delta h}.
 \end{aligned}$$

The above equations can be extended to include a wavemaker, see equations (6) in Gagarina et al. (2014) or (3.3) in Gidel (2018).

3.2 Coupled model

At any given time, the domain occupied by the fluid is denoted by Ω and the reference domain occupied by the hyperelastic material by Ω_0 . For simplicity, a block shape of hyperelastic material is considered. The interface between the fluid and solid domains is parameterized by $\mathbf{X}_s = \mathbf{X}(L_s, b, c, t)$ and, at rest, $\mathbf{X} = \mathbf{a}$ for Cartesian $a \in [L_s, L_x]$, $b \in [0, L_y]$, $c \in [0, L_z]$, while the fluid domain at rest is $x \in [0, L_s]$, $y \in [0, L_y]$, $z \in [0, H_0]$. The (outward-from-fluid) unit normal at this interface $\mathbf{X}(L_s, b, c, t)$, with $b \in [0, L_y]$, $c \in [0, L_z]$, is $\mathbf{n} = \partial_b\mathbf{X} \times \partial_c\mathbf{X} / |\partial_b\mathbf{X} \times \partial_c\mathbf{X}|$. A schematic diagram of the domain at rest is given in Fig. 3.2, and, hence, the last expression is for the outward normal to the fluid domain at the fluid-structure interface.

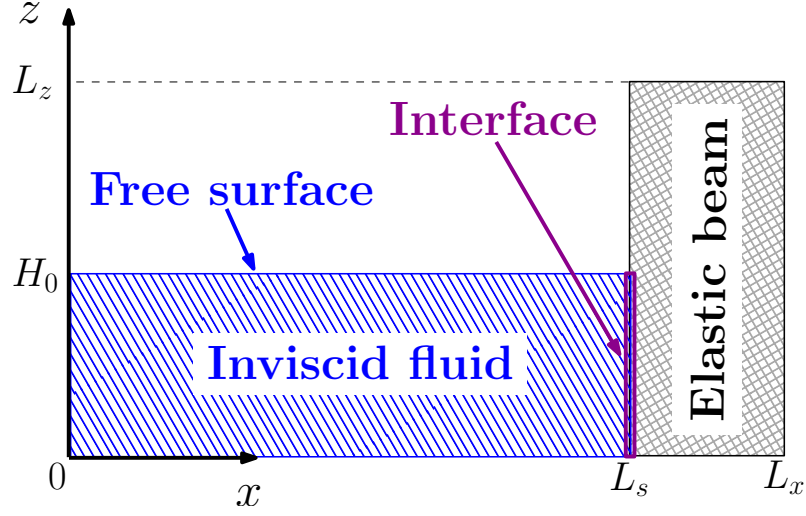


Figure 3.2: Geometry of the linearized or rest system: fluid (hatched) and elastic beam (cross-hatched). This 2D representation is in the $y = 0$ plane, with the y -axis directed into the page, in which direction the full 3D configuration has uniform depth L_y .

The moving fluid and elastic domains are defined by

$$\Omega: \quad x \in (0, x_s(y, z, t)), \quad y \in (0, L_y), \quad z \in (0, h(x, y, t)); \quad (3.4a)$$

$$\Omega_0: \quad a \in (L_s, L_x), \quad b \in (0, L_y), \quad c \in (0, L_z), \quad (3.4b)$$

in which $x_s = x_s(y, z, t)$ is a new variable that describes the position of the moving fluid boundary. Since it is at the structure surface, a Lagrange multiplier $\gamma = \gamma(b, c, t)$ is used to equate $x_s(y = Y(L_s, b, c, t), z = Z(L_s, b, c, t), t)$ to $X(L_s, b, c, t)$. For the coupled fluid-structure VP, the sum is taken of the two VPs, and augmented with the Lagrange-multiplier term as follows:

$$\begin{aligned} 0 = & \delta \int_0^T \iiint_{\Omega} -\rho \left(\partial_t \phi + \frac{1}{2} |\nabla \phi|^2 + g(z - H_0) \right) dx dy dz \\ & + \int_0^{L_y} \int_0^{L_z} \rho \gamma \left(x_s(Y(L_s, b, c, t), Z(L_s, b, c, t), t) - X(L_s, b, c, t) \right) dc db \quad (3.5) \\ & + \iiint_{\Omega_0} \rho_0 \partial_t \mathbf{X} \cdot \mathbf{U} - \frac{1}{2} \rho_0 |\mathbf{U}|^2 - \rho_0 g Z - \frac{1}{2} \lambda [\text{tr}(\mathbf{E})]^2 - \mu \text{tr}(\mathbf{E}^2) da db dc dt. \end{aligned}$$

Note that the waterline height z at the fluid-beam interface is implicitly defined by

$z = h(x_s(y, z, t), y, t)$, even for the non-breaking waves considered. To avoid the implicit definition, and because it is here easier to work in a fixed domain, a new horizontal coordinate $\chi = L_s x / x_s(y, z, t)$ is introduced before applying the coordinate transformation

$$\chi = L_s x / x_s(y, z, t), \quad y' = y, \quad z' = z, \quad t' = t$$

such that the fluid domain Ω is now redefined as $\chi \in (0, L_s)$, $y' \in (0, L_y)$, $z' \in (0, h(\chi, y, t))$. Both x_s and χ are indicated in Fig. 3.3. The following transformation

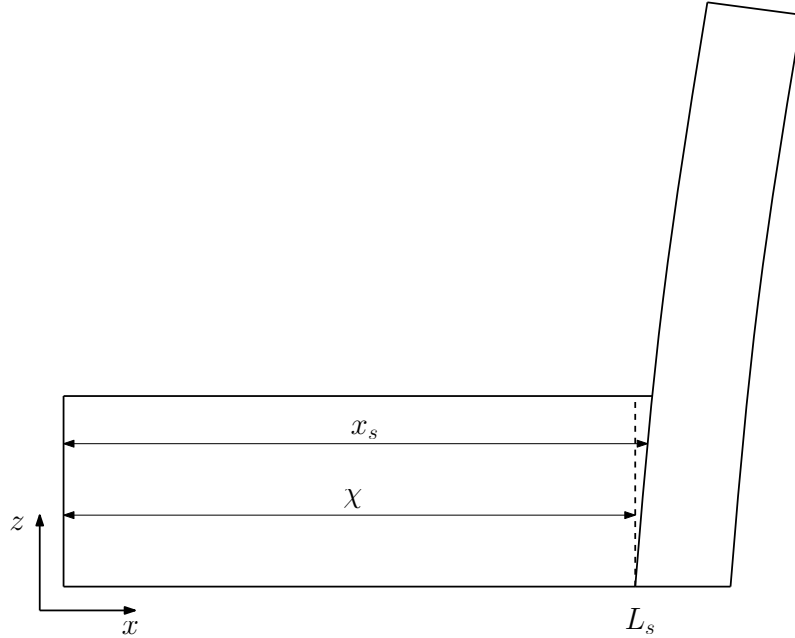


Figure 3.3: Definition of the variables used in the VP transformation. Here $x_s(y, z, t)$ denotes the position of the fluid-structure interface and $\chi = L_s x / x_s(y, z, t)$ denotes the transformation of the domain to one whose dimension is fixed in the x -direction. A cross-section perpendicular to the y -direction is shown.

rules are required to transform the VP

$$\partial_x = \frac{\partial \chi}{\partial x} \partial_\chi + \frac{\partial y'}{\partial x} \partial_{y'} + \frac{\partial z'}{\partial x} \partial_{z'} + \frac{\partial t'}{\partial x} \partial_{t'} = \frac{L_s}{x_s} \partial_\chi \quad (3.6a)$$

$$\partial_y = \frac{\partial \chi}{\partial y} \partial_\chi + \frac{\partial y'}{\partial y} \partial_{y'} + \frac{\partial z'}{\partial y} \partial_{z'} + \frac{\partial t'}{\partial y} \partial_{t'} = -\frac{\chi}{x_s} \frac{\partial x_s}{\partial y} \partial_\chi + \partial_{y'} \quad (3.6b)$$

$$\partial_z = \frac{\partial \chi}{\partial z} \partial_\chi + \frac{\partial y'}{\partial z} \partial_{y'} + \frac{\partial z'}{\partial z} \partial_{z'} + \frac{\partial t'}{\partial z} \partial_{t'} = -\frac{\chi}{x_s} \frac{\partial x_s}{\partial z} \partial_\chi + \partial_{z'} \quad (3.6c)$$

$$\partial_t = \frac{\partial \chi}{\partial t} \partial_\chi + \frac{\partial y'}{\partial t} \partial_{y'} + \frac{\partial z'}{\partial t} \partial_{z'} + \frac{\partial t'}{\partial t} \partial_{t'} = -\frac{\chi}{x_s} \frac{\partial x_s}{\partial t} \partial_\chi + \partial_{t'} \quad (3.6d)$$

$$dx dy dz dt = \frac{x_s}{L_s} d\chi dy' dz' dt'. \quad (3.6e)$$

Due to numerical equality of primed and unprimed y, z and t , primes can be dropped. Then, in this new coordinate system, VP (3.5) becomes

$$\begin{aligned} 0 = & \delta \int_0^T \int_0^{L_s} \int_0^{L_y} \int_0^{h(\chi, y, t)} -\rho \left(-\frac{\chi}{L_s} \partial_t x_s \partial_\chi \phi + \frac{x_s}{L_s} \partial_t \phi \right. \\ & + \frac{1}{2} \frac{L_s}{x_s} (\partial_\chi \phi)^2 + \frac{1}{2} \frac{x_s}{L_s} \left(-\frac{\chi}{x_s} \partial_y x_s \partial_\chi \phi + \partial_y \phi \right)^2 \\ & + \frac{1}{2} \frac{x_s}{L_s} \left(-\frac{\chi}{x_s} \partial_z x_s \partial_\chi \phi + \partial_z \phi \right)^2 + g(z - H_0) \frac{x_s}{L_s} \Big) dz dy d\chi \\ & + \int_0^{L_y} \int_0^{L_z} \rho \gamma \left(x_s(Y(L_s, b, c, t), Z(L_s, b, c, t), t) - X(L_s, b, c, t) \right) dc db \\ & + \int_{L_s}^{L_x} \int_0^{L_y} \int_0^{L_z} \rho_0 \partial_t \mathbf{X} \cdot \mathbf{U} - \frac{1}{2} \rho_0 |\mathbf{U}|^2 - \rho_0 g Z - \frac{1}{2} \lambda [\text{tr}(\mathbf{E})]^2 - \mu \text{tr}(\mathbf{E}^2) dc db da dt. \end{aligned} \quad (3.7)$$

3.2.1 Conclusions

In this chapter, the variational principle governing the nonlinear dynamics of the coupled water-wave and hyperelastic-beam motions has been derived. The simplified version of this comprehensive variational principle governing the linear dynamics will be derived in the next chapter and will form the basis of our monolithic finite-element numerical discretization of the coupled system. Since this linearized model was our first focus of attention, the complete nonlinear equations of motion of the coupled model have not been derived. It is recommended as future work in addition to extending the overall dynamics with a wavemaker of the waveflap type, such as used at MARIN.

Chapter 4

Linear variational modelling of wave-structure interactions: finite-element method

4.1 Introduction

The variational principle governing the nonlinear dynamics of the coupled water-wave and hyperelastic-beam motions derived in the previous chapter is now developed into an implemented algorithmic form. As indicated in the conclusions immediately above, consideration of the full, nonlinear problem is deferred to future work. Accordingly, the objectives of the current chapter are threefold.

First, a simplified version of the variational principle is formulated on the basis of considering only the linearized dynamics of the nonlinear coupled model. Second, a discretization is sought of the linearized coupled model via a direct space-time discretization of the simplified variational principle, attention being taken to ensure that the variation thereof directly leads to a robust, stable and accurate discretization of the entire coupled system.

Finally, the resulting spatio-temporal discretization of the linear coupled water-wave and elastic-beam dynamics is implemented. Spatial discretization is performed following a transformation of the system into an intermediate Hamiltonian form, and temporal discretization is undertaken using a total-energy-preserving Störmer-Verlet scheme (Leimkuhler and Reich, 2004). Computations were performed using both bespoke code and Firedrake (Rathgeber et al., 2016) employing finite elements, and the formulation verified and codes validated by numerical simulations in both two and three dimensions of water waves impacting on a steel monopile.

The chapter concludes with a discussion of extensions of the model that are able to accommodate breaking waves.

4.2 Linearization of the variational principle

The starting point is the transformed VP obtained at the end of previous chapter

$$0 = \delta \int_0^T \int_0^{L_s} \int_0^{L_y} \int_0^{h(\chi, y, t)} -\rho \left(-\frac{\chi}{L_s} \partial_t x_s \partial_\chi \phi + \frac{x_s}{L_s} \partial_t \phi \right) \quad (4.1a)$$

$$+ \frac{1}{2} \frac{L_s}{x_s} (\partial_\chi \phi)^2 + \frac{1}{2} \frac{x_s}{L_s} \left(-\frac{\chi}{x_s} \partial_y x_s \partial_\chi \phi + \partial_y \phi \right)^2 \quad (4.1b)$$

$$+ \frac{1}{2} \frac{x_s}{L_s} \left(-\frac{\chi}{x_s} \partial_z x_s \partial_\chi \phi + \partial_z \phi \right)^2 + g(z - H_0) \frac{x_s}{L_s} \Big) dz dy d\chi \quad (4.1c)$$

$$+ \int_0^{L_y} \int_0^{L_z} \rho \gamma \left(x_s (Y(L_s, b, c, t), Z(L_s, b, c, t), t) - X(L_s, b, c, t) \right) dc db \quad (4.1d)$$

$$+ \int_{L_s}^{L_x} \int_0^{L_y} \int_0^{L_z} \rho_0 \partial_t \mathbf{X} \cdot \mathbf{U} - \frac{1}{2} \rho_0 |\mathbf{U}|^2 - \rho_0 g Z - \frac{1}{2} \lambda [\text{tr}(\mathbf{E})]^2 - \mu \text{tr}(\mathbf{E}^2) dc db da dt. \quad (4.1e)$$

Equation (4.1) is first linearized around a state of rest. Small-amplitude perturbations around this rest state are introduced as follows

$$x_s = L_s + \tilde{x}_s, \quad \phi = 0 + \phi, \quad h = H_0 + \eta, \quad \mathbf{X} = \mathbf{x} + \tilde{\mathbf{X}}, \quad \mathbf{U} = \mathbf{0} + \mathbf{U}, \quad \gamma = 0 + \gamma. \quad (4.2)$$

Some of the terms in (4.1) can be simplified as follows. First considered is the term in (4.1a)

$$\int_0^{L_s} \int_0^{L_y} \int_0^{H_0+\eta} \rho \frac{\chi}{L_s} \partial_t \tilde{x}_s \partial_\chi \phi - \rho \frac{L_s + \tilde{x}_s}{L_s} \partial_t \phi \, dz \, dy \, d\chi \, dt \quad (4.3a)$$

$$\begin{aligned} &= \int_0^{L_s} \int_0^{L_y} \int_0^{H_0+\eta} -\frac{\rho}{L_s} \partial_t \tilde{x}_s \partial_\chi \phi + \frac{\rho}{L_s} \partial_t \tilde{x}_s \partial_\chi \phi \\ &\quad + \frac{\rho}{L_s} \partial_\chi (\chi \phi) \partial_t \tilde{x}_s - \frac{\rho}{L_s} \partial_t ((L_s + \tilde{x}_s) \phi) \, dz \, dy \, d\chi \end{aligned} \quad (4.3b)$$

$$\begin{aligned} &= \int_0^{L_y} \int_0^{H_0+\eta} \rho \phi_s \partial_t \tilde{x}_s \, dz \, dy + \int_0^{L_s} \int_0^{L_y} \frac{\rho}{L_s} (L_s + \tilde{x}_s) \phi_f \partial_t \eta \, dy \, d\chi \\ &\quad - \frac{d}{dt} \int_0^{L_s} \int_0^{L_y} \int_0^{H_0+\eta} \frac{\rho}{L_s} x_s \phi \, dz \, dy \, d\chi, \end{aligned} \quad (4.3c)$$

in which Leibniz' rule has been used to yield the time derivative of the integral, and then the integral taken of the derivative with respect to χ , thereby obtaining the final term in (4.3c) as a total time derivative. Temporal integration of this, upon using the conditions $\delta\phi(0) = \delta\phi(T) = 0$ and $\delta x_s(0) = \delta x_s(T) = 0$, yields a variation in (3.7) of zero. Therefore this term can be neglected. The remaining two terms in (4.3c) are now linearized *i.e.* terms of third and higher order are similarly neglected, since quadratic terms in the VP give linear terms in the equations of motion. Thus, the second term in (4.3c) becomes

$$\int_0^{L_s} \int_0^{L_y} \frac{\rho}{L_s} (L_s + \tilde{x}_s) \phi_f \partial_t \eta \, dy \, d\chi \approx \int_0^{L_s} \int_0^{L_y} \rho \phi_f \partial_t \eta \, dy \, d\chi. \quad (4.4)$$

For the first term in (4.3c), Taylor-expansion around H_0 yields

$$\int_0^{L_y} \int_0^{H_0+\eta} \rho \phi_s \partial_t \tilde{x}_s \, dz \, dy \approx \int_0^{L_y} \int_0^{H_0} \rho \phi_s \partial_t \tilde{x}_s \, dz \, dy. \quad (4.5)$$

The zeroth order of the expansion is sufficient, as the first order already contains cubic terms. The definitions of the velocity potentials $\phi_s = \phi(L_s, y, z, t)$ and $\phi_f = \phi(\chi, y, h(\chi, y, t), t)$ are used at the beam interface and the free surface respectively. The

first term in (4.1b) linearizes to

$$\frac{1}{2} \frac{L_s}{x_s} (\partial_\chi \phi)^2 = \frac{1}{2} \frac{1}{1 + \tilde{x}_s/L_s} (\partial_\chi \phi)^2 \approx \frac{1}{2} \left(1 - \frac{\tilde{x}_s}{L_s}\right) (\partial_\chi \phi)^2 \approx \frac{1}{2} (\partial_\chi \phi)^2. \quad (4.6)$$

The second term in (4.1b) linearizes to

$$\begin{aligned} & \frac{1}{2} \frac{x_s}{L_s} \left(-\frac{\chi}{x_s} \partial_y x_s \partial_\chi \phi + \partial_y \phi\right)^2 = \\ & = \frac{1}{2} \left(\frac{\chi^2}{L_s x_s} (\partial_y \tilde{x}_s)^2 (\partial_\chi \phi)^2 + \frac{x_s}{L_s} (\partial_y \phi)^2 - 2 \frac{\chi}{L_s} \partial_y \tilde{x}_s \partial_z \phi \partial_y \phi \right) \\ & \approx \frac{1}{2} \frac{\chi^2}{L_s^2} (\partial_y \tilde{x}_s)^2 (\partial_z \phi)^2 + \frac{1}{2} (\partial_y \phi)^2 - \frac{\chi}{L_s} \partial_y \tilde{x}_s \partial_z \phi \partial_y \phi \approx \frac{1}{2} (\partial_y \phi)^2, \end{aligned} \quad (4.7)$$

upon dropping the higher-order terms; a similar linearization occurs for the first term in (4.1c). The second term in (4.1c) linearizes to

$$\int_0^{L_s} \int_0^{L_y} \int_0^{H_0+\eta} \rho g (z - H_0) \left(1 + \frac{\tilde{x}_s}{L_s}\right) dz dy d\chi \quad (4.8a)$$

$$= \int_0^{L_s} \int_0^{L_y} \frac{1}{2} \rho g \eta^2 dy d\chi - \frac{1}{2} \rho g L_s L_y H_0^2 + \int_0^{L_s} \int_0^{L_y} \int_0^{H_0+\eta} \rho g (z - H_0) \frac{\tilde{x}_s}{L_s} dz dy d\chi \quad (4.8b)$$

$$\approx \int_0^{L_s} \int_0^{L_y} \frac{1}{2} \rho g \eta^2 dy d\chi - \frac{1}{2} \rho g L_s L_y H_0^2 + \int_0^{L_y} \int_0^{H_0} \rho g (z - H_0) \tilde{x}_s dz dy, \quad (4.8c)$$

in which third- and higher-order terms have been omitted. The second term in (4.8c) is a constant and can be dropped, as its variation vanishes. The $-\rho g (z - H_0) \tilde{x}_s$ term in (4.8c) represents the hydrostatic pressure. Since the dynamics of the mutual fluid-structure interaction are of interest, the linearization is assumed to occur around an equilibrium state and hence the hydrostatic term is omitted hereafter. In a similar way, the gravity force term $\rho_0 g Z$ in (4.1e) is omitted and the relations in §2.2 are used to simplify the beam expressions. The subtlety is neglected that, in the equilibrium (hydrostatic and lithostatic) state, all of λ , μ and ρ_0 vary slightly along the structure; they are all assumed to be constant.

Finally, the Lagrange multiplier γ term (4.1d) is linearized by observing that $x_s - X =$

$L_s + \tilde{x}_s - L_s - \tilde{X} = \tilde{x}_s - \tilde{X}$ and

$$\begin{aligned} & \tilde{x}_s(y = Y(L_s, b, c, t), z = Z(L_s, b, c, t), t) \\ &= \tilde{x}_s(y = b + \tilde{Y}(L_s, b, c, t), z = c + \tilde{Z}(L_s, b, c, t), t) \\ &= \tilde{x}_s(b, c, t) + (\tilde{Y}, \tilde{Z}) \cdot \frac{\partial \tilde{x}_s}{\partial (y, z)} \Big|_{y=b, z=c} + \dots \end{aligned} \quad (4.9)$$

In the manipulations in (4.9) \tilde{X} was Taylor-expanded at the interface around the equilibrium position. Here, \tilde{X} is multiplied by γ , which, on the other hand, is expanded around zero since $\gamma = 0$ at equilibrium when the hydrostatic pressure is neglected. Therefore, retaining only quadratic terms, the γ term (4.1d) becomes

$$\int_0^{L_y} \int_0^{L_z} \rho \gamma \left(x_s(Y(L_s, b, c, t), Z(L_s, b, c, t), t) - X(L_s, b, c, t) \right) dc db \quad (4.10a)$$

$$\approx \int_0^{L_y} \int_0^{L_z} \rho \gamma \left(\tilde{x}_s(b, c, t) - \tilde{X}(L_s, b, c, t) \right) dc db \quad (4.10b)$$

$$\approx \int_0^{L_y} \int_0^{H_0} \rho \gamma \left(\tilde{x}_s(y, z, t) - \tilde{X}(L_s, y, z, t) \right) dz dy. \quad (4.10c)$$

In (4.10c) the transformation from Lagrangian to Eulerian coordinates was performed in the linear approximation, as in section 2.2, and the integration in z was limited to the water height at the structural interface. Higher-order terms arising from the integration from H_0 to $H_0 + \eta$ have been neglected. For simplicity of notation, χ is renamed as x to yield, after incorporating all assumptions, the linearized VP

$$0 = \delta \int_0^T \int_0^{L_s} \int_0^{L_y} \rho \partial_t \eta \phi_f - \frac{1}{2} \rho g \eta^2 - \int_0^{H_0} \frac{1}{2} \rho |\nabla \phi|^2 dz dy dx \quad (4.11a)$$

$$+ \int_0^{L_y} \int_0^{H_0} \rho \partial_t \tilde{x}_s \phi_s + \rho \gamma \left(\tilde{x}_s(y, z, t) - \tilde{X}(L_s, y, z, t) \right) dz dy \quad (4.11b)$$

$$+ \int_{L_s}^{L_x} \int_0^{L_y} \int_0^{L_z} \rho_0 \partial_t \tilde{\mathbf{X}} \cdot \mathbf{U} - \frac{1}{2} \rho_0 |\mathbf{U}|^2 - \frac{1}{2} \lambda e_{ii} e_{jj} - \mu e_{ij}^2 dz dy dx dt. \quad (4.11c)$$

Due to the linearization, the domain is fixed and the full system is formulated in Eulerian coordinates. After using the temporal endpoint conditions $\delta \tilde{\mathbf{X}}(\mathbf{x}, 0) = \delta \tilde{\mathbf{X}}(\mathbf{x}, T) = 0$ and

$\delta\eta(x, y, 0) = \delta\eta(x, y, T) = 0$, the variation in (4.11) yields

$$\delta\gamma : \tilde{x}_s(y, z, t) = \tilde{X}(L_s, y, z, t) \quad \text{at } x = L_s \quad (4.12a)$$

$$\delta\tilde{x}_s : \gamma = \partial_t\phi_s \quad \text{at } x = L_s \quad (4.12b)$$

$$\delta\phi_s : \partial_t\tilde{x}_s = \partial_x\phi \quad \text{at } x = L_s \quad (4.12c)$$

$$\delta\tilde{X}_j(L_s, y, z, t) : -\delta_{1j}\rho\gamma = T_{1j} \quad \text{at } x = L_s \quad (4.12d)$$

$$\delta\phi_f : \partial_t\eta = \partial_z\phi \quad \text{at } z = H_0 \quad (4.12e)$$

$$\delta\eta : \partial_t\phi_f = -g\eta \quad \text{at } z = H_0 \quad (4.12f)$$

$$\delta\phi : \nabla^2\phi = 0 \quad \text{in } \Omega \quad (4.12g)$$

$$\delta\mathbf{U} : \partial_t\tilde{\mathbf{X}} = \mathbf{U} \quad \text{in } \Omega_0 \quad (4.12h)$$

$$\delta\tilde{X}_j : \rho_0\partial_t\mathbf{U}_j = \nabla_k T_{jk} \quad \text{in } \Omega_0 \quad (4.12i)$$

with $\Omega_0 : x \in [L_s, L_x], y \in [0, L_y], z \in [0, L_z]$, $\Omega : \chi \in [0, L_s], y \in [0, L_y], z \in [0, H_0]$ and linear stress tensor $T_{ij} = \lambda\delta_{ij}e_{kk} + 2\mu e_{ij}$. The Lagrange multiplier γ can be easily removed from equations (4.12). Without γ and by replacing $\tilde{x}_s(y, z, t)$ with $\tilde{X}_s = \tilde{X}(L_s, y, z, t)$, (4.12) becomes

$$\delta\phi_s : \partial_t\tilde{X}_s = \partial_x\phi \quad \text{at } x = L_s \quad (4.13a)$$

$$\delta\tilde{X}_j(L_s, y, z, t) : -\delta_{1j}\rho\partial_t\phi_s = T_{1j} \quad \text{at } x = L_s \quad (4.13b)$$

$$\delta\phi_f : \partial_t\eta = \partial_z\phi \quad \text{at } z = H_0 \quad (4.13c)$$

$$\delta\eta : \partial_t\phi_f = -g\eta \quad \text{at } z = H_0 \quad (4.13d)$$

$$\delta\phi : \nabla^2\phi = 0 \quad \text{in } \Omega \quad (4.13e)$$

$$\delta\mathbf{U} : \partial_t\tilde{\mathbf{X}} = \mathbf{U} \quad \text{in } \Omega_0 \quad (4.13f)$$

$$\delta\tilde{X}_j : \rho_0\partial_t\mathbf{U}_j = \nabla_k T_{jk} \quad \text{in } \Omega_0. \quad (4.13g)$$

System (4.13) can be also obtained if the removal of the Lagrange multiplier γ is

performed at the level of VP. Then (4.11) takes the form

$$0 = \delta \int_0^T \int_0^{L_s} \int_0^{L_y} \rho \partial_t \eta \phi_f - \frac{1}{2} \rho g \eta^2 - \int_0^{H_0} \frac{1}{2} \rho |\nabla \phi|^2 dz dy dx \quad (4.14a)$$

$$+ \int_0^{L_y} \int_0^{H_0} \rho \partial_t \tilde{X}_s \phi_s dz dy \quad (4.14b)$$

$$+ \int_{L_s}^{L_x} \int_0^{L_y} \int_0^{L_z} \rho_0 \partial_t \tilde{\mathbf{X}} \cdot \mathbf{U} - \frac{1}{2} \rho_0 |\mathbf{U}|^2 - \frac{1}{2} \lambda e_{ii} e_{jj} - \mu e_{ij}^2 dz dy dx dt. \quad (4.14c)$$

The coupling term (4.14b), derived here, is equivalent to the *ad hoc* one proposed in Salwa et al. (2016b).

To further simplify computations, non-dimensional variables are now introduced. A length scale D is chosen, e.g., beam length, whereafter other units are nondimensionalized using

$$V = \sqrt{gD}, \quad T = \frac{D}{V}, \quad M = \rho D^3. \quad (4.15)$$

Then, coordinates and variables are transformed to non-dimensional ones using

$$\begin{aligned} x &\rightarrow Dx & y &\rightarrow Dy & z &\rightarrow Dz & \eta &\rightarrow D\eta \\ \rho &\rightarrow \frac{M}{D^3} \rho & \rho_0 &\rightarrow \frac{M}{D^3} \rho_0 & \phi &\rightarrow VD\phi \\ \mathbf{X} &\rightarrow D\mathbf{X} & \lambda &\rightarrow \frac{M}{DT^2} \lambda & \mu &\rightarrow \frac{M}{DT^2} \mu. \end{aligned} \quad (4.16)$$

Using (4.16) enables transformation of the whole Lagrangian to the non-dimensional one $\mathcal{L} \rightarrow MV^2 \mathcal{L}$, whence the final simplified Lagrangian from the VP (4.14) becomes

$$\begin{aligned} \mathcal{L} &= \int_0^{L_s} \int_0^{L_y} \left[\partial_t \eta \phi_f - \frac{1}{2} \eta^2 - \int_0^{H_0} \frac{1}{2} |\nabla \phi|^2 dz \right] dy dx \\ &+ \int_0^{L_y} \int_0^{H_0} \partial_t X_s \phi_s dz dy \\ &+ \int_{L_s}^{L_x} \int_0^{L_y} \int_0^{L_z} \rho_0 \partial_t \mathbf{X} \cdot \mathbf{U} - \frac{1}{2} \rho_0 |\mathbf{U}|^2 - \frac{1}{2} \lambda e_{ii} e_{jj} - \mu e_{ij}^2 dz dy dx \end{aligned} \quad (4.17)$$

with, it is recalled, $e_{ij} = \frac{1}{2}(\partial_i X_j + \partial_j X_i)$. Hereafter, although the tilde over the X has been dropped for simplicity of notation, it still denotes the displacement rather than the actual beam position.

4.3 Solution of the coupled linear system

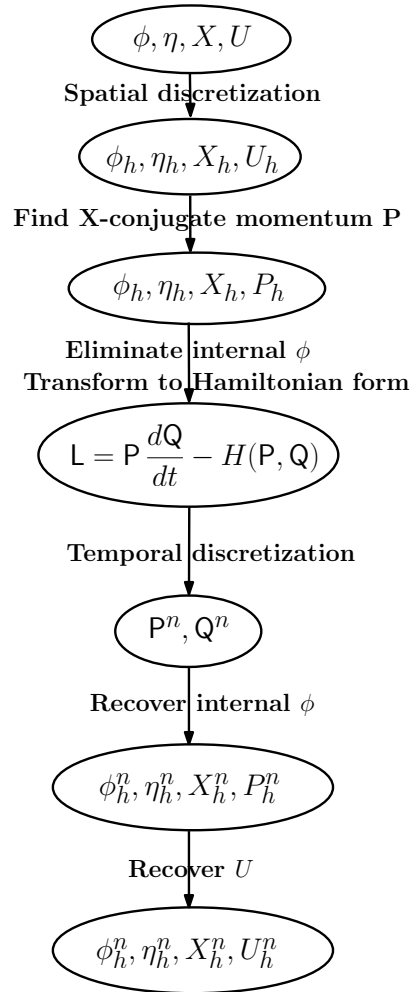


Figure 4.1: Flow chart schematically depicting the solution method. The subscript $(\cdot)_h$ denotes a spatially discretized function and superscript $(\cdot)^n$ the timestep counter.

In Fig. 4.1, is portrayed the discretization procedure of the VP with Lagrangian (4.17). The system is reduced to Hamiltonian form, in which a known stable time discretization

scheme can be applied. Though ultimately a space-time discrete system of equations is sought, it is much easier to work with the space-discretized system than with the continuous one, as it invites the use of matrix inverses and partial rather than functional derivatives. Therefore, spatial discretization is first undertaken by using continuous C^0 -Galerkin finite element expansions directly substituted into the VP. Since the variable \mathbf{X} is conjugated through coupling to both \mathbf{U} and ϕ , the first step is to find its single conjugate momentum \mathbf{P} . It transpires that the interior ϕ degrees of freedom are not independent, and can be expressed in terms of the free-surface ones ϕ_f and \mathbf{P} at the common boundary. The resulting system has a standard Hamiltonian structure with Lagrangian $L = \mathbf{P} d\mathbf{Q}/dt - H(\mathbf{P}, \mathbf{Q}, t)$, where $\mathbf{Q} = \mathbf{Q}(t)$ and $\mathbf{P} = \mathbf{P}(t)$ are the conjugate vectors of unknowns, see Fig. 4.1. For such a system, stable, second-order, conservative temporal schemes such as the Störmer-Verlet method are known. One is thus left with a fully discretized VP and the resulting algebraic equations of motion follow. To avoid computing full-system matrix inverses, ϕ is reintroduced in the interior, together with \mathbf{U} instead of \mathbf{P} at properly determined time levels. Details are provided next.

4.3.1 FEM space discretization

To find a spatial discretization, C^0 -Galerkin finite element expansions of the variables are, given an appropriate mesh tessellation of the fixed fluid and beam domains, substituted directly into the VP. The basis functions are $\tilde{\varphi}_i(x, y, z)$ in the fluid domain with the limiting basis function $\tilde{\varphi}_\alpha(x, y) = \tilde{\varphi}_\alpha(x, y, z = H_0)$ at the free surface $z = H_0$, and $\tilde{X}_k(x, y, z)$ in the structural domain. Both the fixed fluid and beam domains have coordinates $\vec{x} = (x, y, z) = (x_1, x_2, x_3)$. At the common interface $x = L_s$ (see Fig. 3.2), it is assumed that the respective meshes join up with common nodes. However, since there are two meshes, these nodes are denoted by indices m and n on the fluid mesh and by \tilde{m} and \tilde{n} on the solid mesh. There is a mapping between these two node sets, namely $m = m(\tilde{m})$. Here, i and j denote nodes in the fluid domain, α and β nodes at its surface, m and n or \tilde{m} and \tilde{n} nodes at the common fluid-structure boundary, and k and l

nodes in the structure domain. Primed indices refer to the nodes below the water surface, and α_n denotes the surface nodes at the common boundary. Indices $a, b = 1, 2, 3$ are the coordinate indices used for \mathbf{X} and \mathbf{x} . The Einstein summation convention is assumed for all indices. Finally, with the subscript h denoting the numerical approximations, the expansions are

$$\begin{aligned} \phi_h(\vec{x}, t) &= \phi_i(t)\tilde{\varphi}_i(\vec{x}) & \phi_{fh}(x, y, t) &= \phi_\alpha(t)\tilde{\varphi}_\alpha(x, y) & \eta_h(x, y, t) &= \eta_\alpha(t)\tilde{\varphi}_\alpha(x, y) \\ X_h^a(\vec{x}, t) &= X_k^a(t)\tilde{X}_k(\vec{x}) & U_h^a(\vec{x}, t) &= U_k^a(t)\tilde{X}_k(\vec{x}). \end{aligned} \quad (4.18)$$

Substitution of (4.18) into (4.17) yields the spatially discrete Lagrangian function

$$L = \dot{\eta}_\alpha M_{\alpha\beta} \phi_\beta + \dot{X}_k^a N_{kl} U_l^a + \dot{X}_{\tilde{m}}^1 W_{\tilde{m}n} \phi_n - H(\eta, \phi, X, U), \quad (4.19)$$

with Hamiltonian

$$H(\eta, \phi, X, U) = \frac{1}{2} \eta_\alpha M_{\alpha\beta} \eta_\beta + \frac{1}{2} \phi_i A_{ij} \phi_j + \frac{1}{2} U_k^a N_{kl} U_l^a + \frac{1}{2} X_k^a E_{kl}^{ab} X_l^b, \quad (4.20)$$

wherein a superscript dot indicates a time derivative, and in which the matrices are given by

$$\begin{aligned} M_{\alpha\beta} &= \int_x \int_y \tilde{\varphi}_\alpha \tilde{\varphi}_\beta \, dy \, dx, & A_{ij} &= \int_\Omega \nabla \tilde{\varphi}_i \cdot \nabla \tilde{\varphi}_j \, dV, \\ W_{\tilde{m}n} &= \int_y \int_0^{H_0} \tilde{X}_{\tilde{m}} \tilde{\varphi}_n \, dz \, dy, & N_{kl} &= \rho_0 \int_{\Omega_0} \tilde{X}_k \tilde{X}_l \, dV, \\ B_{kl}^{ab} &= \int_{\Omega_0} \frac{\partial \tilde{X}_k}{\partial x_a} \frac{\partial \tilde{X}_l}{\partial x_b} \, dV, & E_{kl}^{ab} &= \lambda B_{kl}^{ab} + \mu (B_{kl}^{cc} \delta_{ab} + B_{kl}^{ba}). \end{aligned} \quad (4.21)$$

Provided that in both fluid and beam domains the basis functions come from the same function space, one can identify $\tilde{X}_{\tilde{m}} \equiv \tilde{\phi}_{m(\tilde{m})}$. In other words, if the numbering is taken into account, at the fluid-beam interface basis functions are the same in the fluid and the

beam. The matrices in (4.21) are symmetric; in particular, it is highlighted that

$$B_{kl}^{ab} = B_{lk}^{ba} \quad \text{and} \quad E_{kl}^{ab} = E_{lk}^{ba}. \quad (4.22)$$

Unlike in the continuous case, *cf.* remarks after (2.1), the Dirichlet boundary condition can be incorporated directly into the Lagrangian, *i.e.*, by imposing $X_{k_b}^a = 0$ and $U_{k_b}^a = 0$, with $(\cdot)_{k_b}$ denoting the structure-base nodes. Then (4.19) becomes

$$\begin{aligned} L &= \dot{\eta}_\alpha M_{\alpha\beta} \phi_\beta + \dot{X}_{k'}^a N_{k'l'} U_{l'}^a + \dot{X}_{\tilde{m}'}^1 W_{\tilde{m}'n} \phi_n - H(\eta, \phi, X, U), \\ H(\eta, \phi, X, U) &= \frac{1}{2} \eta_\alpha M_{\alpha\beta} \eta_\beta + \frac{1}{2} \phi_i A_{ij} \phi_j + \frac{1}{2} U_{k'}^a N_{k'l'} U_{l'}^a + \frac{1}{2} X_{k'}^a E_{k'l'}^{ab} X_{l'}^b, \end{aligned} \quad (4.23)$$

with primed structural indices denoting nodes excluding those at the beam bottom. The next step is to compute the momentum conjugate to $X_{k'}^a$,

$$R_{k'}^a = \frac{\partial L}{\partial \dot{X}_{k'}^a} = N_{k'l'} U_{l'}^a + \delta_{a1} \delta_{k'\tilde{m}'} W_{\tilde{m}'n} \phi_n, \quad (4.24)$$

in which δ_{ij} is the Kronecker delta symbol. Rearrangement of (4.24) yields

$$U_{k'}^a = N_{k'l'}^{-1} R_{l'}^a - \delta_{a1} N_{k'l'}^{-1} \delta_{l'\tilde{m}'} W_{\tilde{m}'n} \phi_n, \quad (4.25)$$

in which it is to be noted that $N_{k'l'}^{-1}$ is the inverse not of the full matrix N_{kl} , but of the system excluding the nodes at the beam bottom. Therefore, after using $R_{k'}^a$ instead of $U_{k'}^a$, the Lagrangian takes the form

$$L = \dot{\eta}_\alpha M_{\alpha\beta} \phi_\beta + \dot{X}_{k'}^a R_{k'}^a - H(\phi_\alpha, \eta_\alpha, X_{k'}^a, R_{k'}^a), \quad (4.26)$$

in which the Hamiltonian (computed using the Lagrangian L in (4.19) and (4.25)) is given by

$$\begin{aligned}
 H(\phi_\alpha, \eta_\alpha, X_{k'}^a, R_{k'}^a) &= \dot{\eta}_\alpha M_{\alpha\beta} \phi_\beta + \dot{X}_{k'}^a R_{k'}^a - L \\
 &= \frac{1}{2} \eta_\alpha M_{\alpha\beta} \eta_\beta + \frac{1}{2} \phi_i A_{ij} \phi_j + \frac{1}{2} \phi_m \widetilde{M}_{mn} \phi_n \\
 &\quad - R_{k'}^1 N_{k'l'}^{-1} \delta_{l'\tilde{m}'} W_{\tilde{m}'n} \phi_n \\
 &\quad + \frac{1}{2} R_{k'}^a N_{k'l'}^{-1} R_{l'}^a + \frac{1}{2} X_{k'}^a E_{k'l'}^{ab} X_{l'}^b,
 \end{aligned} \tag{4.27}$$

in which

$$\widetilde{M}_{mn} = (N^{-1})_{\tilde{m}'\tilde{n}'} W_{\tilde{m}'m} W_{\tilde{n}'n}. \tag{4.28}$$

To facilitate the computations, the vector P is introduced and defined by

$$R_{k'}^a = N_{k'l'} P_{l'}^a, \tag{4.29}$$

which obviates the need to compute the inverse of the full matrix N , instead requiring only the part in the definition of \widetilde{M}_{mn} . The inverse $(N^{-1})_{\tilde{m}'\tilde{n}'}$ in (4.28) is the submatrix of the inverse of $N_{k'l'}$ including interface but excluding beam-bottom nodes. Therefore, the substitution of (4.29) into (4.26) using (4.27) yields

$$L = \dot{\eta}_\alpha M_{\alpha\beta} \phi_\beta + \dot{X}_{k'}^a N_{k'l'} P_{l'}^a - H(\phi_\alpha, \eta_\alpha, X_{k'}^a, P_{k'}^a), \tag{4.30}$$

with the Hamiltonian

$$\begin{aligned}
 H(\phi_\alpha, \eta_\alpha, X_{k'}^a, P_{k'}^a) &= \frac{1}{2} \eta_\alpha M_{\alpha\beta} \eta_\beta + \frac{1}{2} \phi_i A_{ij} \phi_j + \frac{1}{2} \phi_m \widetilde{M}_{mn} \phi_n \\
 &\quad - P_{\tilde{m}'}^1 W_{\tilde{m}'n} \phi_n + \frac{1}{2} P_{k'}^a N_{k'l'} P_{l'}^a + \frac{1}{2} X_{k'}^a E_{k'l'}^{ab} X_{l'}^b.
 \end{aligned} \tag{4.31}$$

That not all terms in (4.31) are positive definite will be discussed in more detail later. Note that the Hamiltonian depends explicitly on only the surface degrees of freedom ϕ_α . Therefore, it is possible to eliminate the interior degrees of freedom $\phi_{i'}$, with the primed index i' denoting the nodes in the interior of the fluid excluding those on the free surface,

in order to reduce the system to the general Hamiltonian form. Therefore, the equations of motion are derived by applying the VP to the Lagrangian (4.30); after rearranging and using arbitrariness of respective variations as well as suitable end-point conditions, there follows

$$\begin{aligned}
 0 &= \int_0^{t_1} L dt \\
 &= \int_0^{t_1} \left\{ \dot{\eta}_\alpha M_{\alpha\beta} \delta\phi_\beta - M_{\alpha\beta} \dot{\phi}_\beta \delta\eta_\alpha - \eta_\alpha M_{\alpha\beta} \delta\eta_\beta - \phi_i A_{ij} \delta\phi_j - \phi_m \widetilde{M}_{mn} \delta\phi_n \right. \\
 &\quad + (W_{\widetilde{m}'n} \phi_n \delta P_{\widetilde{m}'}^1 + P_{\widetilde{m}'}^1 W_{\widetilde{m}'n} \delta\phi_n) \\
 &\quad \left. + \left(\dot{X}_{k'}^a N_{k'l'} \delta P_{l'}^a - N_{k'l'} \dot{P}_{l'}^a \delta X_{k'}^a - P_{k'}^a N_{k'l'} \delta P_{l'}^a \right) - X_{k'}^a E_{k'l'}^{ab} \delta X_{l'}^b \right\} dt.
 \end{aligned} \tag{4.32}$$

Hence, by renaming certain indices, the following equations are obtained

$$\delta\eta_\beta : \quad \dot{\phi}_\alpha = -\eta_\alpha \tag{4.33a}$$

$$\delta\phi_\alpha : \quad M_{\alpha\beta} \dot{\eta}_\beta = \phi_i A_{i\alpha} + \underbrace{(\phi_m \widetilde{M}_{mn} - P_{\widetilde{m}'}^1 W_{\widetilde{m}'n})}_{\delta_{\alpha n}} \tag{4.33b}$$

$$\delta\phi_{j'} : \quad \phi_i A_{ij'} = \underbrace{(-\phi_m \widetilde{M}_{mn} + P_{\widetilde{m}'}^1 W_{\widetilde{m}'n})}_{\delta_{nj'}} \tag{4.33c}$$

$$\delta P_{k'}^a : \quad N_{k'l'} \dot{X}_{l'}^a = N_{k'l'} P_{l'}^a - \underbrace{\delta_{\alpha 1} \delta_{k'l'} \widetilde{m}' W_{\widetilde{m}'n} \phi_n}_{\delta_{\alpha 1} \delta_{k'l'} \widetilde{m}' W_{\widetilde{m}'n} \phi_n} \tag{4.33d}$$

$$\delta X_{k'}^a : \quad N_{k'l'} \dot{P}_{l'}^a = -E_{k'l'}^{ab} X_{l'}^b, \tag{4.33e}$$

in which the new coupling terms introduced by the present formulation are underlined.

Defining the matrix C by

$$C_{i'j'} = A_{i'j'} + \delta_{i'm} \widetilde{M}_{mn} \delta_{nj'}, \tag{4.34}$$

(4.33c) can be split into internal and surface degrees of freedom and inverted to express internal ones in terms of surface ones and P at the interface

$$\phi_{i'} = C_{i'j'}^{-1} \left(-\phi_\alpha A_{\alpha j'} + P_{\widetilde{m}'}^1 W_{\widetilde{m}'n} \delta_{nj'} - \phi_\alpha \delta_{\alpha m} \widetilde{M}_{mn} \delta_{nj'} \right). \tag{4.35}$$

The interior degrees of freedom are removed from the Lagrangian by substituting (4.35) into (4.26) to obtain

$$\begin{aligned}
 L = & \dot{\eta}_\alpha M_{\alpha\beta} \phi_\beta - \frac{1}{2} \eta_\alpha M_{\alpha\beta} \eta_\beta - \frac{1}{2} \phi_\alpha D_{\alpha\beta} \phi_\beta \\
 & + P_{k'}^a G_{k'\alpha}^a \phi_\alpha \\
 & + P_{k'}^a N_{k'l'} \dot{X}_{l'}^a - \frac{1}{2} P_{k'}^a F_{k'l'}^{ab} P_{l'}^b - \frac{1}{2} X_{k'}^a E_{k'l'}^{ab} X_{l'}^b,
 \end{aligned} \tag{4.36}$$

where Schur decomposition matrices D , F and G have been introduced; their explicit forms are omitted. The structure of (4.36) is as follows: the first line describes the fluid, the second the coupling, and the third the beam. In a more visual matrix notation, (4.36) has the structure

$$\begin{aligned}
 L = & (\dot{\eta}, \dot{\vec{X}}) \begin{pmatrix} M & \phi \\ N & \vec{P} \end{pmatrix} - \frac{1}{2} (\eta, \vec{X}) \begin{pmatrix} M & 0 \\ 0 & E \end{pmatrix} \begin{pmatrix} \eta \\ \vec{X} \end{pmatrix} \\
 & - \frac{1}{2} (\phi, \vec{P}) \begin{pmatrix} D & -G^T \\ -G & F \end{pmatrix} \begin{pmatrix} \phi \\ \vec{P} \end{pmatrix}.
 \end{aligned} \tag{4.37}$$

The classical Hamilton's equations of an abstract system emerge when a generalized coordinate vector and its conjugate vector are introduced, *i.e.*

$$\begin{aligned}
 \mathbf{Q} = & (\eta_1, \dots, \eta_{N_f}, X_1^1, \dots, X_{N_b}^1, X_1^2, \dots, X_{N_b}^2, X_1^3, \dots, X_{N_b}^3) \\
 \mathbf{P} = & (M_{1\alpha} \phi_\alpha, \dots, M_{N_f\alpha} \phi_\alpha, N_{1k'} P_{k'}^1, \dots, N_{N_b k'} P_{k'}^1, \\
 & N_{1k'} P_{k'}^2, \dots, N_{N_b k'} P_{k'}^2, N_{1k'} P_{k'}^3, \dots, N_{N_b k'} P_{k'}^3),
 \end{aligned} \tag{4.38}$$

with N_f degrees of freedom at the free surface and N_b degrees of freedom in the beam (recall, fixed-bottom nodes are excluded), using which the Lagrangian can be written in the form

$$\mathbf{L} = \frac{d\mathbf{Q}}{dt} \cdot \mathbf{P} - \mathbf{H}(\mathbf{Q}, \mathbf{P}) \tag{4.39}$$

with Hamiltonian $H(P, Q)$. After introducing the following (symmetric) matrices

$$\begin{aligned} M_Q &= \begin{pmatrix} M & 0 \\ 0 & E \end{pmatrix} \\ M_P &= \begin{pmatrix} M^{-1}DM^{-1} & -M^{-1}G^T N^{-1} \\ -N^{-1}GM^{-1} & N^{-1}FN^{-1} \end{pmatrix}, \end{aligned} \quad (4.40)$$

the Hamiltonian in (4.39) can be written as

$$H(Q, P) = \frac{1}{2}Q^T M_Q Q + \frac{1}{2}P^T M_P P. \quad (4.41)$$

4.3.2 Time discretization

The Störmer-Verlet scheme (see Marsden and West (2001) for a definition, and Bokhove and Kalogirou (2016) for a variational derivation) is used to discretize (4.39) to second-order accuracy in time. The resulting difference equations are

$$\begin{aligned} P^{n+1/2} &= P^n - \frac{1}{2}\Delta t \frac{\partial H(Q^n, P^{n+1/2})}{\partial Q^n}, \\ Q^{n+1} &= Q^n + \frac{1}{2}\Delta t \left(\frac{\partial H(Q^n, P^{n+1/2})}{\partial P^{n+1/2}} + \frac{\partial H(Q^{n+1}, P^{n+1/2})}{\partial P^{n+1/2}} \right), \\ P^{n+1} &= P^{n+1/2} - \frac{1}{2}\Delta t \frac{\partial H(Q^{n+1}, P^{n+1/2})}{\partial Q^{n+1}}. \end{aligned} \quad (4.42)$$

In the linear case considered, for which the Hamiltonian is given by (4.41), (4.42) yields the explicit scheme

$$\begin{aligned} P^{n+1/2} &= P^n - \frac{1}{2}\Delta t M_Q Q^n, \\ Q^{n+1} &= Q^n + \Delta t M_P P^{n+1/2}, \\ P^{n+1} &= P^{n+1/2} - \frac{1}{2}\Delta t M_Q Q^{n+1}. \end{aligned} \quad (4.43)$$

After some manipulations (described in detail in Appendix B), in terms of original physical variables the discretization to be implemented is

$$\phi_\alpha^{n+1/2} = \phi_\alpha^n - \frac{1}{2}\Delta t \eta_\alpha^n \quad (4.44a)$$

$$\begin{aligned} N_{k'l'}(U_{l'}^a)^{n+1/2} + \underbrace{\delta_{a1}\delta_{k'\tilde{m}'}W_{\tilde{m}'n}\delta_{ni'}\phi_{i'}^{n+1/2}}_{\text{}} = N_{k'l'}(U_{l'}^a)^n - \frac{1}{2}\Delta t E_{k'l'}^{ab}(X_{l'}^b)^n \\ + \delta_{a1}\delta_{k'\tilde{m}'}W_{\tilde{m}'n}\phi_n^n - \delta_{a1}\delta_{k'\tilde{m}'}W_{\tilde{m}'n}\delta_{n\alpha}\phi_\alpha^{n+1/2} \end{aligned} \quad (4.44b)$$

$$A_{i'j'}\phi_{i'}^{n+1/2} - \underbrace{(U_{\tilde{m}'}^1)^{n+1/2}W_{\tilde{m}'n}\delta_{nj'}}_{\text{}} = -A_{\alpha j'}\phi_\alpha^{n+1/2} \quad (4.44c)$$

$$M_{\alpha\beta}\eta_\beta^{n+1} = M_{\alpha\beta}\eta_\beta^n + \Delta t A_{\alpha i}\phi_i^{n+1/2} - \underbrace{\Delta t (U_{\tilde{m}'}^1)^{n+1/2}W_{\tilde{m}'n}\delta_{n\alpha}}_{\text{}} \quad (4.44d)$$

$$(X_{k'}^a)^{n+1} = (X_{k'}^a)^n + \Delta t (U_{k'}^a)^{n+1/2} \quad (4.44e)$$

$$\phi_\alpha^{n+1} = \phi_\alpha^{n+1/2} - \frac{1}{2}\Delta t \eta_\alpha^{n+1} \quad (4.44f)$$

$$\begin{aligned} N_{k'l'}(U_{l'}^a)^{n+1} + \underbrace{\delta_{a1}\delta_{k'\tilde{m}'}W_{\tilde{m}'n}\delta_{ni'}\phi_{i'}^{n+1}}_{\text{}} = N_{k'l'}(U_{l'}^a)^{n+1/2} - \frac{1}{2}\Delta t E_{k'l'}^{ab}(X_{l'}^b)^{n+1} \\ + \delta_{a1}\delta_{k'\tilde{m}'}W_{\tilde{m}'n}\phi_n^{n+1/2} - \delta_{a1}\delta_{k'\tilde{m}'}W_{\tilde{m}'n}\delta_{n\alpha}\phi_\alpha^{n+1} \end{aligned} \quad (4.44g)$$

$$A_{i'j'}\phi_{i'}^{n+1} - \underbrace{(U_{\tilde{m}'}^1)^{n+1}W_{\tilde{m}'n}\delta_{nj'}}_{\text{}} = -A_{\alpha j'}\phi_\alpha^{n+1}. \quad (4.44h)$$

Let us remark that equations (4.44a), (4.44d), (4.44e) and (4.44f) can be solved in the separate fluid and structure domains, while (4.44b), (4.44c), (4.44g) and (4.44h) have to be solved in both domains simultaneously. Therefore, the scheme is a variant of the mixed partitioned-monolithic approach, see *e.g.*, Hübner et al. (2004).

The Firedrake environment (see start of section 4.4) used to obtain 3D results accepts equations in the weak form as an input. Therefore, the weak-form equivalent of (4.44), with more general structural geometry, is

$$\int v \phi^{n+1/2} dS_f = \int v (\phi^n - \frac{1}{2}\Delta t \eta^n) dS_f \quad (4.45a)$$

$$\begin{aligned} \int \rho_0 \mathbf{v} \cdot \mathbf{U}^{n+1/2} dV_S + \int \mathbf{n} \cdot \mathbf{v} \phi^{n+1/2} dS_s = \rho_0 \int \mathbf{v} \cdot \mathbf{U}^n dV_S \\ - \frac{1}{2}\Delta t \int (\lambda \nabla \cdot \mathbf{v} \nabla \cdot \mathbf{X}^n + \mu \partial_a X_b^n (\partial_a v_b + \partial_b v_a)) dV_S + \int \mathbf{n} \cdot \mathbf{v} \phi^n dS_s \end{aligned} \quad (4.45b)$$

$$\int \nabla v \cdot \nabla \phi^{n+1/2} dV_F - \int v \mathbf{n} \cdot \mathbf{U}^{n+1/2} dS_s = 0 \quad (4.45c)$$

$$\int v \eta^{n+1} dS_f = \int v \eta^n dS_f + \Delta t \int \nabla v \cdot \nabla \phi^{n+1/2} dV_F - \Delta t \int v \mathbf{n} \cdot \mathbf{U}^{n+1/2} dS_s \quad (4.45d)$$

$$\int \mathbf{v} \cdot \mathbf{X}^{n+1} dV_S = \int \mathbf{v} \cdot (\mathbf{X}^n + \Delta t \mathbf{U}^{n+1/2}) dV_S \quad (4.45e)$$

$$\int v \phi^{n+1} dS_f = \int v (\phi^{n+1/2} - \frac{1}{2} \Delta t \eta^{n+1}) dS_f \quad (4.45f)$$

$$\int \rho_0 \mathbf{v} \cdot \mathbf{U}^{n+1} dV_S + \int \mathbf{n} \cdot \mathbf{v} \phi^{n+1} dS_s = \rho_0 \int \mathbf{v} \cdot \mathbf{U}^{n+1/2} dV_S - \frac{1}{2} \Delta t \int (\lambda \nabla \cdot \mathbf{v} \nabla \cdot \mathbf{X}^{n+1} + \mu \partial_a X_b^{n+1} (\partial_a v_b + \partial_b v_a)) dV_S + \int \mathbf{n} \cdot \mathbf{v} \phi^{n+1/2} dS_s \quad (4.45g)$$

$$\int \nabla v \cdot \nabla \phi^{n+1} dV_F - \int v \mathbf{n} \cdot \mathbf{U}^{n+1} dS_s = 0, \quad (4.45h)$$

in which dS_f denotes integration over the free surface, dS_s the fluid-structure interface, dV_F the fluid domain, dV_S the structure domain, and \mathbf{n} is, as before, the unit outward-normal vector of the fluid domain. In general, the quantities on the left-hand side are unknowns. The procedure for solving equations (4.45) is summarised as follows. The result of (4.45a) is $\phi^{n+1/2}$ at the free surface. It is used as a Dirichlet boundary condition in (4.45b) and (4.45c), which are solved simultaneously to get $\phi^{n+1/2}$ in the whole fluid domain and $\mathbf{U}^{n+1/2}$. Next, η is updated in (4.45d) and \mathbf{X} in (4.45e). Then (4.45f) yields ϕ^{n+1} at the free surface. Again, it is used as a Dirichlet boundary condition in the simultaneously solved (4.45g) and (4.45h) for the final update of the full ϕ and \mathbf{U} . In addition, the beam-bottom no-motion boundary condition is applied, *i.e.*, $\mathbf{X}(0, y, z, t) = \mathbf{0}$ in (4.45e) and $\mathbf{U}(0, y, z, t) = \mathbf{0}$ in (4.45b), (4.45c), (4.45g) and (4.45h).

The numerical results obtained via the described approach are now presented and discussed.

4.4 Results

Firedrake (Rathgeber et al., 2016) is an open-source FEM automation package written in python, that uses PETSc for numerical computations. It accepts equations in weak form and automatically assembles the system matrices. Therefore, in this case the scheme in the form (4.45) was used, with linear continuous Galerkin test functions. For the purposes of illustration and validation, computations were performed first in two dimensions (no y -dependence), with bespoke code (no use of Firedrake for automation), constructing directly the matrices in (4.44). Later, the two-dimensional code in Firedrake was shown to produce the same results. Once the scheme was verified to yield a stable solution, computations in three dimensions using the Firedrake software were performed.

4.4.1 2D results

Parameter values used in this case are shown in Table 4.1. In order to render visible the beam deformations, Lamé constants are taken to be approximately 10^4 times smaller than those for the steel used to make wind-turbine masts. As previously mentioned, Dirichlet boundary conditions were assumed for the beam, which is fixed (zero displacement and velocity) at its base $z = 0$ whereas other boundaries can move freely. A solution with zero initial movement and displacement in the beam is presented, and, in the fluid, the first mode of an analytical solution, with deflected initial free surface and no fluid velocity, the natural period of which is $T = 5.3s$. The energy in the system is presented in Fig. 4.2, in which it is clear that, although there is always an energy exchange between the water and beam, the total energy remains bounded, due to the energy conservation of the space and time discretization. Oscillations in the energy depend on the timestep used, as shown in Fig. 4.3. As expected, the method is second-order accurate in time, *i.e.*, halving the timestep decreases the difference between the numerically computed energy and the exact one by a factor of four. The method is also expected to be second-order accurate in space, as linear basis functions are used in the finite element expansion. To verify this the

formula is used for the convergence rate derived for regularly refined-by-halving meshes from Aitken extrapolation

$$s = \log_2 \frac{\|\phi_f - \phi_m\|}{\|\phi_m - \phi_c\|}, \quad (4.46)$$

in which ϕ_c , ϕ_m and ϕ_f is the solution on coarse, medium and fine meshes, respectively, and $\|\cdot\|$ denotes either the L_2 or L_∞ norm. The convergence rate s computed by (4.46) is shown in Fig. 4.4, which shows an oscillatory behaviour around the value of $s = 1.7$. Snapshots of the initial condition (no flow, free surface deflected) and evolved state are shown in Fig. 4.5.

Table 4.1: Parameter values used in the 2D computations.

Parameter	Value	Comment
g	9.8 m/s ²	gravitational acceleration
$L_x \times H_0$	20 m \times 10 m	water domain
$L_x^B \times L_z^B$	2 m \times 20 m	beam domain
ρ	1000 kg/m ²	water density
ρ_0	7700 kg/m ²	beam density (steel)
λ	1×10^7 N/m	first Lamé constant
μ	1×10^7 N/m	second Lamé constant
$N_x^W \times N_z^W$	20 \times 10	no. of elements in water
$N_x^B \times N_z^B$	4 \times 20	no. of elements in beam

4.4.2 3D results

Parameter values for this case are shown in Table 4.2. The mesh consists of layers of tetrahedra in the z -direction, and the fluid domain is asymmetric in the xy plane. The beam is represented by a hollow cylinder, which is meshed with layers of 8 blocks comprising 4 tetrahedra each. Snapshots of the system evolution are shown in Fig. 4.8. The applied initial condition is one of a beam in equilibrium adjacent to a fluid whose free-surface elevation is the first mode of a harmonic analytical solution (without the beam) with oscillation period of 4s. Fig. 4.6 presents the energy transfer in the system. The convergence of the results with decreasing time step is shown in Fig. 4.7.

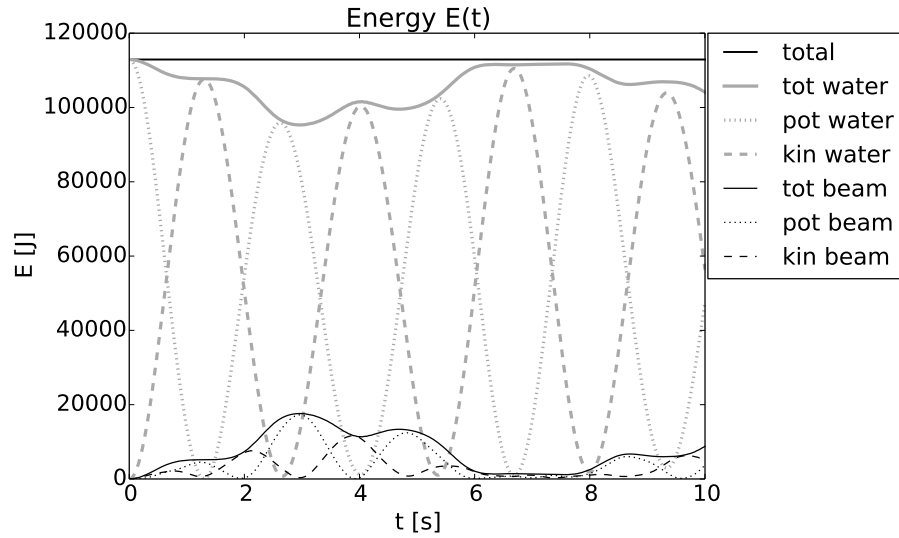


Figure 4.2: Energy apportionment (in J) in the 2D system. From top to bottom (see key), curves represent energies of the total system (medium, horizontal), total water (thick, wavy), potential/kinetic water (thick dotted/dashed oscillatory), total beam (thin, wavy) and potential/kinetic beam (thin dotted/dashed oscillatory).

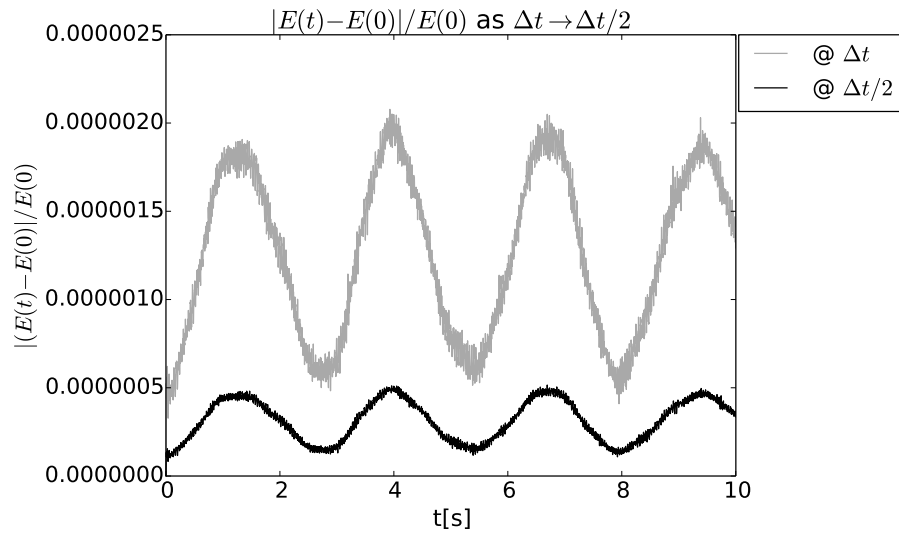


Figure 4.3: Convergence of the temporal energy as a function of timestep in 2D: relative error curves for timesteps Δt (upper curve) and $\Delta t/2$ (lower curve) have amplitudes in the ratio four to one, confirming second-order convergence.

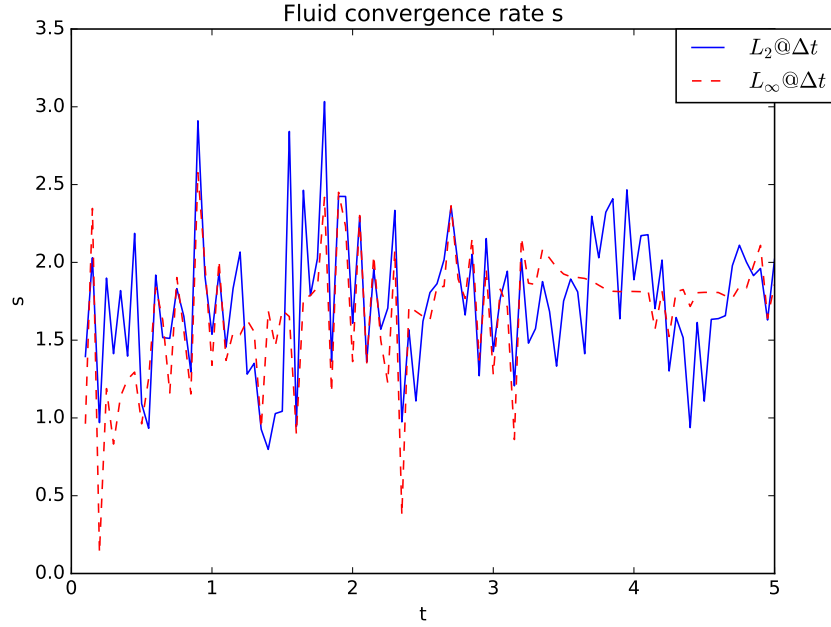


Figure 4.4: Rate of convergence, s in (4.46), of ϕ against time, computed using 3 regularly refined meshes and two norms: L_2 (solid line) and L_∞ (dashed line). As the mesh size tends to zero, the theoretical limit of Aitken acceleration yields $s = 2$.

Table 4.2: Parameter values used in the 3D computations.

Parameter	Value	Comment
g	9.8 m/s^2	gravitational acceleration
$L_x \times L_y \times H_0$	$10 \text{ m} \times 10 \text{ m} \times 4 \text{ m}$	water domain
R_i	0.6 m	beam inner radius
R_o	0.8 m	beam outer radius
H	12 m	beam height
ρ	1000 kg/m^3	water density
ρ_0	7700 kg/m^3	beam density (steel)
λ	$1 \times 10^7 \text{ N/m}^2$	first Lamé constant
μ	$1 \times 10^7 \text{ N/m}^2$	second Lamé constant
N_z^W	4	no. of layers in water
N_z^B	12	no. of layers in beam

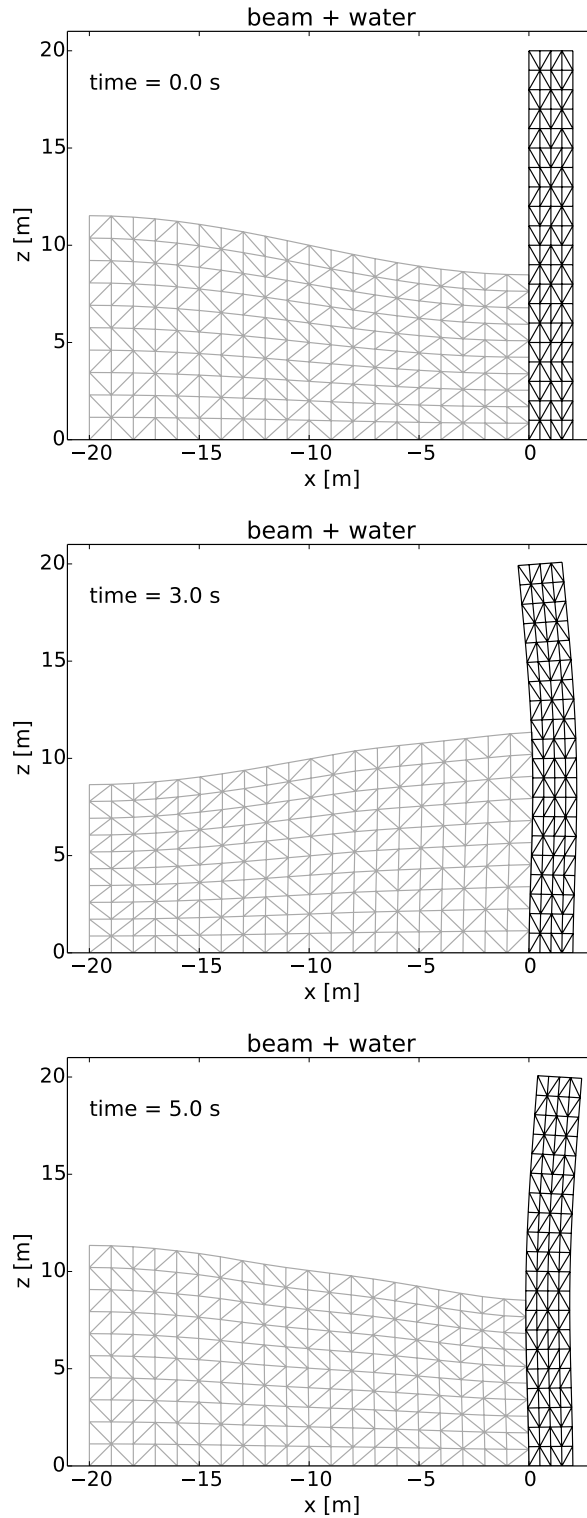


Figure 4.5: Temporal snapshots of the 2D water-beam geometry during flow evolution. Although the computational domain is fixed, results have been post-processed into physical space to visualize the deformations. Initial condition of no flow (top) with motion initiated by free-surface displacement. Solutions after 3s (middle) and 5s (bottom).

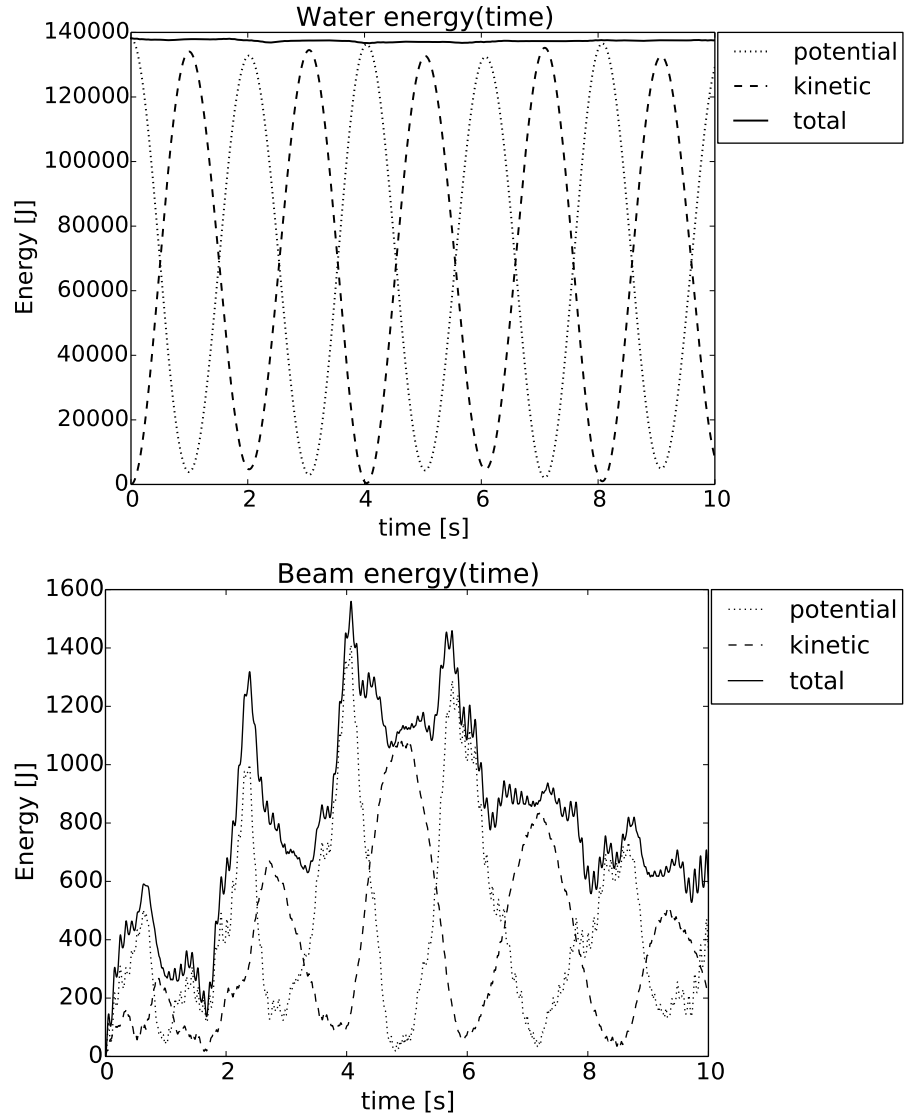


Figure 4.6: Energy apportionment (in J) in the 3D system: water (top) and beam (bottom). Curves represent total (continuous), potential (dotted) and kinetic (dashed) energies. Note from the disparate vertical scales in the two plots that the total beam energy is much less than that of the water.

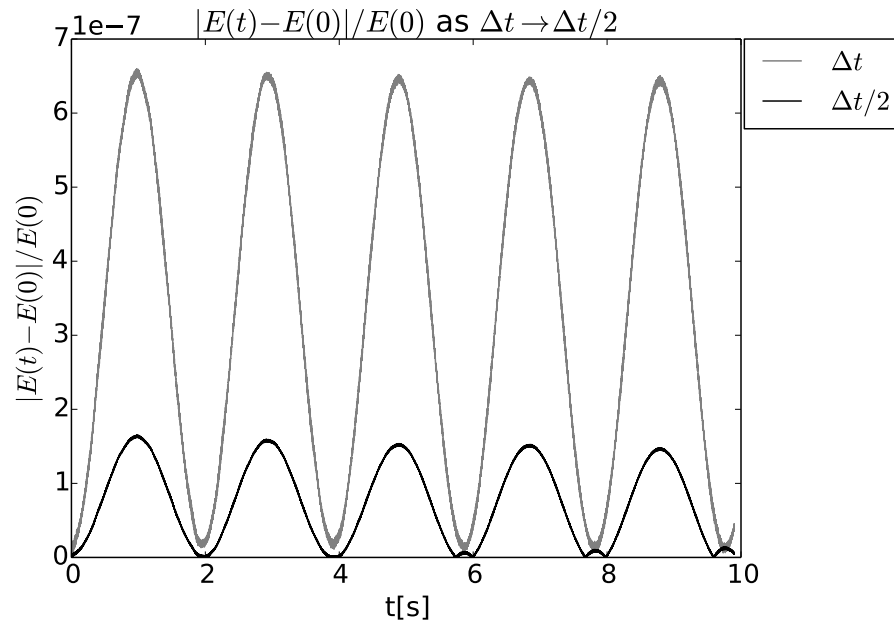


Figure 4.7: Convergence of the method as a function of the timestep in 3D: the full timestep (upper curve, grey) and half timestep (lower curve, black) relative-error curves have amplitudes in the ratio four to one, confirming second-order convergence.

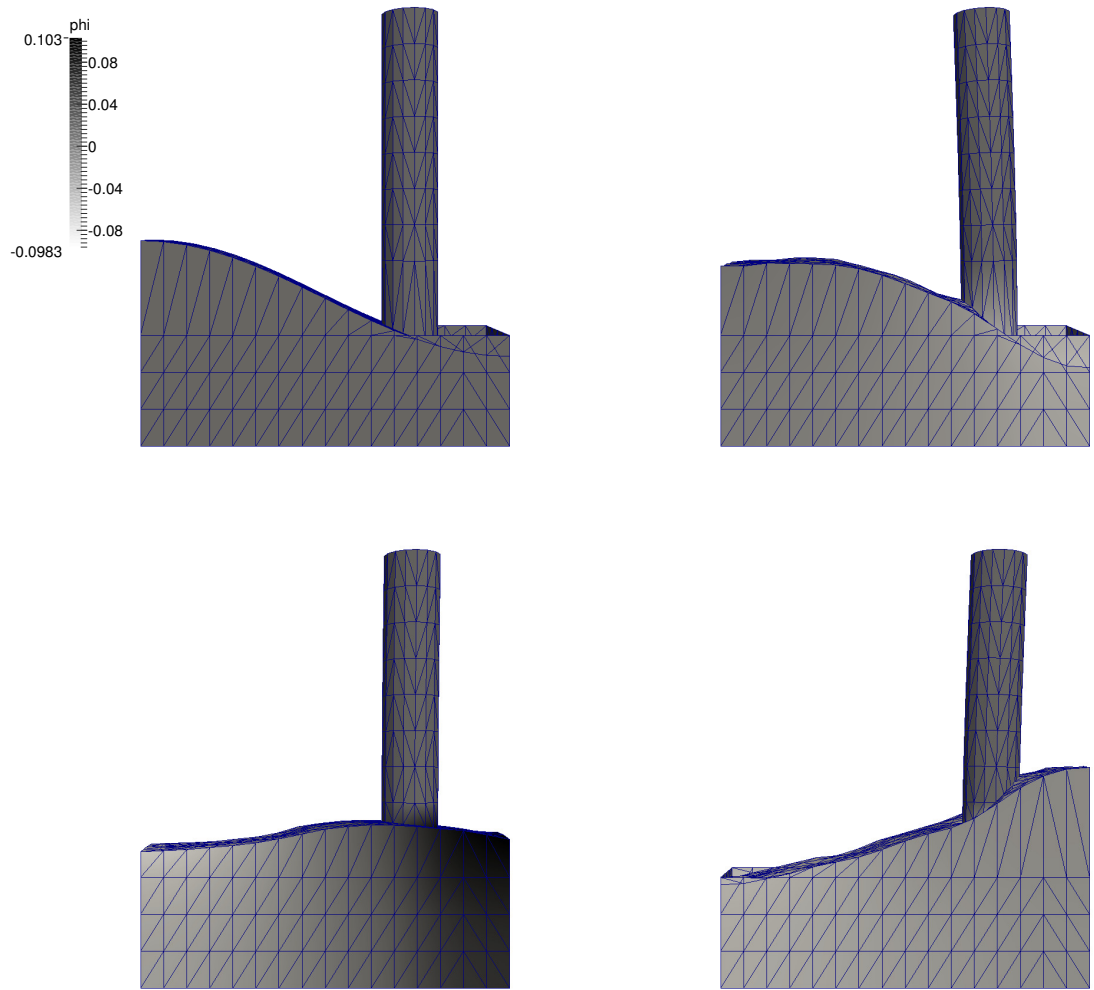


Figure 4.8: Temporal snapshots of the 3D water-beam geometry during flow evolution. Although the computational domain is fixed, results have been post-processed into physical space to visualize the deformations. (Top left) initial condition; no flow; motion initiated by free-surface displacement. Physical flow geometries after 1.1 s (bottom left), 3.8 s (top right) and 5.9 s (bottom right). Colours, white to black, indicate flow-potential values. A beam deflection is clearly evident.

4.5 Discussion

A fully coupled nonlinear variational model of a free-surface fluid-structure interaction has been formulated. The main benefit is the incorporation of a complex multi-domain, evolving-geometry, single-valued free-surface, transient problem within a unifying and computationally tractable framework with a novel approach to use the Lagrange multiplier γ to constrain the beam and fluid common boundary. After elimination of the Lagrange multiplier and the hydrostatic term, the system (4.13) of linearized water-wave dynamics coupled to an elastic beam, *i.e.*, a system of linearized fluid-structure interaction (FSI) equations, is equivalent to the FSI with the *ad hoc* coupling derived in Salwa et al. (2016b). The linear equations have been discretized using a dis/continuous variational FEM, employing techniques from Bokhove and Kalogirou (2016), leading to a fully coupled and stable linear FSI with overall energy conservation, *i.e.*, without any energy loss between the subsystems, as there are bounded oscillations in the total energy decreasing with the size of timestep, due to the symplectic solver used. In the final scheme (4.44) there appears an extra coupling term in the equation (4.44d) for the free-surface deviation at the fluid-structure boundary that is not obvious from the continuous equation (4.13c). This is a novel aspect that emerges from the variational approach. The numerical extension of these FSI to the nonlinear realm is planned as future research.

The next extension of the model will be to allow for rotational flow to model wave breaking where the free surface can overturn. Non-potential flow and the mixture theory Benitz et al. (2015); Bokhove et al. (2016) of the water-air phase can be used for this purpose. An alternative, which will be exploited, is to propose a compressible, van-der-Waals-like potential-flow fluid model, that enables the modelling of wave-breaking without actually introducing rotational flow.

The code used in the 3D computation is available here: <https://doi.org/10.5281/zenodo.816221>. A simplified 2D version is also published as a tutorial on Firedrake's website and presented in Chapter 6.

Chapter 5

Towards modelling and simulating breaking waves

5.1 Introduction

The main advantage of the incompressible potential-flow model is its simplicity and speed in calculations; it is accordingly considered an industrial benchmark for applications. However, the same simplicity can be a drawback when the simulation of more complex behaviour is required. In reality, impact events with steep waves usually involve wave breaking, which cannot be simulated with plain, incompressible potential flow due to lack of rotational degrees of freedom. Therefore, to correctly simulate real fluid-structure interaction one has to resort to different models.

One such model, analysed and developed in this chapter, is the attempt to simulate wave breaking through the use of an air-water mixture model, *e.g.* see Bokhove et al. (2016); Dumbser (2011). In this alternative approach, the free-surface “interface” is considered as a limiting transition quantified by the density jump between two constituent phases (and, optionally, an intermediate “transition zone”) of ideal gases of variable density. An equation of state is then introduced on the basis of a van-der-Waals-like fluid model with a pseudo phase transition between the two phases, which herein are taken as water and air.

The van-der-Waals system studied is a potential-flow limit of flow equations that are now heavily studied in the research community, including applications with floating bodies and dynamic structures (Golay et al., 2015). We note, however, that despite remaining within potential-flow formalism, the fluid under consideration is no longer incompressible.

The theory is verified through several models based on combinations of C^0 and/or C^∞ equations of state and/or sound speeds which admits progression through: first, a sharp-interface model; second, a smooth-interface model of which the sharp-interface is the limiting form, and; third, an infinitely differentiable model whose limiting form is also the sharp-interface one but which does not suffer (at the computational stage) from the discontinuities of the first two models.

Validation of the theory is achieved by noting that, in the incompressible limit, results therefrom agree to demonstrably high accuracy with those obtained from independent computations performed on the corresponding potential-flow model.

5.2 Compressible van-der-Waals-like fluid

The van-der-Waals-like fluid model presented below enables simplified treatment of breaking waves; its formulation and properties are now investigated.

5.2.1 Model formulation

Consider a compressible stratified fluid under the influence of gravity in a closed cuboid as domain with a modified van-der-Waals-like equation of state (EOS). The corresponding variational principle reads

$$0 = \delta \int_0^T \mathcal{L}[\rho, \phi] dt \equiv \delta \int_0^T \int_0^{L_x} \int_0^{L_y} \int_0^H \rho \partial_t \phi + \frac{1}{2} \rho |\nabla \phi|^2 + \rho g z + \rho U(\rho) - \rho \left(g z + Q(\rho_0(z)) + \frac{p}{\rho} \Big|_{\rho=0} \right) dx dy dz dt \quad (5.1)$$

with: Lagrangian $\mathcal{L}[\rho, \phi]$ depending on density $\rho = \rho(x, y, z, t)$ as a function of spatial coordinates (x, y, z) and time t , and the velocity potential $\phi = \phi(x, y, z, t)$ such that the velocity $\mathbf{u} = \nabla\phi$; internal energy $U(\rho)$; constant acceleration of gravity g ; domain scales L_x, L_y and H in the three spatial directions; and, final time T . Note that this is an extension of Luke's VP (3.1). The internal energy $U = U(\rho)$ and the related $Q(\rho)$ are chosen to be a function of density ρ as follows. The second thermodynamic law for the adiabatic process is

$$du = p dV = p d\left(\frac{m}{\rho}\right) = -\frac{pm}{\rho^2} d\rho. \quad (5.2)$$

Therefore, the internal energy density per unit mass is

$$U = \int_0^\rho \frac{p(\tilde{\rho})}{\tilde{\rho}^2} d\tilde{\rho}. \quad (5.3)$$

Moreover, one has

$$\begin{aligned} \delta(\rho U(\rho)) &= \rho U' \delta\rho + U \delta\rho \equiv Q(\rho) \delta\rho \\ &= \frac{p}{\rho} \delta\rho + \int_0^\rho \frac{p(\tilde{\rho})}{\tilde{\rho}^2} d\tilde{\rho} \delta\rho \\ &= \frac{p}{\rho} \delta\rho|_{\rho=0} + \int_0^\rho \frac{1}{\tilde{\rho}} \frac{\partial p(\tilde{\rho})}{\partial \tilde{\rho}} d\tilde{\rho} \delta\rho \\ &= \left(\frac{p}{\rho} |_{\rho=0} + Q(\rho) \right) \delta\rho, \end{aligned} \quad (5.4)$$

in which integration by parts was used as well as the definition

$$Q(\rho) \equiv \int_0^\rho \frac{1}{\tilde{\rho}} \frac{\partial p(\tilde{\rho})}{\partial \tilde{\rho}} d\tilde{\rho}. \quad (5.5)$$

Given these relations, variations of (5.1) become

$$\begin{aligned} 0 &= \int_0^T \int_0^{L_x} \int_0^{L_y} \int_0^H (\partial_t \phi + \frac{1}{2} |\nabla\phi|^2 + Q(\rho) - Q(\rho_0)) \delta\rho + \\ &\quad - (\partial_t \rho + \nabla \cdot (\rho \nabla \phi)) \delta\phi dV \\ &\quad + \rho \mathbf{n} \cdot \nabla \phi \delta\phi dS dt. \end{aligned} \quad (5.6)$$

The arbitrariness of $\delta\rho$ and $\delta\phi$ in (5.6) subsequently yields the following equations

$$\delta\phi : \quad \partial_t\phi + \frac{1}{2}|\nabla\phi|^2 + Q(\rho) - Q(\rho_0) = 0 \quad (5.7a)$$

$$\delta\rho : \quad \partial_t\rho + \nabla \cdot (\rho\nabla\phi) = 0 \quad (5.7b)$$

$$\delta\phi|_{\partial\Omega} : \quad \rho\mathbf{n} \cdot \nabla\phi = 0. \quad (5.7c)$$

The gradient of (5.7a) should give the inviscid momentum equation

$$\partial_t\mathbf{u} + \mathbf{u} \cdot \nabla\mathbf{u} = -\frac{1}{\rho}\nabla p + \mathbf{g}. \quad (5.8)$$

Since $\nabla Q = \frac{1}{\rho}\nabla p$, it is assumed that $\nabla Q(\rho_0) = (0, 0, \frac{dQ(\rho_0)}{dz})^T = (0, 0, -g)^T$, as $\rho_0 = \rho_0(z)$ is the density in the hydrostatic state. The static case with $\phi = 0$ or constant then defines the hydrostatic density profile $\rho_0(x)$ through:

$$-g = \frac{dQ(\rho_0(z))}{dz} = \frac{1}{\rho_0(z)} \frac{dp}{dz} = \frac{1}{\rho_0(z)} \frac{d\rho_0(z)}{dz} \frac{dp}{d\rho_0(z)}. \quad (5.9)$$

Three candidate EOSs are now considered.

5.2.2 Equations of state

C^0 EOS with discontinuous sound speed

The first simplified van-der-Waals fluid-type EOS considered consists of two linear sections, one for each of the “air” and “liquid” branches of the model, connected by a constant-pressure branch as follows:

$$p(\rho) = \begin{cases} c_a^2\rho & \rho \leq \rho_a \\ p_a = c_a^2\rho_a & \rho_a < \rho < \rho_w \\ p_a + c_w^2(\rho - \rho_w) & \rho \geq \rho_w \end{cases} \quad (5.10)$$

with $c_a^2 = RT \ll c_w^2$ with $R = 287 \text{ J/kg} \cdot \text{K}$ and $T \approx 270 \text{ K}$, such that $c_a \approx 316 \text{ m/s}$, and $c_w \approx 1500 \text{ m/s}$. Given this equation of state consider the equilibrium hydrostatic rest state for a given mass $M = \int_0^H \rho \, dz$ in a container of height H . When the pressure exceeds p_a , the density jumps from ρ_a to ρ_w at the unknown level h , $0 \leq h \leq H$, which models the free-surface position; at rest, $h = H_0$. The hydrostatic solution of (5.9) with equation of state (5.10) is

$$\rho_0(z) = \begin{cases} \rho_a \exp\left(-\frac{g}{c_a^2}(z - z_a)\right) & \text{for } \rho_0 \leq \rho_a, \quad z \geq z_a \\ \rho_w \exp\left(-\frac{g}{c_w^2}(z - z_w)\right) & \text{for } \rho_0 \geq \rho_w, \quad z \leq z_w. \end{cases} \quad (5.11)$$

For $\rho_a < \rho_0 < \rho_w$, $z_w < z < z_a$ the density is not defined. The simplest way to resolve this apparent anomaly is to assume that the transition zone has zero width $z_a = z_w = H_0$, and that there is a jump in density across the interface

$$\rho_0(z) = \begin{cases} \rho_a \exp\left(-\frac{g}{c_a^2}(z - H_0)\right) & \text{for } z > H_0 \\ \rho_w \exp\left(-\frac{g}{c_w^2}(z - H_0)\right) & \text{for } z \leq H_0. \end{cases} \quad (5.12)$$

Because of the shape of the solution, (5.10) will be referred to as the ‘‘sharp-interface’’ or ‘‘two-phase’’ model. In the limit $\rho_a \rightarrow 0$, $c_a \rightarrow \infty$, $c_w \rightarrow \infty$ such that $c_a^2 \rho_a = p_a$, (5.12) takes the form

$$\rho_0(z) = \begin{cases} 0 & \text{for } z > H_0 \\ \rho_w & \text{for } z \leq H_0 \end{cases} \quad (5.13)$$

and (5.10) becomes

$$p(z) = \begin{cases} p_a & \text{for } z > H_0 \\ p_a - \rho_w g(z - H_0) & \text{for } z \leq H_0 \end{cases}, \quad (5.14)$$

which represent an incompressible fluid with constant density ρ_w and surface at $z = H_0$. Quantification of how this limit is approached in the sharp-interface model is demonstrated in the two sub-figures in the top row of Fig.5.1.

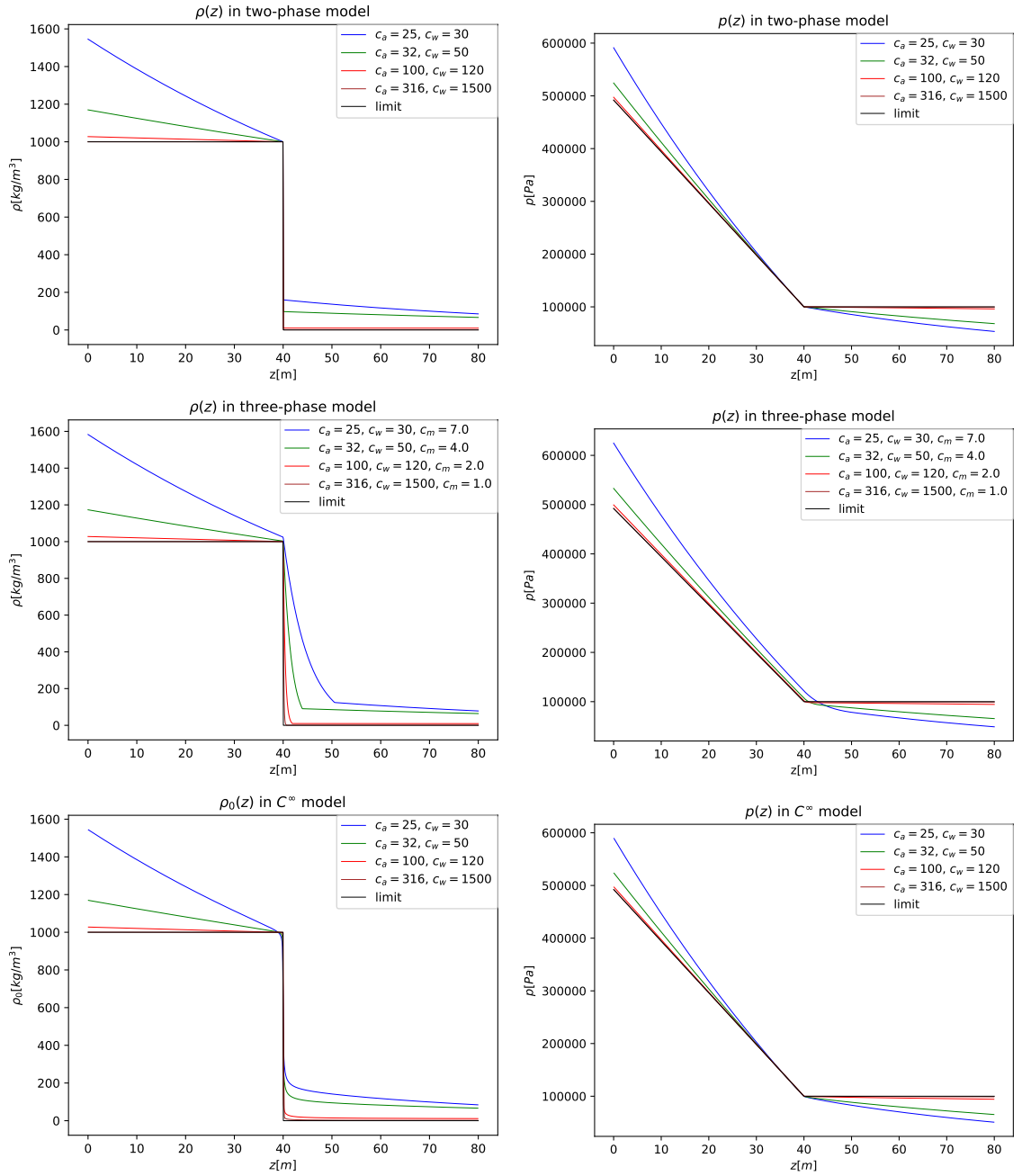


Figure 5.1: Two-phase (top), three-phase (middle) and C^∞ (bottom) interface models. Density (left) and pressure (right) in the limit $\rho_a \rightarrow 0$, $c_a \rightarrow \infty$, $c_w \rightarrow \infty$, $c_a^2 \rho_a = p_a = 1000 \text{ hPa}$, $\rho_w = 1000 \text{ kg/m}^3$ with colors: blue, green, red to brown as the values approach the incompressible limit (black). The interface is located at $H_0 = 40\text{m}$, while the total tank height $H = 80\text{m}$.

The value of the term $Q(\rho) - Q(\rho_0)$ in (5.7a) with equation of state (5.10) is

$$Q(\rho) - Q(\rho_0) = c_a^2 \ln \frac{\min(\rho, \rho_a)}{\min(\rho_0, \rho_a)} + c_w^2 \ln \frac{\max(\rho, \rho_w)}{\max(\rho_0, \rho_w)}. \quad (5.15)$$

C^0 EOS and speed of sound

An alternative to (5.10) is an equation of state that describes a “smooth-interface” or “three-phase” region,

$$p(\rho) = \begin{cases} c_a^2 \rho & \rho \leq \rho_* \\ p_a + c_m^2 (\rho - (\rho_a + \rho_w)/2) & \rho_* < \rho < \rho_{**} \\ p_a + c_w^2 (\rho - \rho_w) & \rho \geq \rho_{**} \end{cases} \quad (5.16)$$

in which $p_a = c_a^2 \rho_a$, and c_m is a small sound speed in the transition region, $c_m < c_a, c_w$. The continuity of pressure yields

$$\rho_* = (p_a - c_m^2 (\rho_a + \rho_w)/2) / (c_a^2 - c_m^2) \quad \text{and} \quad (5.17a)$$

$$\rho_{**} = (c_w^2 \rho_w - c_m^2 (\rho_a + \rho_w)/2) / (c_w^2 - c_m^2). \quad (5.17b)$$

With the equation of state (5.16) the term $Q(\rho) - Q(\rho_0)$ in (5.7a) becomes

$$Q(\rho) - Q(\rho_0) = c_a^2 \ln \frac{\min(\rho, \rho_*)}{\min(\rho_0, \rho_*)} + c_w^2 \ln \frac{\max(\rho, \rho_{**})}{\max(\rho_0, \rho_{**})} + c_m^2 \begin{cases} 0, & \rho_0 \leq \rho \wedge (\rho_{**} \leq \rho_0 \vee \rho \leq \rho_*) \\ \ln \frac{\min(\rho, \rho_{**})}{\max(\rho_0, \rho_*)}, & \rho_0 \leq \rho \wedge \rho_0 < \rho_{**} \wedge \rho_* < \rho \\ 0, & \rho < \rho_0 \wedge (\rho_{**} \leq \rho \vee \rho_0 \leq \rho_*) \\ \ln \frac{\max(\rho, \rho_*)}{\min(\rho_0, \rho_{**})}, & \rho < \rho_0 \wedge \rho < \rho_{**} \wedge \rho_* < \rho_0 \end{cases}. \quad (5.18)$$

The hydrostatic density resulting from (5.9) with the equation of state (5.16) is

$$\rho_0(z) = \begin{cases} \rho_* \exp(-\frac{g}{c_a^2}(z - H_*)), & z \geq H_* \\ \rho_{**} \exp(-\frac{g}{c_m^2}(z - H_0)), & H_* > z > H_0 \\ \rho_{**} \exp(-\frac{g}{c_w^2}(z - H_0)), & H_0 \geq z \end{cases}, \quad (5.19)$$

in which $H_* = H_0 + \frac{c_m^2}{g} \ln \frac{\rho_{**}}{\rho_*}$ to ensure density continuity, and H_0 is defined as the height at which the interface starts. In the limiting case $c_a, c_w \rightarrow \infty, c_m \rightarrow 0, \rho_a \rightarrow 0, c_a^2 \rho_a = p_a$, it is found that $\rho_* \rightarrow 0$ and $\rho_{**} \rightarrow \rho_w$. Assuming also that $c_m^2 \ln \frac{\rho_*}{\rho_{**}} \rightarrow 0$, which holds if c_m tends to zero as $\frac{1}{c_a}$, results (5.13) and (5.14) are obtained, *i.e.* as in the sharp-interface model. Quantification of the smooth-interface results is depicted in the two sub-figures in the middle row of Fig. 5.1, in which comparison of top and middle rows clearly evidences the limiting approach of the smooth-interface model to the sharp-interface one.

C^∞ EOS and speed of sound

Both equations of state (5.10) and (5.16) have the drawback that they are not differentiable (smooth) in the whole domain, as a direct result of which the numerical solution proves problematic. Therefore another equation of state is proposed that asymptotically tends to (5.10), but is C^∞ .

The starting point is to introduce an equation of the form

$$y_\pm(x, a, b) = \frac{a}{2} \left(x \pm \sqrt{x^2 + \frac{4b^2}{a^2}} \right) \quad (5.20)$$

which represents two branches of hyperbola centered at the coordinate origin, with asymptotes $y = 0$ and $y = ax$ and crossing the y -axis at $y = \pm b$; the described set-up is depicted in Fig. 5.2. This function admits proposal of an infinitely differentiable approximation of the equation of state (5.10):

$$p(\rho, b_a, b_w) = y_-(\rho - \rho_a, c_a^2, b_a) + y_+(\rho - \rho_w, c_w^2, b_w) + p_a. \quad (5.21)$$

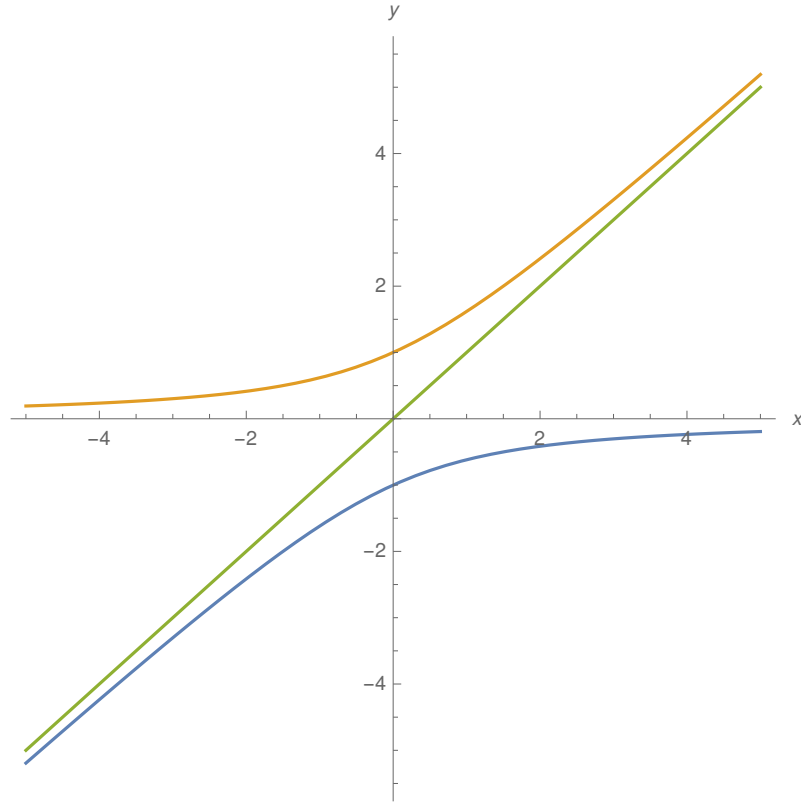


Figure 5.2: The hyperbola, described by setting $a = b = 1$ in equation (5.20) centred at the origin, with lower branch ('-'-blue), upper branch ('+'-yellow), asymptotes $y = 0$ and $y = x$ (green), crossing y - axis at $b = \pm 1$.

The two parameters $b_{a,w}$ dictate the proximity to (5.10) which is recovered without error when $b = 0$: see Fig. 5.3 for a graph of (5.21). In finding the hydrostatic state, the following integral is required

$$\int \frac{1}{x} \frac{d y_{\pm}(x - x_0, a, b)}{d x} d x = \frac{a}{2} \left\{ \ln x \pm \ln \left(x - x_0 + \sqrt{(x - x_0)^2 + \frac{4b^2}{a^2}} \right) \right. \\ \left. \pm \frac{x_0}{\sqrt{x_0^2 + \frac{4b^2}{a^2}}} \left[\ln \left(x_0^2 - x_0 x + \frac{4b^2}{a^2} + \sqrt{x_0^2 + \frac{4b^2}{a^2}} \sqrt{(x - x_0)^2 + \frac{4b^2}{a^2}} \right) - \ln x \right] \right\} \quad (5.22)$$

up to the integration constant. Then (5.9) can be solved numerically, yielding a hydrostatic-state pressure $p(z)$ and density profile $\rho_0(z)$ that are shown at the bottom

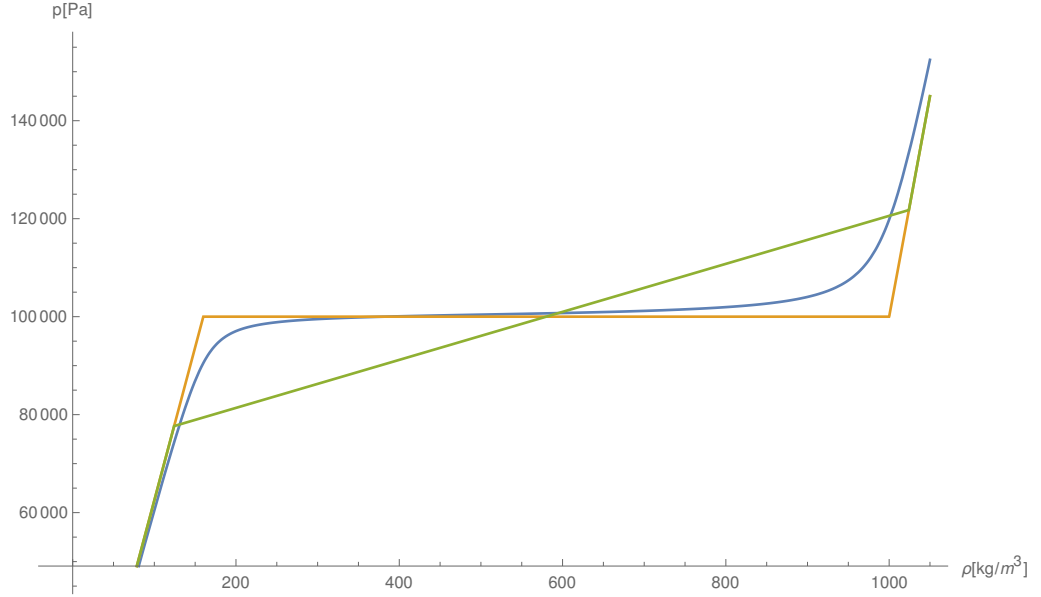


Figure 5.3: Equations of state: pressure as a function of density for the C^∞ model (blue) compared with the two-phase model (5.10) (yellow) and three-phase model (5.16) (green). Parameter values are: $c_a = 25$ m/s, $c_w = 30$ m/s, $c_m = 7$ m/s, $p_a = 1000$ hPa, $\rho_a = 160$ kg/m³, $\rho_w = 1000$ kg/m³, $b_a = 0.1p_a$, $b_w = 0.2p_a$.

of Fig. 5.1. Next, with (5.22) the driving terms can be computed analytically as $Q(\rho) - Q(\rho_0(z))$ in (5.7a). Using also (5.5) and (5.21), there results

$$\begin{aligned}
 Q(\rho) - Q(\rho_0(z)) &= \tag{5.23} \\
 &= \frac{c_a^2}{2} \left\{ \ln \frac{\rho}{\rho_0} - \ln \left(\frac{\rho - \rho_a + \sqrt{(\rho - \rho_a)^2 + \frac{4b_a^2}{c_a^4}}}{\rho_0 - \rho_a + \sqrt{(\rho_0 - \rho_a)^2 + \frac{4b_a^2}{c_a^4}}} \right) \right. \\
 &\quad \left. - \frac{\rho_a}{\sqrt{\rho_a^2 + \frac{4b_a^2}{c_a^4}}} \left[\ln \left(\frac{\rho_a^2 - \rho_a\rho + \frac{4b_a^2}{c_a^4} + \sqrt{\rho_a^2 + \frac{4b_a^2}{c_a^4}} \sqrt{(\rho - \rho_a)^2 + \frac{4b_a^2}{c_a^4}}}{\rho_a^2 - \rho_a\rho_0 + \frac{4b_a^2}{c_a^4} + \sqrt{\rho_a^2 + \frac{4b_a^2}{c_a^4}} \sqrt{(\rho_0 - \rho_a)^2 + \frac{4b_a^2}{c_a^4}}} \right) - \ln \frac{\rho}{\rho_0} \right] \right\} \\
 &\quad + \frac{c_w^2}{2} \left\{ \ln \frac{\rho}{\rho_0} + \ln \left(\frac{\rho - \rho_w + \sqrt{(\rho - \rho_w)^2 + \frac{4b_w^2}{c_w^4}}}{\rho - \rho_w + \sqrt{(\rho_0 - \rho_w)^2 + \frac{4b_w^2}{c_w^4}}} \right) \right. \\
 &\quad \left. + \frac{\rho_w}{\sqrt{\rho_w^2 + \frac{4b_w^2}{c_w^4}}} \left[\ln \left(\frac{\rho_w^2 - \rho_w\rho + \frac{4b_w^2}{c_w^4} + \sqrt{\rho_w^2 + \frac{4b_w^2}{c_w^4}} \sqrt{(\rho - \rho_w)^2 + \frac{4b_w^2}{c_w^4}}}{\rho_w^2 - \rho_w\rho_0 + \frac{4b_w^2}{c_w^4} + \sqrt{\rho_w^2 + \frac{4b_w^2}{c_w^4}} \sqrt{(\rho_0 - \rho_w)^2 + \frac{4b_w^2}{c_w^4}}} \right) - \ln \frac{\rho}{\rho_0} \right] \right\}.
 \end{aligned}$$

The value of $Q(\rho) - Q(\rho_0(z))$ so computed is shown as a function of ρ and z in Fig. 5.4.

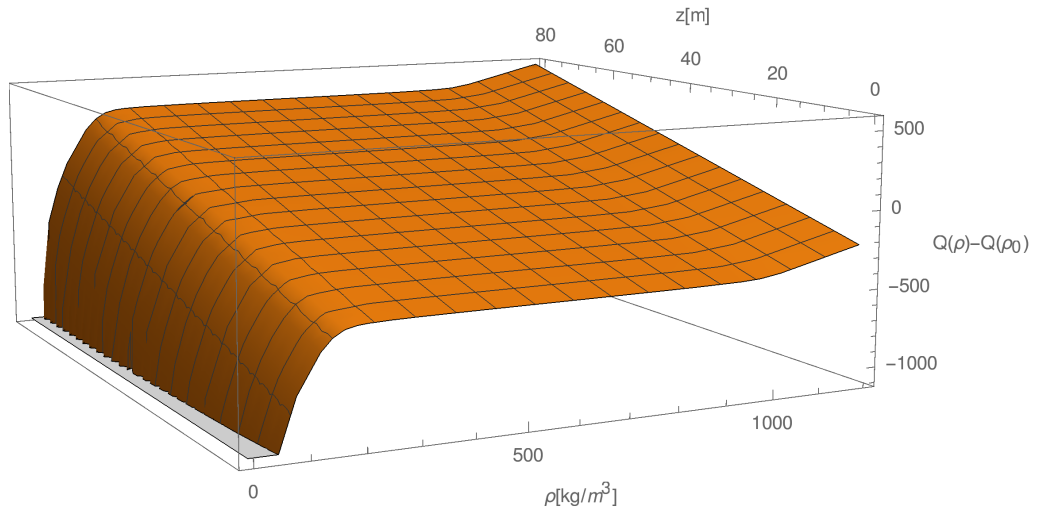


Figure 5.4: Driving term $Q(\rho) - Q(\rho_0(z))$ as a function of ρ and z . Parameter values are as given in the caption of Fig. 5.3 with the addition of $H_0 = 40\text{m}$.

5.3 Linear waves

The next test problem used to verify system (5.7) is one comprising linear waves. It is assumed that (tilded) perturbations around the hydrostatic state $\rho_0(z)$ are given by $\phi = 0 + \tilde{\phi}$ and $\rho = \rho_0(z) + \tilde{\rho}$, in which perturbations are considered to be small so that their quadratic and higher-order terms can be neglected. The resulting linearization is

$$\partial_t \tilde{\phi} + Q'_0 \tilde{\rho} = 0 \tag{5.24a}$$

$$\partial_t \tilde{\rho} + \rho'_0 \partial_z \tilde{\phi} + \rho_0 \nabla^2 \tilde{\phi} = 0 \tag{5.24b}$$

$$\mathbf{n} \cdot \nabla \tilde{\phi} = 0, \quad (5.24c)$$

in which the following notation has been used:

$$\frac{dQ}{d\rho} \Big|_{\rho_0(z)} = Q'(\rho_0) \equiv Q'_0 \quad (5.25a)$$

$$\frac{d\rho_0(z)}{dz} \equiv \rho'_0. \quad (5.25b)$$

The perturbation $\tilde{\rho}$ is first eliminated by taking the temporal derivative of (5.24a) and substituting $\partial_t \tilde{\rho}$ from (5.24b) to get

$$\partial_{tt} \tilde{\phi} - Q'_0(\rho'_0 \partial_z \tilde{\phi} + \rho_0 \nabla^2 \tilde{\phi}) = 0. \quad (5.26)$$

The substitution of $\tilde{\phi}(x, z, t) = \hat{\phi}(z) e^{i(kx - \omega t)}$ leads to an equation for $\hat{\phi}$ in the z -direction only:

$$Q'_0 \rho_0 \hat{\phi}'' + Q'_0 \rho'_0 \hat{\phi}' + (\omega^2 - Q'_0 \rho_0 k^2) \hat{\phi} = 0. \quad (5.27)$$

$$Q'_0 \frac{d}{dz} (\rho_0 \hat{\phi}') + (\omega^2 - Q'_0 \rho_0 k^2) \hat{\phi} = 0. \quad (5.28)$$

After substituting expressions for ρ_0 and Q'_0 there results

$$c^2 \hat{\phi}'' - g \hat{\phi}' + (\omega^2 - c^2 k^2) \hat{\phi} = 0. \quad (5.29)$$

The general solution of (5.29) is

$$\begin{aligned} \hat{\phi}(z) = & C^+ \exp \left[\frac{z}{2c^2} \left(g + \sqrt{g^2 + 4c^4 k^2 - 4c^2 \omega^2} \right) \right] \\ & + C^- \exp \left[\frac{z}{2c^2} \left(g - \sqrt{g^2 + 4c^4 k^2 - 4c^2 \omega^2} \right) \right], \end{aligned} \quad (5.30)$$

in which the constants C^\pm are discussed below. To simplify further expressions, the following notation is introduced:

$$\Delta_\alpha \equiv g^2 + 4c_\alpha^4 k^2 - 4c_\alpha^2 \omega^2, \quad G_\alpha^\pm \equiv \frac{1}{2c_\alpha^2} (g \pm \sqrt{\Delta_\alpha}) \quad \text{and} \quad E_\alpha^{\pm\beta} \equiv \exp [G_\alpha^\pm H_\beta]. \quad (5.31)$$

The particular solutions are denoted as

$$\hat{\phi}_\alpha^\pm(z) \equiv \exp \left[\frac{z}{2c_\alpha^2} \left(g \pm \sqrt{g^2 + 4c_\alpha^4 k^2 - 4c_\alpha^2 \omega^2} \right) \right]. \quad (5.32)$$

5.3.1 One-phase model

The constants C^\pm arising in (5.30) are now sought within the context of the dispersion relation, first in the simplest case of a single phase (with no interface). Since there is only one phase, subscripts are dropped from the terms defined in (5.31). Two boundary conditions emerge from (5.24c), namely $\hat{\phi}'(0) = 0$ and $\hat{\phi}'(H) = 0$, which yield the 2×2 linear system

$$\begin{pmatrix} (\hat{\phi}^+)'(0) & (\hat{\phi}^-)'(0) \\ (\hat{\phi}^+)'(H) & (\hat{\phi}^-)'(H) \end{pmatrix} \begin{pmatrix} C^+ \\ C^- \end{pmatrix} = \vec{0}. \quad (5.33)$$

System (5.33) has a solution if the determinant of its matrix is zero, which gives

$$(\omega^2 - c^2 k^2) \sinh \left(\frac{H}{2c^2} \sqrt{\Delta} \right) = 0. \quad (5.34)$$

There are three cases to consider:

I) For $\Delta > 0$, equation (5.34) is satisfied if and only if $\omega = \pm ck$. Boundary conditions yield $C^+ = 0$ and, denoting $C^- \equiv C$, the solution takes the form: $\hat{\phi}(z) = C$.

II) For $\Delta = 0$ (5.34) is automatically satisfied and the dispersion relation is $\omega^2 = g^2/4c^2 + c^2 k^2$. However, boundary conditions require that $C^+ = C^- = 0$, so the solution is trivial, *i.e.* $\hat{\phi}(z) = 0$.

III) For $\Delta < 0$ there exists a nontrivial solution satisfying (5.34) if

$$\sinh\left(i\frac{H\sqrt{-\Delta}}{2c^2}\right) = i\sin\left(\frac{H\sqrt{-\Delta}}{2c^2}\right) = 0, \quad (5.35)$$

which holds if

$$\frac{H\sqrt{-\Delta}}{2c^2} = n\pi, \quad n \in \{1, 2, \dots\}, \quad (5.36)$$

or

$$\omega^2 = \frac{g^2}{4c^2} + c^2k^2 + \frac{c^2n^2\pi^2}{H^2}. \quad (5.37)$$

Note that $n = 0$ gives case II. The solution then takes the form

$$\hat{\phi}(z) = C \exp\left(\frac{gz}{2c^2}\right) \cos\left(\frac{n\pi z}{H}\right). \quad (5.38)$$

5.3.2 C^0 EOS and discontinuous speed of sound

In the sharp-interface, or two-phase model (5.10), the sound speed is

$$c = \begin{cases} c_a & \text{for } z > H_0 \\ c_w & \text{for } z \leq H_0 \end{cases} \quad (5.39)$$

and there are now four integration constants $C_{w,a}^\pm$. In addition to the two boundary conditions, as previously, $\hat{\phi}'(0) = 0$ and $\hat{\phi}'(H) = 0$, continuity across the interface is demanded of ϕ , so $\hat{\phi}(H_0^-) = \hat{\phi}(H_0^+)$, and of the flux, so $\rho_0\hat{\phi}'|_{z=H_0^-} = \rho_0\hat{\phi}'|_{z=H_0^+}$; see equation (5.28). These yield the 4×4 linear system

$$\begin{pmatrix} (\hat{\phi}_a^+)'(H) & (\hat{\phi}_a^-)'(H) & 0 & 0 \\ 0 & 0 & (\hat{\phi}_w^+)'(0) & (\hat{\phi}_w^-)'(0) \\ \hat{\phi}_a^+(H_0) & \hat{\phi}_a^-(H_0) & -\hat{\phi}_w^+(H_0) & -\hat{\phi}_w^-(H_0) \\ \rho_a(\hat{\phi}_a^+)'(H_0) & \rho_a(\hat{\phi}_a^-)'(H_0) & -\rho_w(\hat{\phi}_w^+)'(H_0) & -\rho_w(\hat{\phi}_w^-)'(H_0) \end{pmatrix} \begin{pmatrix} C_a^+ \\ C_a^- \\ C_w^+ \\ C_w^- \end{pmatrix} = \vec{0}, \quad (5.40)$$

which has nontrivial solution only if the determinant of its matrix is zero, which yields

$$\begin{aligned}
 0 = & G_a^{-2} G_w^+ \rho_w \left(-e^{(H+H_0)G_a^- + H_0 G_a^+} \right) - G_a^+ G_w^- G_w^+ \rho_w e^{H_0(G_a^- + G_w^+) + H G_a^+} \\
 & + G_a^- \left(G_w^- e^{H_0 G_w^+} \left(G_a^+ \rho_a \left(e^{H_0 G_a^- + H G_a^+} - e^{H G_a^- + H_0 G_a^+} \right) + G_w^+ \rho_w e^{H G_a^- + H_0 G_a^+} \right) \right. \\
 & \left. - G_a^+ G_w^+ \left(\rho_a \left(e^{H_0(G_a^- + G_w^-) + H G_a^+} - e^{H_0(G_a^+ + G_w^-) + H G_a^-} \right) - \rho_w e^{2H_0 G_a^- + H G_a^+} \right) \right)
 \end{aligned} \tag{5.41}$$

Equation (5.41) can be solved numerically for $\omega(k)$; the dispersion-relation curves are shown in Fig. 5.5 in which, unfortunately, the gravity-wave branch is not present.

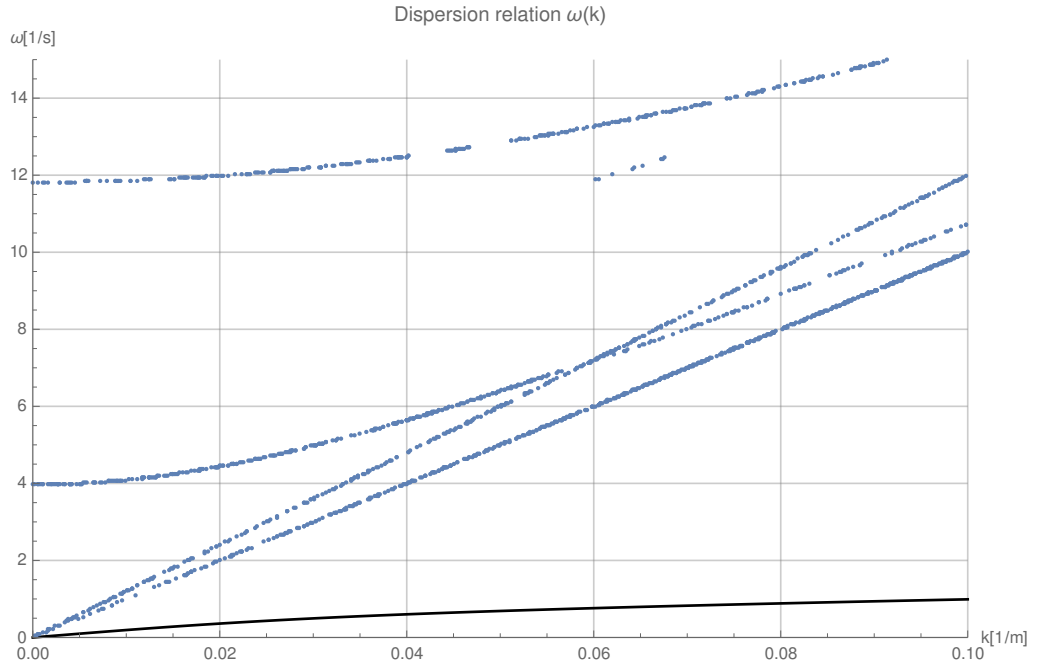


Figure 5.5: Dispersion curves computed from (5.41) for the pseudo two-phase model. Parameter values are: $c_w = 120\text{m/s}$, $c_a = 100\text{m/s}$, $c_m = 2\text{m/s}$, $H_0 = 40\text{m}$, $H = 80\text{m}$, $\rho_w = 1000\text{kg/m}^3$, $p_a = 10^5\text{Pa}$. The black curve represents the gravity-wave dispersion relation, and its presence reveals the absence of gravity-wave modes in the solution of the dispersion relation (5.41).

5.3.3 C^0 EOS and speed of sound

In the case of a smooth interface, or three-phase model (5.16), the sound speed is given by

$$c = \begin{cases} c_a & z \geq H_* \\ c_m & \text{for } H_0 < z < H_* \\ c_w & z \leq H_0 \end{cases} \quad (5.42)$$

and there are now six integration constants $C_{a,m,w}^\pm$. To determine them, two boundary conditions, $\hat{\phi}'|_{z=0,H} = 0$, are first used, as above. In this case, continuity conditions across both sides of the interface can be used. First, continuity of the flow potential gives $\hat{\phi}(H_0^+) = \hat{\phi}(H_0^-)$ and $\hat{\phi}(H_*^+) = \hat{\phi}(H_*^-)$. Second, continuity of the flux gives $\rho_0 \frac{d\hat{\phi}}{dz}$. However, since density ρ_0 is continuous in this model, this reduces to flow continuity. Thus the residual conditions are $\hat{\phi}'(H_0^+) = \hat{\phi}'(H_0^-)$ and $\hat{\phi}'(H_*^+) = \hat{\phi}'(H_*^-)$. These result in 6×6 homogeneous linear system, similar to (5.33), for the vector of unknowns $(C_a^+, C_a^-, C_w^+, C_w^-, C_m^+, C_m^-)^T$ with system matrix

$$\begin{pmatrix} (\hat{\phi}_a^+)'(H) & (\hat{\phi}_a^-)'(H) & 0 & 0 & 0 & 0 \\ 0 & 0 & (\hat{\phi}_w^+)'(0) & (\hat{\phi}_w^-)'(0) & 0 & 0 \\ \hat{\phi}_a^+(H_*) & \hat{\phi}_a^-(H_*) & 0 & 0 & -\hat{\phi}_m^+(H_*) & -\hat{\phi}_m^-(H_*) \\ (\hat{\phi}_a^+)'(H_*) & (\hat{\phi}_a^-)'(H_*) & 0 & 0 & -(\hat{\phi}_m^+)'(H_*) & -(\hat{\phi}_m^-)'(H_*) \\ 0 & 0 & \hat{\phi}_w^+(H_0) & \hat{\phi}_w^-(H_0) & -\hat{\phi}_m^+(H_0) & -\hat{\phi}_m^-(H_0) \\ 0 & 0 & (\hat{\phi}_w^+)'(H_0) & (\hat{\phi}_w^-)'(H_0) & -(\hat{\phi}_m^+)'(H_0) & -(\hat{\phi}_m^-)'(H_0) \end{pmatrix}. \quad (5.43)$$

Equating the determinant of (5.43) zero yields the implicit dispersion relation. Using the further notation

$$\begin{aligned}
 W &= E_m^{+0} E_m^{-0} (G_m^- - G_m^+) \\
 W^+ &= G_m^- E_m^{-0} (G_w^- E_w^{+0} - G_w^+ E_w^{-0}) - G_w^+ G_w^- E_m^{-0} (E_w^{+0} - E_w^{-0}) \\
 W^- &= G_w^- G_w^+ E_m^{+0} (E_w^{+0} - E_w^{-0}) - G_m^+ E_m^{+0} (G_w^- E_w^{+0} - G_w^+ E_w^{-0}) \\
 W^0 &= \frac{G_m^+ E_m^{+*} W^+ + G_m^- E_m^{-*} W^-}{G_a^- E_a^{-H} G_a^+ E_a^{+*} - G_a^+ E_a^{+H} G_a^- E_a^{-*}},
 \end{aligned} \tag{5.44}$$

the dispersion relation is

$$\frac{G_a^+ G_a^- (E_a^{-H} E_a^{+*} - E_a^{+H} E_a^{-*})}{G_a^- E_a^{-H} E_a^{+*} - G_a^+ E_a^{+H} E_a^{-*}} = \frac{W^+ G_m^+ E_m^{+*} + W^- G_m^- E_m^{-*}}{W^+ E_m^{+*} + W^- E_m^{-*}}, \tag{5.45}$$

which, as before, can be solved numerically. The integration constants may be expressed as follows

$$\begin{aligned}
 C_w^+ &= CW G_w^- \\
 C_w^- &= -CW G_w^+ \\
 C_m^+ &= CW^+ \\
 C_m^- &= CW^- \\
 C_a^+ &= CW^0 G_a^- E_a^{-H} \\
 C_a^- &= -CW^0 G_a^+ E_a^{+H}.
 \end{aligned} \tag{5.46}$$

The dispersion curves are presented in Fig. 5.6. Unlike the two-phase case, the gravity-wave branch is now represented up to $k = 2 \text{ m}^{-1}$.

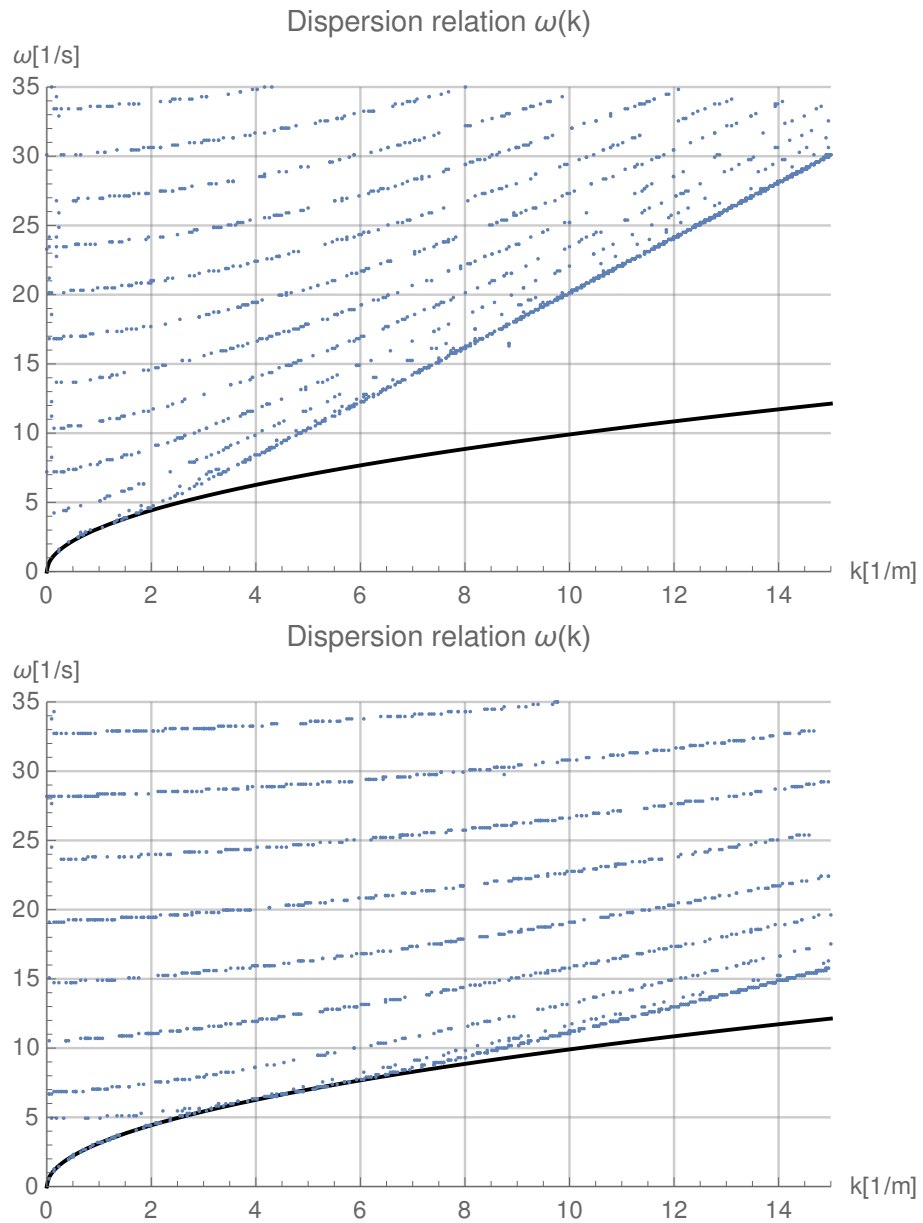


Figure 5.6: Dispersion curves for three-phase model, for which results up to $k = 2 \text{ m}^{-1}$ now agree with the gravity-wave dispersion relation shown by the black line. Parameter values are (top) $c_a = 100 \text{ m/s}$, $c_w = 120 \text{ m/s}$, $c_a = 2 \text{ m/s}$ and (bottom) $c_a = 316 \text{ m/s}$, $c_w = 1500 \text{ m/s}$, $c_a = 1 \text{ m/s}$.

5.3.4 Fluid in a box

In this section the flow is considered of pseudo three-phase model in a box with boundary conditions $\frac{d\phi}{dx}|_{x=0,L} = 0$, for which the solution takes the form

$$\phi = \hat{\phi}(z) \cos kx \cos \omega t \quad (5.47a)$$

$$\rho = \rho_0(z) \left(1 + \frac{\omega}{c^2} \hat{\phi}(z) \cos kx \sin \omega t \right) \quad (5.47b)$$

$$\text{with } k = \frac{n\pi}{L}, \quad n \in \mathbb{Z}, \quad (5.47c)$$

in which

$$c = \begin{cases} c_w & z \leq H_0 \\ c_m & \text{for } H_0 < z < H_* \\ c_a & z \geq H_* \end{cases} \quad (5.48)$$

The profile of $\hat{\phi}$ is presented in Fig. 5.7 and compared, for $z \leq H_0$, with the ϕ obtained independently from linear potential-flow water-waves theory: the agreement between the results of the two models is manifestly clear.

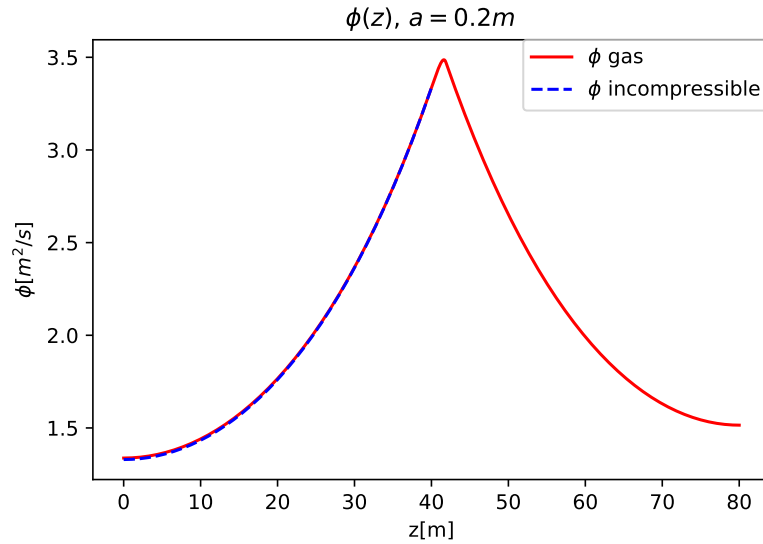


Figure 5.7: The profile of $\hat{\phi}$ (red line) from the three-phase gas model compared, for $z \geq 0$, with ϕ from linear potential-flow water-wave theory (dashed blue line). Parameter values are $c_a = 100$ m/s, $c_w = 120$ m/s, $c_a = 2$ m/s.

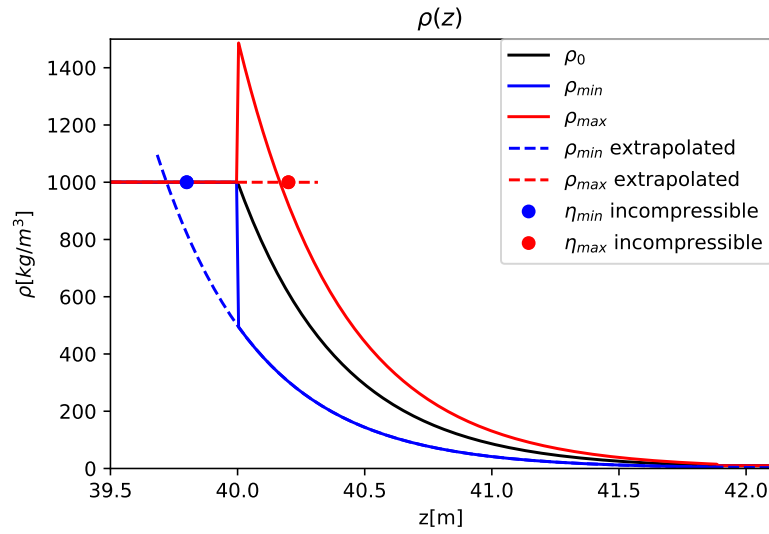


Figure 5.8: Linear ρ at $x = 0$ and $\omega t = 0, \frac{\pi}{2}, \frac{3\pi}{2}$ corresponding to initial (hydrostatic, black), maximal (red) and minimal (min) displacement values. The reconstructed position of the free surface is obtained as the intersection of extrapolated solutions from different regions (dashed lines). The free-surface deviation η from the equilibrium given by linear potential-flow water waves with amplitude 0.2m is added for comparison (blue and red dots). Parameter values are as in the caption of Figure 5.7.

Because of the jump in the value of c , the solution (5.47b) for ρ also contains a jump, see Fig. 5.8, which is a result of the linearization of $Q(\rho)$ in (5.7a) yielding (5.24a). In the nonlinear model there is no discontinuity, so one attempt to improve this solution to be useful as an initial value for the nonlinear solver is the following. Note that, in Fig. 5.8, the free-surface level from the linear potential-flow water waves lies close to the intersection of extrapolated lines, *i.e.*, the solutions from different regions. The intersection point can be then associated with the water level. Fig. 5.9 shows a comparison between the water levels reconstructed in this way and obtained from the incompressible linear potential-flow model.

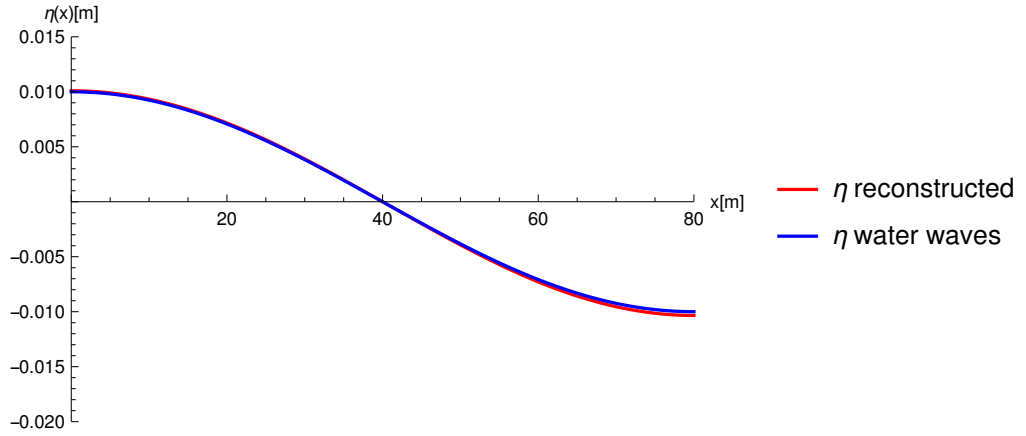


Figure 5.9: Free-surface level obtained by finding the intersection point between extrapolated solutions of the water and middle regions, compared with linear potential-flow water waves at their maximal deviation of amplitude of 0.01m. Parameter values are as in the caption of Figure 5.7.

5.4 Nonlinear results

The dispersion-relation approach of the previous section is precluded in the case of nonlinearity, which demands that all results be obtained numerically. To this end, finite element (FE) computations are automated in Firedrake (Rathgeber et al., 2016), which accepts the weak form of the equations of motion. In the present case, the weak form of the equations of motion (5.7) is

$$\int (\partial_t \phi + \frac{1}{2} |\nabla \phi|^2 + Q(\rho) - Q(\rho_0)) \delta \rho \, dV = 0 \quad (5.49a)$$

$$\int (\delta \phi \partial_t \rho - \rho \nabla \phi \cdot (\nabla \delta \phi)) \, dV = 0. \quad (5.49b)$$

Firedrake automates FE discretisation in space, yet temporal discretisation has to be performed manually. To this end, the implicit midpoint scheme can be used:

$$\int \left(\frac{1}{\Delta t} (\phi^{n+1} - \phi^n) + \frac{1}{2} |\nabla (\phi^n + \phi^{n+1})/2|^2 + Q((\rho^n + \rho^{n+1})/2) - Q(\rho_0) \right) \delta \rho \, dV = 0 \quad (5.50a)$$

$$\int \left(\frac{\delta\phi}{\Delta t} (\rho^{n+1} - \rho^n) - (\rho^n + \rho^{n+1})/2 \nabla(\phi^n + \phi^{n+1})/2 \cdot \nabla\delta\phi \right) dV = 0. \quad (5.50b)$$

Since the in-built nonlinear solver of Firedrake may have difficulty with the nonlinearity in $Q(\rho)$, an alternative is to consider a partial Picard iteration starting with $\phi^{(k=1)} = \phi^n$, yielding an iteration scheme with iterates

$$\int \left(\frac{\delta\phi}{\Delta t} (\rho^{(k+1)} - \rho^n) - (\rho^n + \rho^{(k+1)})/2 \nabla(\phi^n + \phi^{(k)})/2 \cdot \nabla\delta\phi \right) dV = 0 \quad (5.51a)$$

$$\int \left(\frac{1}{\Delta t} (\phi^{(k+1)} - \phi^n) + \frac{1}{2} |\nabla(\phi^n + \phi^{(k+1)})/2|^2 + Q((\rho^n + \rho^{(k+1)})/2) - Q(\rho_0) \right) \delta\rho dV = 0, \quad (5.51b)$$

in which convergence is assured if and only if, for some suitable threshold value of ϵ , temporal iterates satisfy $|\phi^{(k+1)} - \phi^{(k)}|_{L^\infty} < \epsilon$; an analogous result is demanded on temporal iterates of ρ , and another norm could also be used.

An alternative to Picard iteration is the use of the symplectic Euler scheme in the following form:

$$\int \left(\frac{\delta\phi}{\Delta t} (\rho^{n+1} - \rho^n) - \rho^{n+1} \nabla\phi^n \cdot \nabla\delta\phi \right) dV = 0 \quad (5.52a)$$

$$\int \left(\frac{1}{\Delta t} (\phi^{n+1} - \phi^n) + \frac{1}{2} |\nabla\phi^n|^2 + Q(\rho^{n+1}) - Q(\rho_0) \right) \delta\rho dV = 0. \quad (5.52b)$$

Equations (5.52) can be reformulated as

$$\int \rho^{n+1} (\delta\phi - \Delta t \nabla\phi^n \cdot \nabla\delta\phi) dV = \int \rho^n \delta\phi dV \quad (5.53a)$$

$$\int \phi^{n+1} \delta\rho dV = \int \left(\phi^n - \Delta t \left(\frac{1}{2} |\nabla\phi^n|^2 + Q(\rho^{n+1}) - Q(\rho_0) \right) \right) \delta\rho dV. \quad (5.53b)$$

Since the left-hand side of (5.53a) is a bilinear form of an unknown function ρ^{n+1} and a test function $\delta\phi$, it can be solved with a linear solver. Once (5.53a) is solved, both ρ^{n+1} and the right-hand side of (5.53b) are known. Therefore an explicit integration step can

be again performed with a linear solver, thereby entirely avoiding the use of nonlinear solvers. This approach has the disadvantage that there is a timestep criterion based on the minimum mesh size and the maximum wave frequency present in the discrete model.

5.4.1 C^0 EOS and discontinuous speed of sound

The schemes outlined above have been tested with different initial states in two dimensions. First, a hydrostatic state was verified for all three equations of state: if the scheme functions properly, the initial profile should be preserved, *i.e.*, there should be no motion. Second, the linear solution from section 5.3.4 was tried but the results showed that small free-surface deflections were overwhelmed with rapidly excited acoustic waves. The third attempt was therefore to use as an initial configuration a gravity wave with a higher amplitude. The free surface of the hydrostatic state was accordingly moved at each point using a formula for the free-surface deflection taken from linear potential-flow water waves. Specifically, for the initial free-surface deviation $\eta_0(x) = a \cos kx$, the starting density for the two-phase model is (*cf.* equation (5.12))

$$\rho_{\text{init}}(x, z) = \begin{cases} \rho_a \exp\left(-\frac{g}{c_a^2}(z - H_0 - \eta_0(x))\right) & \text{for } z > H_0 + \eta_0(x) \\ \rho_w \exp\left(-\frac{g}{c_w^2}(z - H_0 - \eta_0(x))\right) & \text{for } z \leq H_0 + \eta_0(x). \end{cases} \quad (5.54)$$

It is recalled that $k = \frac{2\pi}{\lambda}$ with λ being the wave length. The results for $\lambda = 2L$, where L is the length of the domain, are presented in Fig. 5.10. The excitation of acoustic modes is evident. Moreover, the solution is unstable in the long term and inevitably ends up with divergent results. The time t_{div} at which this divergence occurs is timestep- and mesh-resolution dependent; some examples are shown in Table 5.1. The gravity-wave period for this value of L is 10.57s, computed with $T = 2\pi/\sqrt{k \tanh(kH_0)}$. The same formula can be used to get an estimate of the maximal timestep needed to simulate the shortest gravity waves for a given mesh. For the mesh used to obtain the results in Fig. 5.10, $\Delta x = 4\text{m}$ and minimal $\Delta z = 0.7\text{m}$, which gives an estimate of $\Delta t_{\text{max}} = 0.67\text{s}$. On the

other hand, for $c_w = 120\text{m/s}$, stability criterion (2.37) requires that $\Delta t \leq 0.0037s$.

Tests with Störmer-Verlet and modified midpoint schemes yielded qualitatively similar results. Also, changing Newton nonlinear solver to Richardson one in Firedrake, or directly implementing Picard iteration did not improve the final outcome. Similar results, *i.e.* divergence at similar time, have been obtained for the three-phase model. The C^∞ model exhibited even worse behaviour, not yielding a stable solution for nonlinear waves.

Table 5.1: Simulation time until divergence t_{div} for a given timestep size for the symplectic Euler scheme, on a reference mesh (left) and one that has been refined by splitting (right).

Reference mesh		Refined mesh	
$\Delta t[s]$	$t_{\text{div}}[s]$	$\Delta t[s]$	$t_{\text{div}}[s]$
10^{-3}	7.7	10^{-3}	2.35
10^{-4}	8.7	10^{-4}	2.85
$5 \cdot 10^{-5}$	12.6	$5 \cdot 10^{-5}$	2.8
10^{-5}	8.1	10^{-5}	2.7

5.5 Conclusions

Several models for simulating wave breaking were analysed in this chapter. Common to all approaches was the underlying consideration of an air-to-water free surface as a transition, whose sharpness can be parameterised, in densities across the interface of a two-phase (optionally three-phase) van-der-Waals-like fluid model. The progression of models culminated in an infinitely differentiable one, validation of which was demonstrated by showing through numerical experiments that its limiting (transition-gradient) form yielded results that agreed to high accuracy with those obtained from corresponding potential-flow models. The research undertaken in the chapter can be considered as preliminary work whose results suggest the following recommendations for future research.

- The linear-wave solutions of the mixture system from Bokhove et al. (2016) should

be derived (exactly), in the potential-flow limit, and with a sharp interface, around the resting, hydrostatic state. These linear equations are the same as the linearized system of the two-layer (water and air) potential-flow equations found in Whitham (1999) (§13.7). The resulting solutions should then be used in the study of the linearized wave solutions of the van-der-Waals-system, derived in the later parts of this chapter, as these will be improved solutions yielding a better comparison with the van-der-Waals solutions.

- The hydrostatic state of the C^∞ EOS should be investigated, including its convergence to the hydrostatic state in the incompressible limit, as was done for the other EOS.
- The system of equations for the C^∞ case, linearized around the hydrostatic state, should be studied more carefully in several ways. First, the discretization of this linearized system can be studied within Firedrake, to test the temporal discretization and solvers. Second, a zonal harmonic-wave Ansatz can be used to reduce the equations to (z, t) -coordinates, thus facilitating a study of: (a) harmonic-wave solutions, with a further, finite-element discretization in the vertical, akin to the one for the nonlinear system implemented in Firedrake, as well as; (b) time discretizations testing a further, finite-element discretization in the vertical, akin to the one in Firedrake. In essence, (b) is a linear-stability analysis of the numerical system, which could address the convergence issues hitherto observed.
- Given these outcomes of linear stability and convergence, the preconditioners of semi-implicit time-stepping schemes for the nonlinear system should be investigated, which could further address the observed stalling of convergence of the iterative solvers.
- Various non-symplectic solvers can be investigated, including those that dampen the acoustic waves and those that are a combination of symplectic solvers with a dedicated filtering of the acoustic modes.

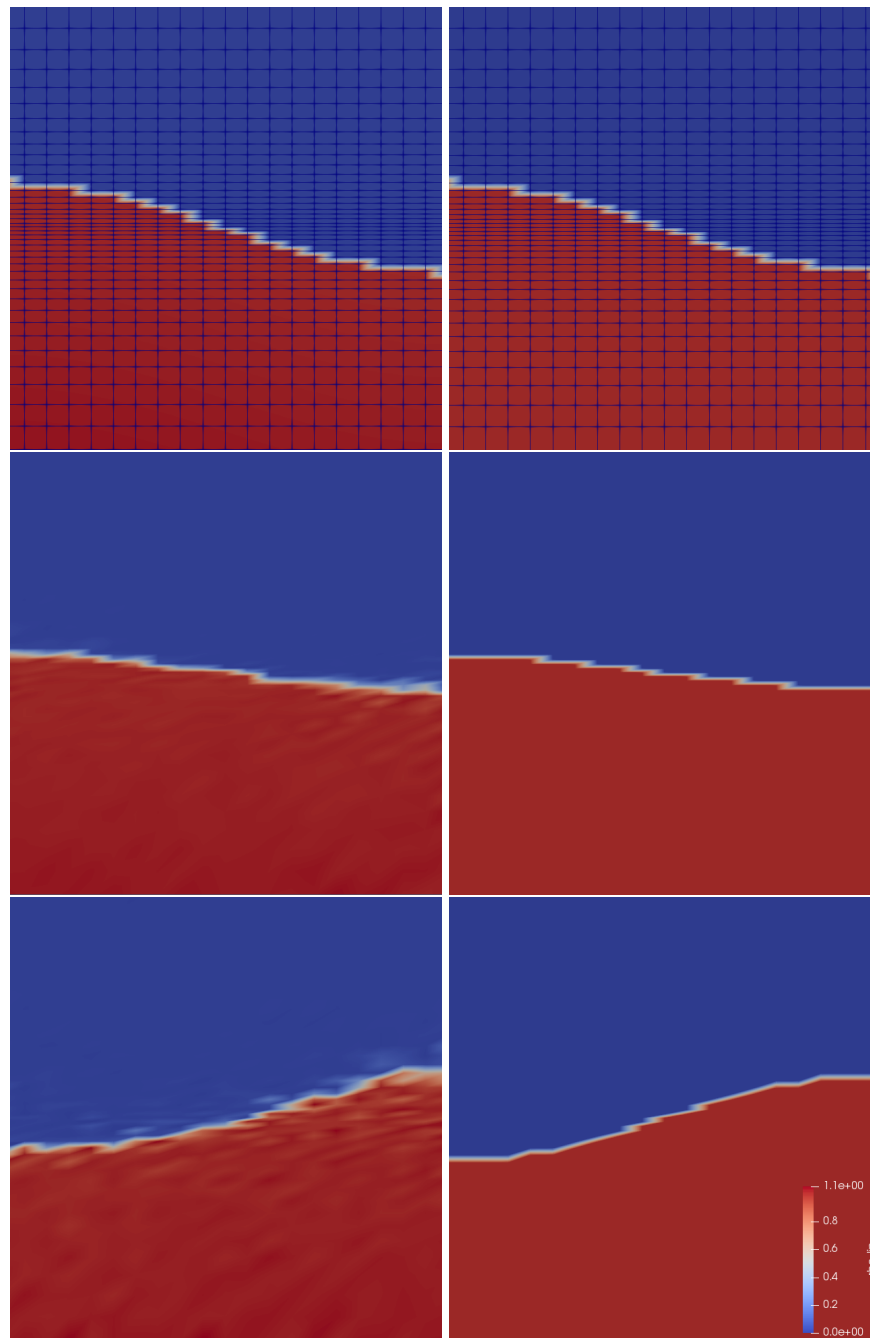


Figure 5.10: Density-profile evolution in the 2D two-phase model (left) compared with the profile in the incompressible, linear potential-flow water-wave model mapped onto the same mesh (right) at times 0 (top) 2 (middle) and 5 seconds (bottom). The top figures also display the mesh, for which the uniform horizontal spacing is $\Delta x = 4\text{m}$ and the minimum vertical spacing is $\Delta z = 0.7\text{m}$. The initial state for the gas model is constructed as the hydrostatic state with a shifted level of the free surface at each point, the shift corresponding to the level from the incompressible case. The growth of acoustic modes with time is clearly evident. Parameter values used (see main text for description) are: $a = 8\text{m}$, $\lambda = 160\text{m}$, $c_w = 120\text{m/s}$, $c_a = 100\text{m/s}$, $c_m = 2\text{m/s}$, $H_0 = 40\text{m}$, $H = 80\text{m}$, $L = 80\text{m}$, $\rho_w = 1000\text{kg/m}^3$, $p_a = 10^5\text{Pa}$.

Chapter 6

Code tutorial

“Firedrake is an automated system for the portable solution of partial differential equations using the finite element method (FEM)” (Rathgeber et al., 2016). It has been used extensively to implement the models in preceding chapters and it largely helped to facilitate the overall process. Since Firedrake is in ongoing development, users are welcome to contribute to it. Therefore a simplified 2D version of the linear potential flow fluid interacting with the elastic beam has been added to Firedrake demos available on its website. In this chapter this tutorial is presented, that is directly available at https://firedrakeproject.org/demos/linear_fluid_structure_interaction.py.html.

6.1 Linear mixed fluid-structure interaction system

The tutorial demonstrates the use of subdomain functionality and shows how to describe a system consisting of multiple materials in Firedrake.

The work is based on the articles Salwa et al. (2016b) and Salwa et al. (2017).

The model considered consists of fluid with a free surface and an elastic solid. The notions of fluid/water and structure/solid/beam will be used interchangeably. For simplicity (and

speed of computation) a model is considered in 2D, however it can be easily generalized to 3D. The starting point is the linearized version (domain is fixed) of the fully nonlinear variational principle. In non-dimensional units:

$$\begin{aligned}
 0 = & \delta \int_0^{t_{\text{end}}} \int \left(\partial_t \eta \phi - \frac{1}{2} \eta^2 \right) dS_f - \int \frac{1}{2} |\nabla \phi|^2 dx_F \\
 & + \int \mathbf{n} \cdot \partial_t \mathbf{X} \phi ds_s \\
 & + \int \rho_0 \partial_t \mathbf{X} \cdot \mathbf{U} - \frac{1}{2} \rho_0 |\mathbf{U}|^2 - \frac{1}{2} \lambda e_{ii} e_{jj} - \mu e_{ij} e_{ij} dx_S dt,
 \end{aligned}$$

in which the first line contains integration over fluid domain, second, fluid-structure interface, and third, structure domain. The following notions are used:

- η - free surface deviation
- ϕ - fluid flow potential
- ρ_0 - structure density (in fluid density units)
- λ - first Lamé constant (material parameter)
- μ - second Lamé constant (material parameter)
- \mathbf{X} - structure displacement
- \mathbf{U} - structure velocity
- $e_{ij} = \frac{1}{2} \left(\frac{\partial X_j}{\partial x_i} + \frac{\partial X_i}{\partial x_j} \right)$ - linear strain tensor;
- i, j denote vector components
- dS_f - integration element over fluid free surface
- ds_s - integration element over structure-fluid interface
- dx_F - integration element over fluid domain
- dx_S - integration element over structure domain

After numerous manipulations (described in detail in Salwa et al. (2017)) and evaluation of individual variations, the time-discrete equations, with symplectic Euler scheme, to be implemented in Firedrake, are:

$$\begin{aligned}
 \int v \phi^{n+1} dS_f &= \int v(\phi^n - \Delta t \eta^n) dS_f \\
 \int \rho_0 \mathbf{v} \cdot \mathbf{U}^{n+1} dx_S + \int \mathbf{n} \cdot \mathbf{v} \phi^{n+1} ds_s &= \rho_0 \int \mathbf{v} \cdot \mathbf{U}^n dx_S \\
 &\quad - \Delta t \int \left(\lambda \nabla \cdot \mathbf{v} \nabla \cdot \mathbf{X}^n + \mu \frac{\partial X_j^n}{\partial x_i} \left(\frac{\partial v_i}{\partial x_j} + \frac{\partial v_j}{\partial x_i} \right) \right) dx_S + \int \mathbf{n} \cdot \mathbf{v} \phi^n ds_s \\
 \int \nabla v \cdot \nabla \phi^{n+1} dx_F - \int v \mathbf{n} \cdot \mathbf{U}^{n+1} ds_s &= 0 \\
 \int v \eta^{n+1} dS_f &= \int v \eta^n dS_f + \Delta t \int \nabla v \cdot \nabla \phi^{n+1} dx_F - \Delta t \int v \mathbf{n} \cdot \mathbf{U}^{n+1} ds_s \\
 \int \mathbf{v} \cdot \mathbf{X}^{n+1} dx_S &= \int \mathbf{v} \cdot (\mathbf{X}^n + \Delta t \mathbf{U}^{n+1}) dx_S.
 \end{aligned}$$

The underlined terms are the coupling terms. Note that the first equation for ϕ at the free surface is solved on the free surface only, the last equation for \mathbf{X} in the structure domain, while the others are solved in both domains. Moreover, the second and third equations for ϕ and \mathbf{U} need to be solved simultaneously. The geometry of the system with initial condition is shown in Fig. 6.1.

Now the code used to solve the system of equations above is presented. One starts with appropriate imports:

```

from firedrake import *
import math
import numpy as np
    
```

Then, parameters of the simulation are set:

```

# parameters in SI units
t_end = 5. # time of simulation [s]
dt = 0.005 # time step [s]
    
```

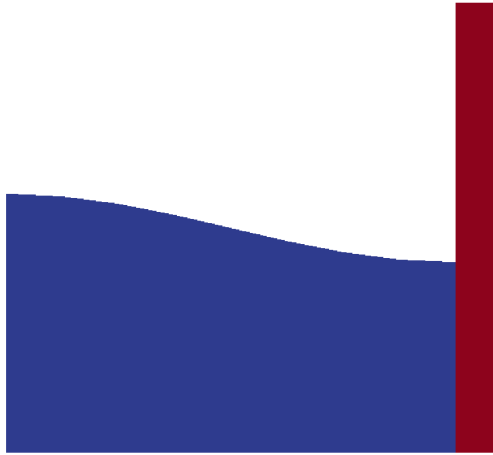


Figure 6.1: Geometry and initial condition in the system. Fluid with deflected free surface (blue) and the structure (red).

```

g = 9.8 # gravitational acceleration
# water
Lx = 20. # length of the tank [m] in x-direction;
          # needed for computing initial condition
Lz = 10. # height of the tank [m];
          # needed for computing initial condition
rho = 1000. # fluid density in kg/m^2 in 2D [water]
# solid parameters
# - a sufficiently soft material is used to be able
#   to see noticeable structural displacement
rho_B = 7700. # structure density in kg/m^2 in 2D
lam = 1e7 # N/m in 2D - first Lamé constant
mu = 1e7 # N/m in 2D - second Lamé constant
# mesh
mesh = Mesh("L_domain.msh")
#numbers below must match those defined in the mesh file

```

```

fluid_id = 1 # fluid subdomain
structure_id = 2 # structure subdomain
bottom_id = 1 # structure bottom
top_id = 6 # fluid surface
interface_id = 9 # fluid-structure interface
# control parameters
# to avoid saving data every time step:
output_data_every_x_time_steps = 20
coupling = True # turn on coupling terms

```

The equations are in nondimensional units, hence they are transformed:

```

L = Lz
T = L/math.sqrt(g*L)
t_end /= T
dt /= T
Lx /= L
Lz /= L
rho_B /= rho
lam /= g*rho*L
mu /= g*rho*L
rho = 1. # or equivalently rho /= rho

```

Let us define function spaces, including the mixed one:

```

V_W = FunctionSpace(mesh, "CG", 1)
V_B = VectorFunctionSpace(mesh, "CG", 1)
mixed_V = V_W * V_B

```

Then, functions are defined. First, in the fluid domain:

```

phi = Function(V_W, name="phi")
phi_f = Function(V_W, name="phi_f") #at the free surface
eta = Function(V_W, name="eta")
trial_W = TrialFunction(V_W)
v_W = TestFunction(V_W)

```

Second, in the beam domain:

```

X = Function(V_B, name="X")
U = Function(V_B, name="U")
trial_B = TrialFunction(V_B)
v_B = TestFunction(V_B)

```

And last, mixed functions in the mixed domain:

```

trial_f , trial_s = TrialFunctions(mixed_V)
v_f , v_s = TestFunctions(mixed_V)
tmp_f = Function(V_W)
tmp_s = Function(V_B)
result_mixed = Function(mixed_V)

```

Auxiliary indicator functions are needed, that are 0 in one subdomain and 1 in the other. They are needed both in "CG" and "DG" space. The fact is used that the fluid and structure subdomains are defined in the mesh file with an appropriate ID number that Firedrake is able to recognise. That can be used in constructing indicator functions:

```

V_DG0_W = FunctionSpace(mesh, "DG", 0)
V_DG0_B = FunctionSpace(mesh, "DG", 0)

# Heaviside step function in fluid
I_W = Function( V_DG0_W )
par_loop(

```

```

    'for_(int i=0; i<f.dofs; i++) f[i][0] = 1.0;',
        dx(fluid_id), {'f': (I_W, WRITE)} )
I_cg_W = Function(V_W)
par_loop('for_(int i=0; i<A.dofs; i++)'
        +'A[i][0] = fmax(A[i][0], B[0][0]);',
        dx, {'A': (I_cg_W, RW), 'B': (I_W, READ)} )

# Heaviside step function in solid
I_B = Function( V_DG0_B )
par_loop('for_(int i=0; i<f.dofs; i++) f[i][0] = 1.0;',
        dx(structure_id), {'f': (I_B, WRITE)} )
I_cg_B = Function(V_B)
par_loop('for_(int i=0; i<A.dofs; i++)'
        +'for_(int j=0; j<2; j++)'
        +'A[i][j] = fmax(A[i][j], B[0][0]);',
        dx, {'A': (I_cg_B, RW), 'B': (I_B, READ)})

```

Indicator functions are used to construct normal unit vector outward to the fluid domain at the fluid-structure interface:

```

n_vec = FacetNormal(mesh)
n_int = I_B("++") * n_vec("++") + I_B("--") * n_vec("--")

```

Now special boundary conditions can be constructed that limit the solvers only to the appropriate subdomains of our interest:

```

class MyBC(DirichletBC):
    def __init__(self, V, value, markers):
        # Call superclass init
        # We provide a dummy subdomain id.
        super(MyBC, self).__init__(V, value, 0)

```

```

        # Override the "nodes" property which says where
        # the boundary condition is to be applied.
        self.nodes=np.unique(np.where(
            markers.dat.data_ro_with_halos==0)[0])

def surface_BC():
    # This will set nodes on the top boundary to 1.
    bc = DirichletBC( V_W, 1, top_id )
    # We will use this function to determine new BC nodes
    # (all those that aren't on the boundary)
    f = Function( V_W, dtype=np.int32 )
    # f is now 0 everywhere, except on the boundary
    bc.apply(f)
    # Now MyBC can be used to create
    # a "boundary condition" to zero out all the nodes
    # that are *not* on the top boundary:
    return MyBC( V_W, 0, f )

# same as above, but in the mixed space
def surface_BC_mixed():
    bc_mixed = DirichletBC( mixed_V.sub(0), 1, top_id )
    f_mixed = Function( mixed_V.sub(0), dtype=np.int32 )
    bc_mixed.apply(f_mixed)
    return MyBC( mixed_V.sub(0), 0, f_mixed )

BC_exclude_beyond_surface = surface_BC()
BC_exclude_beyond_surface_mixed = surface_BC_mixed()
BC_exclude_beyond_solid = MyBC( V_B, 0, I_cg_B )

```

Finally, one is ready to define the solvers of our equations. First, equation for ϕ at the free surface:

```
a_phi_f = trial_W * v_W * ds(top_id)
L_phi_f = ( phi_f - dt * eta ) * v_W * ds(top_id)
LVP_phi_f = LinearVariationalProblem( a_phi_f , L_phi_f ,
                                     phi_f , bcs=BC_exclude_beyond_surface )
LVS_phi_f = LinearVariationalSolver( LVP_phi_f )
```

Second, equation for the beam displacement X , where it is also fixed to the bottom by applying zero Dirichlet boundary condition:

```
a_X = dot( trial_B , v_B ) * dx(structure_id)
L_X = dot( (X + dt * U) , v_B ) * dx(structure_id)
# no-motion beam bottom boundary condition
BC_bottom = DirichletBC( V_B , Expression([0.,0.]) , bottom_id )
LVP_X = LinearVariationalProblem(a_X , L_X , X ,
                                 bcs = [BC_bottom , BC_exclude_beyond_solid ])
LVS_X = LinearVariationalSolver( LVP_X )
```

Finally, solvers for ϕ , U and η in the mixed domain are defined. In particular, value of ϕ at the free surface is used as a boundary condition. Note that `avg(...)` is necessary for terms in expressions containing `n_int`, which is built in "DG" space:

```
# phi-U equations:
#no-motion beam bottom boundary condition in mixed space
BC_bottom_mixed = DirichletBC( mixed_V.sub(1),
                               Expression([0.,0.]) , bottom_id )
# boundary condition to set phi_f at the free surface
BC_phi_f = DirichletBC( mixed_V.sub(0), phi_f , top_id )
delX = nabla_grad(X)
delv_B = nabla_grad(v_s)
```

```

T_x_dv = lam * div(X) * div(v_s)
          + mu * (inner(delX, delv_B + transpose(delv_B)))
a_U = rho_B * dot( trial_s , v_s ) * dx(structure_id)
L_U = (rho_B * dot(U, v_s) - dt*T_x_dv) * dx(structure_id)
a_phi = dot( grad(trial_f), grad(v_f) ) * dx(fluid_id)
if coupling:
    a_U += dot( avg(v_s), n_int ) * avg(trial_f) * dS
    # avg(...) necessary here and below
    L_U += dot( avg(v_s), n_int ) * avg(phi) * dS
    a_phi += - dot( n_int , avg(trial_s) ) * avg(v_f) * dS
LVP_U_phi = LinearVariationalProblem( a_U + a_phi , L_U,
                                     result_mixed , bcs=[BC_phi_f , BC_bottom_mixed] )
LVS_U_phi = LinearVariationalSolver( LVP_U_phi )

# eta
a_eta = trial_f * v_f * ds(top_id)
L_eta = eta * v_f * ds(top_id)
        + dt * dot( grad(v_f), grad(phi) ) * dx(fluid_id)
if coupling:
    L_eta += - dt * dot( n_int , avg(U) ) * avg(v_f) * dS
LVP_eta = LinearVariationalProblem(
    a_eta , L_eta , result_mixed ,
    bcs=BC_exclude_beyond_surface_mixed )
LVS_eta = LinearVariationalSolver( LVP_eta )

```

Let us set the initial condition. No motion at the beginning in both fluid and structure is chosen, zero displacement in the structure and deflected free surface in the fluid. The shape of the deflection is computed from the analytical solution:

```

# initial condition in fluid based on analytical solution

```

```

# compute analytical initial phi and eta
n_mode = 1
a = 0. * T / L**2 # in nondim units
b = 5. * T / L**2 # in nondim units
lambda_x = np.pi*n_mode/Lx
omega = np.sqrt( lambda_x*np.tanh(lambda_x*Lz) )
x = mesh.coordinates
phi_exact_expr = a*cos(lambda_x*x[0])*cosh(lambda_x*x[1])
eta_exact_expr = -omega*b \
                *cos(lambda_x*x[0])*cosh(lambda_x*Lz)

bc_top = DirichletBC(V_W, 0, top_id)
eta.assign(0.)
phi.assign(0.)
eta_exact = Function(V_W)
eta_exact.interpolate( eta_exact_expr )
eta.assign( eta_exact , bc_top.node_set )
phi.interpolate( phi_exact_expr )
phi_f.assign( phi , bc_top.node_set )

```

A file to store data for visualization:

```
outfile_phi = File("results_pvd/phi.pvd")
```

To save data for visualization, the position of the nodes in the mesh is changed, so that they represent the computed dynamic position of the free surface and the structure:

```

def output_data():
    output_data.counter += 1
    if output_data.counter \
        %output_data_every_x_time_steps !=0:

```

```

return

mesh_static = mesh.coordinates.vector().get_local()
mesh.coordinates.vector().set_local(
    mesh_static + X.vector().get_local() )
mesh.coordinates.dat.data[:,1] += eta.dat.data_ro
outfile_phi.write( phi )
mesh.coordinates.vector().set_local( mesh_static )
# -1 below to exclude counting print of initial state
output_data.counter = -1

```

In the end, one proceeds with the actual computation loop:

```

t = 0.
output_data()
while t <= t_end + dt:
    t += dt
    print( 'time = ', t * T)
    # symplectic Euler scheme
    LVS_phi_f.solve()
    LVS_U_phi.solve()
    tmp_f, tmp_s = result_mixed.split()
    phi.assign(tmp_f)
    U.assign(tmp_s)
    LVS_eta.solve()
    tmp_f, _ = result_mixed.split()
    eta.assign(tmp_f)
    LVS_X.solve()
    output_data()

```

The result of the computation, visualised with paraview, is shown here:

<https://youtu.be/C4CpFmxKZGw>.

The mesh is deflected for visualization only. As the model is linear, the actual mesh used for computation is fixed. Colours indicate values of the flow potential ϕ .

A python script version of this demo can be found here: https://firedrakeproject.org/demos/linear_fluid_structure_interaction.py.

The mesh file is here: https://firedrakeproject.org/demos/L_domain.msh. It can be generated with gmesh from this file: https://firedrakeproject.org/demos/L_domain.geo, with a command: `gmsh -2 L_domain.geo`.

An extended 3D version of this code is published at this address: <https://zenodo.org/record/1162196>.

Chapter 7

Conclusions

7.1 Summary

7.1.1 Achievements and concomitant extensions

The achievement of this thesis has been the development of a mathematical model (using a variational formulation) and its successful implementation (using a Galerkin finite element method) as a simulation tool for describing a physical system consisting of water waves interacting with an offshore wind-turbine mast.

For the mathematical model, the starting point is an action functional describing a dual system comprising a potential-flow fluid, a solid structure modelled with nonlinear elasticity, and the coupling between them. A linearized model has been developed of the fluid-structure (*i.e.* wave-mast) coupling, based on the variational principle for the fully coupled nonlinear model. Numerical results obtained for the linear case indicate that the present variational approach yields a stable numerical discretization of a fully coupled model of water waves and an elastic beam. The energy exchange between the subsystems has been demonstrated to be in balance, yielding a total energy that shows only small and bounded oscillations with second-order convergence in time. Similarly, (second-order) convergence is observed for spatial mesh refinement. While

the finite-element discretization of the nonlinear hyperelastic beam structure has been formulated and implemented and the finite-element discretization and implementation of the nonlinear water-wave equations is available (Gidel, 2018), both via geometric variational techniques, our linear finite-element formulations of the coupled model has not yet been extended to the nonlinear régime.

Within the context of applying the simulation tool to realistic wave-mast interactions, the main drawback of the incompressible potential-flow model is that it inevitably does not admit wave-breaking. Moreover, coupling of nonlinear waves with the beam proves challenging due to the finite motion of the domains being described at the nonlinear level in two different formalisms, namely Eulerian for the fluid and Lagrangian for the beam. As a result, computational meshes of the two subsystems no longer match at the fluid-structure interface, whereas nonlinear coupling transpires to be prone to numerical instability. Rather than pursuing this direction, another model was proposed that is loosely based on a van-der-Waals gas. The starting point is again an action functional, but with an extra term representing internal energy. The flow can be assumed to have no rotation, so it is again described with a potential, but now compressibility is incorporated. The functional thus yields a rotationless momentum equation. The free surface is embedded within the compressible fluid for an appropriate van-der-Waals-inspired equation of state, which admits a pseudo-phase transition between the water and air phases separated by a sharp or steep transition in density. Due to the compressibility, in addition to gravity waves the ideal-gas model leads to acoustic waves. Though there is an inherent risk that the results will be dominated by acoustic waves, their higher frequencies admit the possibility of filtering and dampening using suitable implicit time integrators. Both hydrostatic and linearized models have been examined as verification steps. With a proper choice of equation of state that models also a finite-width interface, the dispersion relation confirms that there are multiple wave modes present, including gravity water waves. The model also matches incompressible linear potential flow, which is an important verification step. However, at the nonlinear level, the acoustic noise proves significant.

When dealing with the control and dampening of acoustic noise in the ideal-gas model, the model can — similarly to the incompressible potential-flow case of the first approach — be readily coupled to a hyperelastic beam, but now with a nonlinear fluid and (possibly) breaking waves. Ongoing efforts are being made both to analyse and to implement this development and, once implementation of the model is validated, it can be directly deployed by the marine industry as a helpful simulation tool in the quantification of offshore-wind turbine design.

7.1.2 Outreach

As the work presented in this thesis was part of an European Industry Doctorate, public outreach was an inherent part of it. A personal website <http://www1.maths.leeds.ac.uk/~mmtjs/>, a Facebook page <https://www.facebook.com/surfsupeuid/> and online blog <https://blogsurfsup.wordpress.com/> have been regularly updated with work progress. Moreover, a few public talks for a general non-scientific audience have been given. These included:

- 5th March 2018 - Talk for seniors - University of the Third Age in Starachowice, Poland - *Modelling of sea waves; Freak waves*
- 17th November 2015 and 6th March 2018 - High School talk - II High School in Starachowice, Poland - *Modelling of sea waves; Freak waves*
- 2nd November 2015 - Talk at Cafe Scientifique - New Headingley Club, Headingley, Leeds (UK) - *Legendary freak waves and their evolution in the scientific world*
- 12th September and 10th October, 2015 - School of Mathematics Open days - University of Leeds (UK) - Demonstrations with small scale wave maker, comparison with simulations and explanation of the modeling process.

7.1.3 Experiment

During the development of the mathematical model and simulation, a small-scale table-top experiment was conducted. The wave tank was constructed by Booker et al. (2015), and it consisted of an elongated water tank with a wavemaker at one end and a beach to dampen the waves at the other. For this project, a beam model was included; it comprised an insulating foam pipe fastened to the bottom of the tank through a platform made of modelling foam, see Fig. 7.1. The wave maker was driven with a motor connected to Arduino platform. The end-user could control the wave making with a back-end interface written in C/C++. The experiment was intended as an introduction to a large-scale one to



Figure 7.1: The wave tank set-up with a wave-maker (left), beach (right) and a beam.

be conducted at Maritime Research Institute Netherlands (MARIN), see <http://www.marin.nl>, where part of the work on the project was done. The recording of the table-top experiment was also useful in outreach presentations for non-scientific audiences.

Appendices

A Derivation of temporal discretization

In this appendix, the details of the derivation of the temporal scheme for linear coupled potential flow-elastic beam system are presented. Given eq. (4.43), in terms of original variables, the interim equations of motion arising from the VP for (4.36) become

$$\begin{aligned}
 \phi_\alpha^{n+1/2} &= \phi_\alpha^n - \frac{1}{2}\Delta t \eta_\alpha^n, \\
 N_{k'l'} (P_{l'}^a)^{n+1/2} &= N_{k'l'} (P_{l'}^a)^n - \frac{1}{2}\Delta t E_{k'l'}^{ab} (X_{l'}^b)^n, \\
 M_{\alpha\beta} \eta_\beta^{n+1} &= M_{\alpha\beta} \eta_\beta^n + \Delta t \left(B_{\alpha\beta} \phi_\beta^{n+1/2} - U_{k'\alpha}^a (P_{k'}^a)^{n+1/2} \right), \\
 N_{k'l'} (X_{l'}^a)^{n+1} &= N_{k'l'} (X_{l'}^a)^n + \Delta t \left(-U_{k'\alpha}^a \phi_\alpha^{n+1/2} + F_{k'l'}^{ab} (P_{l'}^b)^{n+1/2} \right), \\
 \phi_\alpha^{n+1} &= \phi_\alpha^{n+1/2} - \frac{1}{2}\Delta t \eta_\alpha^{n+1}, \\
 N_{k'l'} (P_{l'}^a)^{n+1} &= N_{k'l'} (P_{l'}^a)^{n+1/2} - \frac{1}{2}\Delta t E_{k'l'}^{ab} (X_{l'}^b)^{n+1/2}.
 \end{aligned} \tag{A.1}$$

The matrices B , F and U appearing in (A.1) contain the inverse of matrix C which was introduced both to remove the interior ϕ degrees of freedom and to reduce the system to the Hamiltonian form. However, once the temporal scheme is obtained, one would like to avoid the costly computation of the inverse of C . Therefore, guided by (4.35), see also Gagarina et al. (2014), $\phi_{i'}$ is re-introduced in the interior as

$$C_{i'j'} \phi_{i'}^{n+1/2} = -A_{\alpha j'} \phi_\alpha^{n+1/2} + (P_{\tilde{m}'}^1)^{n+1/2} W_{\tilde{m}'n} \delta_{nj'} - \delta_{m\alpha} \phi_\alpha^{n+1/2} \tilde{m}_{mn} \delta_{nj'}. \tag{A.2}$$

After some manipulations, one finds that the final discrete spatio-temporal, fluid-structure interaction equations (*cf.* (4.33)) are

$$\phi_\alpha^{n+1/2} = \phi_\alpha^n - \frac{1}{2}\Delta t \eta_\alpha^n \quad (\text{A.3a})$$

$$N_{k'l'}(P_{l'}^a)^{n+1/2} = N_{k'l'}(P_{l'}^a)^n - \frac{1}{2}\Delta t E_{k'l'}^{ab}(X_{l'}^b)^n \quad (\text{A.3b})$$

$$\underbrace{(A_{i'j'} + \delta_{i'm}\widetilde{M}_{mn}\delta_{j'n})\phi_{i'}^{n+1/2}} = -A_{\alpha j'}\phi_\alpha^{n+1/2} + \underbrace{((P_{\widetilde{m}'}^1)^{n+1/2}W_{\widetilde{m}'n} - \widetilde{M}_{mn}\phi_\alpha^{n+1/2}\delta_{\alpha m})\delta_{n j'}} \quad (\text{A.3c})$$

$$\begin{aligned} M_{\alpha\beta}\eta_\beta^{n+1} &= M_{\alpha\beta}\eta_\beta^n + \Delta t A_{\alpha i}\phi_i^{n+1/2} \\ &\quad + \underbrace{\Delta t(\phi_m^{n+1/2}\widetilde{M}_{mn} - (P_{\widetilde{m}'}^1)^{n+1/2})W_{\widetilde{m}'n}\delta_{n\alpha}} \end{aligned} \quad (\text{A.3d})$$

$$N_{k'l'}(X_{l'}^a)^{n+1} = N_{k'l'}(X_{l'}^a)^n + \Delta t N_{k'l'}(P_{l'}^a)^{n+1/2} - \underbrace{\Delta t \delta_{a1}\delta_{k'\widetilde{m}'}W_{\widetilde{m}'n}\phi_n^{n+1/2}} \quad (\text{A.3e})$$

$$\phi_\alpha^{n+1} = \phi_\alpha^{n+1/2} - \frac{1}{2}\Delta t \eta_\alpha^{n+1} \quad (\text{A.3f})$$

$$N_{k'l'}(P_{l'}^a)^{n+1} = N_{k'l'}(P_{l'}^a)^{n+1/2} - \frac{1}{2}\Delta t E_{k'l'}^{ab}(X_{l'}^b)^{n+1}, \quad (\text{A.3g})$$

in which, as in (4.33), the newly derived coupling terms are underlined.

Implementation of the above formulation leads to a system that conserves energy to second order in the timestep, in keeping with Störmer-Verlet theory. However, using P is inconvenient, as it does not directly represent a physical variable. Moreover, the time evolution of the separate components of (4.31) reveals an equal and opposite monotonic increase in three terms that involve coupling, which annihilate each other when composed to form the physical energy. This behaviour is possibly related to the fact that not all terms in (4.31) are positive definite. As a result of this observation one is motivated to reformulate (A.3) in terms of the original physical variable (structural velocity)

$$U_{k'}^a = P_{k'}^a - \delta_{a1}N_{k'\widetilde{m}'}^{-1}W_{\widetilde{m}'n}\phi_n, \quad (\text{A.4})$$

which is itself motivated by (4.24) and (4.29). When this approach is used, the Hamiltonian (4.31) once more becomes the positive definite (4.23). Equation (A.3) is,

as a result, amended to the form (4.44).

Bibliography

- S. S. Antman. *Nonlinear Problems of Elasticity*. Springer New York, second edition, 1995.
- M. Benitz, M. Lackner, and D. Schmidt. Hydrodynamics of offshore structures with specific focus on wind energy applications. *Renewable and Sustainable Energy Reviews*, 44:692 – 716, 2015. ISSN 1364-0321. doi: 10.1016/j.rser.2015.01.021. URL <http://www.sciencedirect.com/science/article/pii/S1364032115000313>.
- O. Bokhove and A. Kalogirou. Variational water wave modelling: from continuum to experiment. In: *Bridges, T., Groves, M. and Nicholls, D. (eds.) Lectures on the Theory of Water Waves. LMS Lecture Note Series.*, pages 226–260, 2016.
- O. Bokhove, F. Gidel, and T. Salwa. SURFS-UP: Freak waves and breaking wave impact on offshore structures, European Industry Doctorate mid-term report. Technical report, 2016.
- W. Booker, T. Goodfellow, and J. van Alwon. Experimental and numerical modelling of coastal processes. 2015. Report of team project, University of Leeds, Doctoral Training Centre in Fluid Dynamics.
- T. Bunnik, J. Helder, and E.-J. de Ridder. Simulation of the flexible response of a fixed offshore wind turbine subject to breaking waves. *7th International Conference on Hydroelasticity in Marine Technology, Split, Croatia*, pages 65–81, 9 2015.

BIBLIOGRAPHY

- P. Causin, J. Gerbeau, and F. Nobile. Added-mass effect in the design of partitioned algorithms for fluidstructure problems. *Computer Methods in Applied Mechanics and Engineering*, 194(42):4506 – 4527, 2005. ISSN 0045-7825. doi: <https://doi.org/10.1016/j.cma.2004.12.005>. URL <http://www.sciencedirect.com/science/article/pii/S0045782504005328>.
- M. Dumbser. A simple two-phase method for the simulation of complex free surface flows. *Computer Methods in Applied Mechanics and Engineering*, 200:1204–1219, 2011.
- C. Förster, W. A. Wall, and E. Ramm. Artificial added mass instabilities in sequential staggered coupling of nonlinear structures and incompressible viscous flows. *Computer Methods in Applied Mechanics and Engineering*, 196(7):1278 – 1293, 2007. ISSN 0045-7825. doi: <https://doi.org/10.1016/j.cma.2006.09.002>. URL <http://www.sciencedirect.com/science/article/pii/S0045782506002544>.
- E. Gagarina, V. R. Ambati, J. J. W. van der Vegt, and O. Bokhove. Variational space-time (dis)continuous Galerkin method for nonlinear free surface water waves. *Journal of Computational Physics*, 275:459–483, 2014. doi: 10.1016/j.jcp.2014.06.035.
- E. Gagarina, V. Ambati, S. Nuriyanyan, J. van der Vegt, and O. Bokhove. On variational and symplectic time integrators for Hamiltonian systems. *Journal of Computational Physics*, 306:370–389, 2016. doi: 10.1016/j.jcp.2015.11.049.
- F. Gidel. *PhD Thesis: Variational water-wave models and pyramidal freak waves*. 2018. URL <https://theses.whiterose.ac.uk/21730/>.
- F. Golay, M. Ersoy, L. Yushchenko, and D. Sous. Block-based adaptive mesh refinement scheme using numerical density of entropy production for three-dimensional two-fluid flows. *International Journal of Computational Fluid Dynamics*, 29(1):67–81, 2015. doi: 10.1080/10618562.2015.1012161. URL <https://doi.org/10.1080/10618562.2015.1012161>.

BIBLIOGRAPHY

- B. Hübner, E. Walhorn, and D. Dinkler. A monolithic approach to fluid-structure interaction using space-time finite elements. *Computer Methods in Applied Mechanics and Engineering*, 193(2326):2087 – 2104, 2004. ISSN 0045-7825. doi: 10.1016/j.cma.2004.01.024. URL <http://www.sciencedirect.com/science/article/pii/S0045782504000696>.
- S. Hunter. *Mechanics of Continuous Media*. Ellis Horwood, 1976.
- B. Leimkuhler and S. Reich. *Simulating Hamiltonian Dynamics*. Cambridge University Press, 2004.
- J. C. Luke. A variational principle for a fluid with a free surface. *Journal of Fluid Mechanics*, 27:395–397, 1967.
- J. E. Marsden and M. West. Discrete mechanics and variational integrators. *Acta Numerica*, 10:357514, 2001. doi: 10.1017/S096249290100006X.
- J. W. Miles. On Hamilton’s principle for surface waves. *Journal of Fluid Mechanics*, 83: 153–158, 1977.
- F. Rathgeber, D. A. Ham, L. Mitchell, M. Lange, F. Luporini, A. T. T. McRae, G. Bercea, G. R. Markall, and P. H. J. Kelly. Firedrake: automating the finite element method by composing abstractions. *ACM Transactions on Mathematical Software*, 43(3):24:124:27, 2016. doi: 10.1145/2998441. URL <http://arxiv.org/abs/1501.01809>.
- H. Sagar, J. Ley, and B. el Moctar. Hydroelasticity effects of wave induced loads on offshore monopile structure. *7th International Conference on Hydroelasticity in Marine Technology, Split, Croatia*, pages 82–101, 9 2015.
- T. Salwa, O. Bokhove, and M. Kelmanson. Variational coupling of wave slamming against elastic masts. *31st International Workshop on Water Waves and Floating Bodies, IWWWFB, Michigan, USA*, pages 149–152, 2016a. URL http://www.iwwwfb.org/Abstracts/iwwwfb31/iwwwfb31_39.pdf.

BIBLIOGRAPHY

- T. Salwa, O. Bokhove, and M. Kelmanson. Variational modelling of wave-structure interactions for offshore wind turbines. *Extended paper for Int. Conf. on Ocean, Offshore and Arctic Eng., OMAE2016, Busan, South-Korea*, page 10, 6 2016b. URL <http://proceedings.asmedigitalcollection.asme.org/proceeding.aspx?articleID=2570974>.
- T. Salwa, O. Bokhove, and M. A. Kelmanson. Variational modelling of wave-structure interactions with an offshore wind-turbine mast. *Journal of Engineering Mathematics*, 107(1):61–85, Dec 2017. ISSN 1573-2703. doi: 10.1007/s10665-017-9936-4. URL <https://doi.org/10.1007/s10665-017-9936-4>.
- R. Sullivan, L. Kirchler, S. Roch, K. Beckman, and P. Richmond. Wind turbine visibility and visual impact threshold distances in western landscapes. *Proceedings, National Association of Environmental Professionals, 37th Annual Conference, May 2124, 2012, Portland, 2012*.
- R. G. Sullivan, L. B. Kirchler, J. Cothren, and S. L. Winters. Offshore wind turbine visibility and visual impact threshold distances. *Environmental Practice*, 15(1):3349, 2013. doi: 10.1017/S1466046612000464.
- R. Temam and A. Miranville. *Mathematical modeling in continuum mechanics*. Cambridge University Press, 2005.
- E. H. van Brummelen, M. Shokrpour-Roudbari, and G. J. van Zwieten. *Elasto-Capillarity Simulations Based on the Navier-Stokes-Cahn-Hilliard Equations*, pages 451–462. Springer International Publishing, Cham, 2016. ISBN 978-3-319-40827-9. doi: 10.1007/978-3-319-40827-9_35. URL http://dx.doi.org/10.1007/978-3-319-40827-9_35.
- E. van Daalen, E. van Groesen, and P. Zandbergen. A Hamiltonian formulation for nonlinear wave-body interactions. *Eighth International Workshop on Water Waves and Floating Bodies, IWWWFB*, pages 159–163, 1993. URL <http://doc.utwente.nl/30984/>.

BIBLIOGRAPHY

G. B. Whitham. *Linear and Nonlinear Waves*. New York ; Chichester : Wiley, 1999.